Predictions of Control Inputs, Periodic Responses and Damping Levels of an Isolated Experimental Rotor in Trimmed Flight

Final Technical Report Under NASA-Ames Research Grant No. NAG 2-797

G. H. Gaonkar
S. Subramanian

AUG 2 7 1996

CASI

FLORIDA ATLANTIC UNIVERSITY
Department of Mechanical Engineering
College of Engineering
Boca Raton, FL 33431

July 31, 1996

Contents

Abstract

Since the early 1990s the Aeroflightdynamics Directorate at the Ames Research Center has been conducting tests on isolated hingeless rotors in hover and forward flight. The primary objective is to generate a database on aeroelastic stability in trimmed flight for torsionally soft rotors at realistic tip speeds. The rotor test model has four soft inplane blades of NACA 0012 airfoil section with low torsional stiffness. The collective pitch and shaft tilt are set prior to each test run, and then the rotor is trimmed in the following sense: the longitudinal and lateral cyclic pitch controls are adjusted through a swashplate to minimize the 1/rev flapping moment at the 12% radial station. In hover, the database comprises lag regressive-mode damping with collective pitch variations: $-3^0 \leq \theta_0 \leq 8^0$. In forward flight the database comprises cyclic pitch controls, root flap moment and lag regressive-mode damping with advance ratio, shaft angle and collective pitch variations: $0 \leq \mu \leq 0.36$, $0^0 \leq \alpha_s \leq 6^0$, and $0^0 \leq \theta_0 \leq 5.9^0$. This report presents the predictions and their correlation with the database. A modal analysis is used, in which nonrotating modes in flap bending, lag bending and torsion are computed from the measured blade mass and stiffness distributions. The airfoil aerodynamics is represented by the ONERA dynamic stall models of lift, drag and pitching moment, and the wake dynamics is represented by a state-space wake model. The trim analysis of finding the cyclic controls and the corresponding periodic responses is based on periodic shooting with damped Newton iteration; the Floquet transition matrix (FTM) comes out as a byproduct. The stability analysis of finding the frequencies and damping levels is based on the eigenvalue-eigenvector analysis of the FTM. All the structural and aerodynamic states are included from modeling to trim analysis to stability analysis. A major finding is that dynamic wake dramatically improves the correlation for the lateral cyclic pitch control. Overall, the correlation is fairly good.

Nomenclature

Unless otherwise stated, the symbols below are dimensionless:

a	linear lift curve slope
a_d, a_m	damping factors in dynamic stall drag and pitching moment models

b	airfoil semi-chord, $(1/R)$
c, c	airfoil chord, $(m, 1/R)$
C_d, C_{d_0}	airfoil drag coefficient and constant profile-drag coefficient
C_{d_s}	quasisteady drag coefficient
C_z, C_m	airfoil lift and pitching moment coefficients
C_{m_0}	airfoil pitching moment coefficient at zero angle of attack
C_{m_s}	quasisteady pitching moment coefficient
C_T	thrust coefficient
C_T/σ_s	thrust level
C_{z_l}	extrapolated linear-lift coefficient
C_{z_s}	quasisteady lift coefficient
d	dynamic-stall-lift damping parameter
e	phase shift parameter in dynamic stall lift model
$e_f, \overline{e}_f$	radial station for flapping moment estimation, $(1/R, m)$
$e_h, \overline{e}_h$	hinge offset, $(1/R, m)$
E_d, E_m	phase shift parameters in dynamic stall drag and pitching moment models
$FM_{ij}^1, \ldots, FM_i^{12}$	Galerkin-type integrals, Eq. (20)
$\mathbf{I}, \mathbf{J}, \mathbf{K}$	unit vectors associated with inertial frame
$\mathbf{i}, \mathbf{j}, \mathbf{k}$	unit vectors associated with undeformed blade coordinate system
k_{m_1}, k_{m_2}	mass radii of gyration of blade cross section about its principle axes
$\ell, \overline{\ell}$	blade span, $1 - e_h$, $(1/R, m)$
L_u, L_w	sectional aerodynamic forces
$\mathcal{L}_u, \mathcal{L}_w$	total horizontal and vertical forces, (N)
m	mass per unit length, (kg/m)
m_r	reference mass per unit length, (kg/m)
M_ϕ	aerodynamic pitching moment
$\mathcal{M}_v$	total pitching moment, (Nm)
$\overline{\mathcal{M}}$	total flap moment at e_f, $(1/\rho b\Omega^2 R^4)$
$\overline{\mathcal{M}}_{nc}$	n-th harmonic cosine component of $\overline{\mathcal{M}}$

$\overline{\mathcal{M}}_{ns}$	n-th harmonic sine component of $\overline{\mathcal{M}}$
$\overline{\mathcal{M}}_0$	steady component of $\overline{\mathcal{M}}$
r_c	root cutout, $(1/R)$
r_d, r_m	frequency parameters in dynamic stall drag and pitching moment models
$\overline{r}_i$	radial station of the i-th blade, $(1/R)$
R	rotor radius, (m)
t	time, $(1/\Omega)$
v	inplane (lag) bending deflection
$\overline{v}$	dimensional inplane (lag) bending deflection
$V_i(\psi)$	generalized coordinate of i-th mode for lag degree of freedom
w	dynamic stall lift frequency parameter; also out of plane (flap) bending deflection, $(1/R)$
$\overline{w}$	dimensional out of plane (flap) bending deflection
$W_i(\psi)$	generalized coordinate of i-th mode for flap degree of freedom
X, Y, Z	inertial coordinate system
x, y, z	undeformed coordinate system
$x, \overline{x}$	radial distance measured from the rotor center, $(1/R, m)$
α	blade airfoil angle of attack
α_s	shaft angle, (deg, rad)
α_{ss}	quasisteady stall angle, (deg)
β_{pc}	blade precone, (deg)
γ	Lock number (blade inertia parameter)
δ	pitch-rate coefficient
θ	blade pitch angle
θ_0	collective pitch angle, (deg, rad)
θ_c, θ_s	lateral and longitudinal cyclic pitch angles, (deg, rad)
λ	time-delay parameter
Λ_2	flap bending stiffness, $(1/m_r \Omega^2 R^4)$
μ	advance ratio

σ_s	rotor solidity
ψ_i	azimuthal location of the i-th blade
Ψ_i	i-th flap mode
ρ_s	blade mass density (kg/m^3)
ρ_∞	air density (kg/m^3)
Ω	rotor angular speed, (rad/sec)
$(\ )^A$	aerodynamic component of $(\ )$
$(\ )^I$	inertial component of $(\ )$
$(\dot{\ })$	time derivative of $(\ )$
$(\ )'$	spatial derivative of $(\ )$
$\approx$	approximately equal to
NEL	number of aerodynamic elements
NOM	number of modes each in flap bending, lag bending and torsion
rpm	revolutions per minute

1 Introduction

In the early eighties, McNulty experimentally investigated the stability of isolated hingeless rotors in forward flight under untrimmed conditions [1]. The strengths of the experiment were structural simplicity and aerodynamically demanding conditions. In fact, the hub-flexure-blade assembly was intentionally designed to approximate closely root-restrained rigid flap-lag blades, and the database included dynamically stalled conditions with advance ratio as high as 0.55 and shaft angle as high as 20^0. Many investigations right until today have been driven by the database in Ref. [1], and these strengths helped isolate the aerodynamic aspects of the stability problem in forward flight (Refs. 2–8), particularly the nonlinear dynamic stall aspects. However, the weaknesses of the experiment were low tip speed and the lack of a swash plate. For example, the collective pitch and shaft angle were the only control inputs, which were manually set prior to each run. This resulted in the unusual flight conditions of unrestricted tip path planes with very large negative coning an-

gles. To remove these weaknesses Maier *et al.* have been conducting experiments since the early '90s on isolated hingeless rotors with torsionally soft blades [9]. Moreover, they also recognize the increasing need for a database on torsionally soft blades in forward flight [9]. Thus, stated explicitly, the primary objective of their tests was to generate trim and aeroelastic stability data for torsionally soft rotors operating at realistic rotational speeds. The rotor is operated under trimmed conditions of minimized 1/rev root flap moment (details to follow). Thus, the database of Ref. [9] includes test results on lag-regressive mode damping, longitudinal and lateral cyclic pitch controls and steady root flap moment.

With this background, we now spell out the objectives of this report:

1. Develop an elastic flap-lag-torsion analysis for required trim conditions of minimized 1/rev root flap moment.

2. Predict trim results of longitudinal and lateral cyclic pitch controls, and steady root flap moment as well as stability results of modal frequencies and lag damping levels.

3. Correlate these predictions with the database of Refs. [9] and [10] and thereby isolate the effects of quasisteady stall, dynamic stall and dynamic wake on trim and stability results.

2   Experimental Rotor

To facilitate discussion and presentation of results, we briefly describe the experimental rotor of Maier *et al.* [9]. It is a soft-inplane hingeless rotor with torsionally soft blades. The 7.5-*ft* rotor has four blades of an NACA 0012 airfoil section. The blade chord is 3.4-*in* and has a rectangular plan form as shown in Fig. 1. Furthermore, the blades have two-degree precone, and zero-degree pretwist and droop. The rotor also has a provision to vary the blade precone. The blade mass-center, tensile, aerodynamic and elastic axes are nearly coincident with the control axis, which is at the quarter-chord point. Table 1 summarizes the rotor properties of the experimental model. The test-model blade including other details of the hub attachment are given in Figs. 1 and 2. Basically, the blade comprises four distinct regions. The first region is a hub section with very high stiffness values. The second
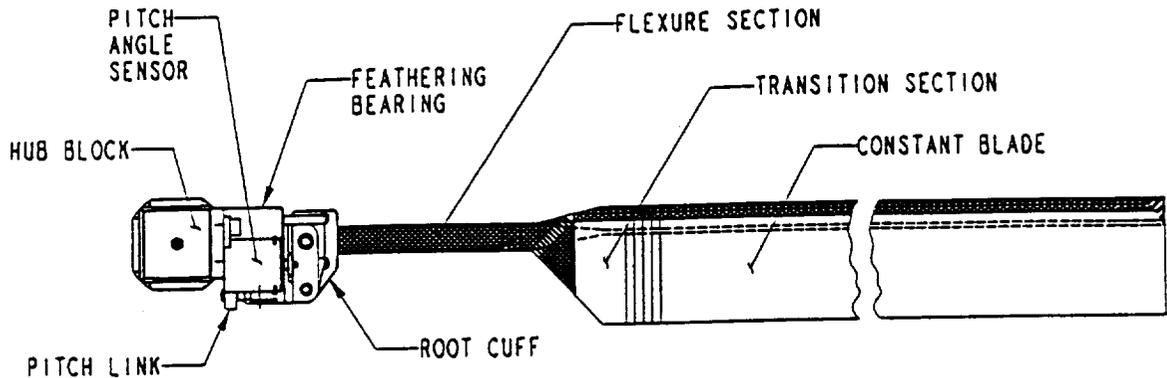
Figure 1: Hub-Flexure-Blade Assembly

region is a root-flexure section, which accommodates the blade flap and lead-lag motions. The third region is a short transition section, which is relatively stiff and provides transition from the blade root-flexure to the airfoil section. The fourth section is the NACA 0012 blade portion. Table 2 details the stiffness and mass distributions in each of these sections. The model is designed so that the test data correspond to stability of isolated rotors. The separation between the lag-regressive mode frequency and the lowest test-stand frequency is $7.1\,Hz$, which is far above the lag regressive-mode frequency.

The collective pitch angle (θ_0) and shaft tilt angle (α_s) are set prior to each run and are known parameters. The rotor is operated trimmed with lateral and longitudinal cyclic pitch controls. The cyclic pitch controls are exercised through a conventional swash plate mechanism that controls pitch on the blade root cuff at a location inboard of the flap-lag flexure motions (Fig. 1). According to Ref. [9], such an arrangement minimizes root-end-kinematic coupling effects and thus avoids any contamination of the aeroelastic stability data with kinematic nonlinearities. The rotor is operated at 1700 rpm, which in hover gives a Reynolds number of 1.2×10^6 and Mach number of 0.6 at the blade tip.

In hover tests, the rotor is set at the desired speed and collective pitch angle. The shaft angle is set to zero degrees. Then, low-amplitude cyclic excitation is applied and the frequency of the excitation is adjusted until the lag response of the first blade reaches

8

Table 1: Details of the Experimental Rotor

Number of blades	4
Airfoil section	NACA 0012
Hover blade-tip Mach number at 1700 rpm	0.6
Hover blade-tip Reynolds number at 1700 rpm	1.2×10^6
Rotor radius, *ft*	3.75
Blade chord, *in*	3.4
Nonrotating fundamental flap frequency, *Hz*	4.499
Nonrotating fundamental lead-lag frequency, *Hz*	14.405
Nonrotating fundamental torsion frequency, *Hz*	64.362
Blade precone, *deg*	0.0 and 2.0
Blade pretwist, *deg*	0.0
Blade droop, *deg*	0.0
Blade sweep, *deg*	0.0

Table 2: Structural Properties of the Experimental Rotor

Region	Radius r/R	Mass $(slugs/ft)$	Polar Inertia/ft $(slugs-ft)$	Flap stiffness $(lbs-ft^2)$	Lag stiffness $(lbs-ft^2)$	Torsion stiffness $(lbs-ft^2)$	Axial stiffness (lbs)
1	0.000–0.104	—	—	very high	very high	very high	very high
2	0.104–0.216	0.00575	2.42×10^{-6}	52.076	268.58	22.188	1.022×10^{6}
3	0.216–0.306	0.00981	4.12×10^{-5}	—	—	—	—
4	0.306–1.000	0.00633	3.57×10^{-5}	53.728	1698. 90	26.395	4.796×10^{5}

10
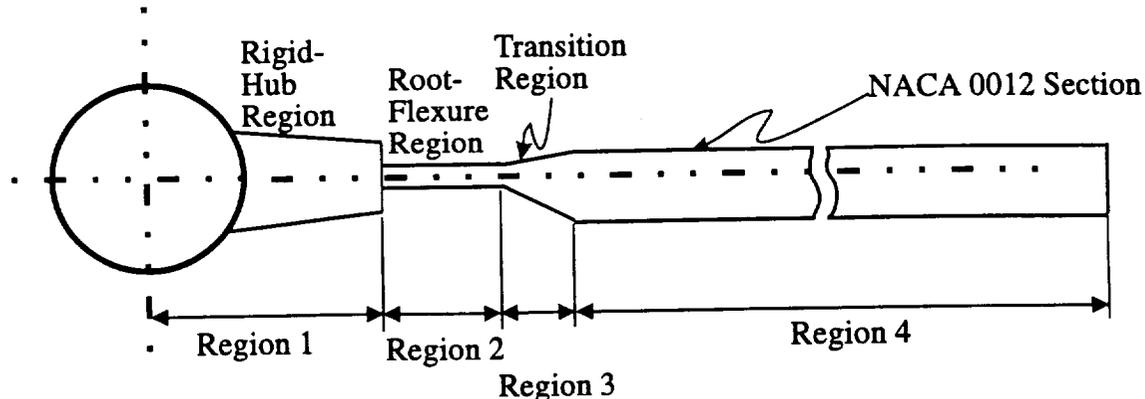
Figure 2: Schematic of Hub-Flexure-Blade Assembly

a maximum. To obtain a strong decaying transient signal, the magnitude of the cyclic excitation is adjusted till the maximum allowable lag response is reached; the maximum allowable is based on the blade structural limit. The excitation is stopped and the ensuing transient signal is recorded for 2 seconds.

In forward-flight tests, the shaft angle is set first and the rotor speed is brought up to the desired value. Then, the collective pitch is set, wind tunnel air speed is increased slowly to the desired forward-flight speed and the cyclic pitch controls are adjusted to maintain low-oscillatory flapping loads. When the desired forward-flight speed is reached, the collective pitch is readjusted to get the desired value and the cyclic pitch controls are further adjusted to minimize the 1/rev flapping moment at the 12% radial station. Then, low-amplitude cyclic excitation is applied. The frequency and magnitude of the excitation are adjusted so that the maximum lead-lag response (but below the structural limit) is attained. The excitation is shut off and the ensuing transient is recorded for 2 seconds. The recorded signals are analyzed using the moving-block analysis technique to obtain modal damping and frequency. Reference [9] provides additional details on the model rotor design and test procedures.

11

3 Analysis

3.1 Elastic Flap-Lag-Torsion Equations

The flap-lag-torsion equations of motion are nonlinear partial differential equations, which are given in Ref. [6]. We use a Galerkin-type scheme to transform these partial differential equations into a set of ordinary differential equations in terms of generalized coordinates. Orthogonal, nonrotating normal modes are used, which are developed numerically with mass and stiffness distributions identical to those of the experimental rotor; see Table 2. *In-vacuo* conditions are assumed; that is, without aerodynamics and the frequencies are obtained from an eigenanalysis. A Mykelstad-type approach is followed in generating the modes. As shown in Table 2, the stiffness distributions for the transition region (region 3) are not given because these distributions change continuously over this region and it was not possible to measure them [9]. In the present correlation work, we assume a linear variation for stiffness properties in that region while computing the mode shapes. Figures 3–5 show the nonrotating mode shapes for the first five flap bending, lag bending and torsion deflection modes. These modes are normalized with a tip deflection of one. The corresponding five nonrotating frequencies are tabulated in Table 3. Using these normal modes, the equations of motion are transformed into a set of modal equations in terms of the generalized coordinates. The Galerkin-type integrals associated with this transformation for spatial dependency are evaluated numerically and are given in Ref. [6].

3.2 Aerodynamics

The airfoil aerodynamics is based on the quasisteady stall, dynamic stall and dynamic stall and wake theories, which are described in Ref. [6]. As in the experimental rotor, the analytical model has four blades of an NACA 0012 airfoil section. The airfoil-section quasisteady stall characteristics are determined following Ref. [11] at a Reynolds number of 1.8×10^6. For the lift model, the quasisteady lift coefficient C_{z_s} and extrapolated lift coefficient C_{z_l} are given by

$$C_{z_l} = a \sin \alpha \cos \alpha \qquad 0^0 \leq \alpha \leq 180^0 \tag{1a}$$

$$C_{z_s} = C_{z_l} \qquad 0^0 \leq \alpha \leq \alpha_{ss}^0 \tag{1b}$$

12
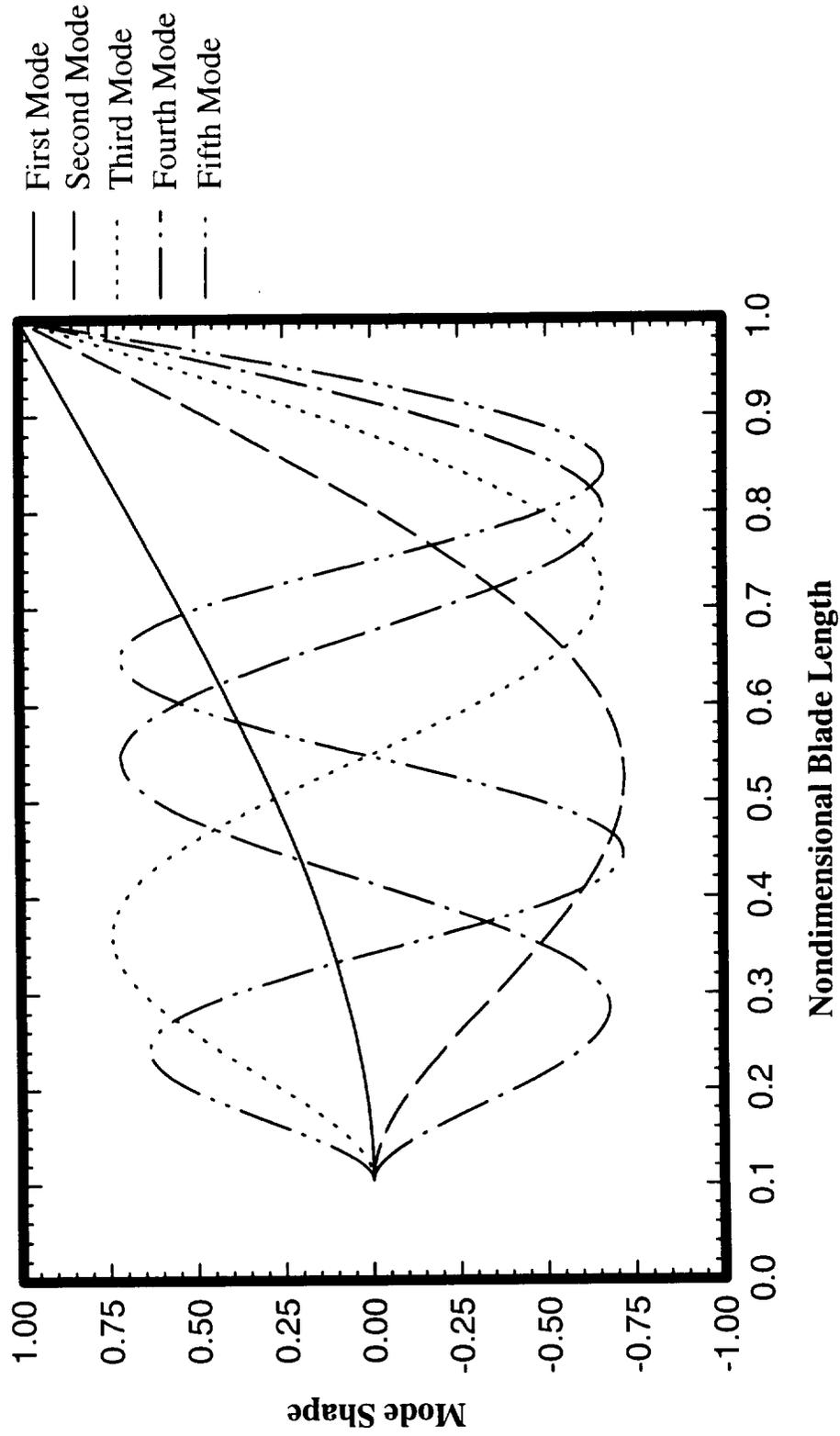
Figure 3: Nonrotating Flap Bending Modes for the Experimental Rotor Blade

13
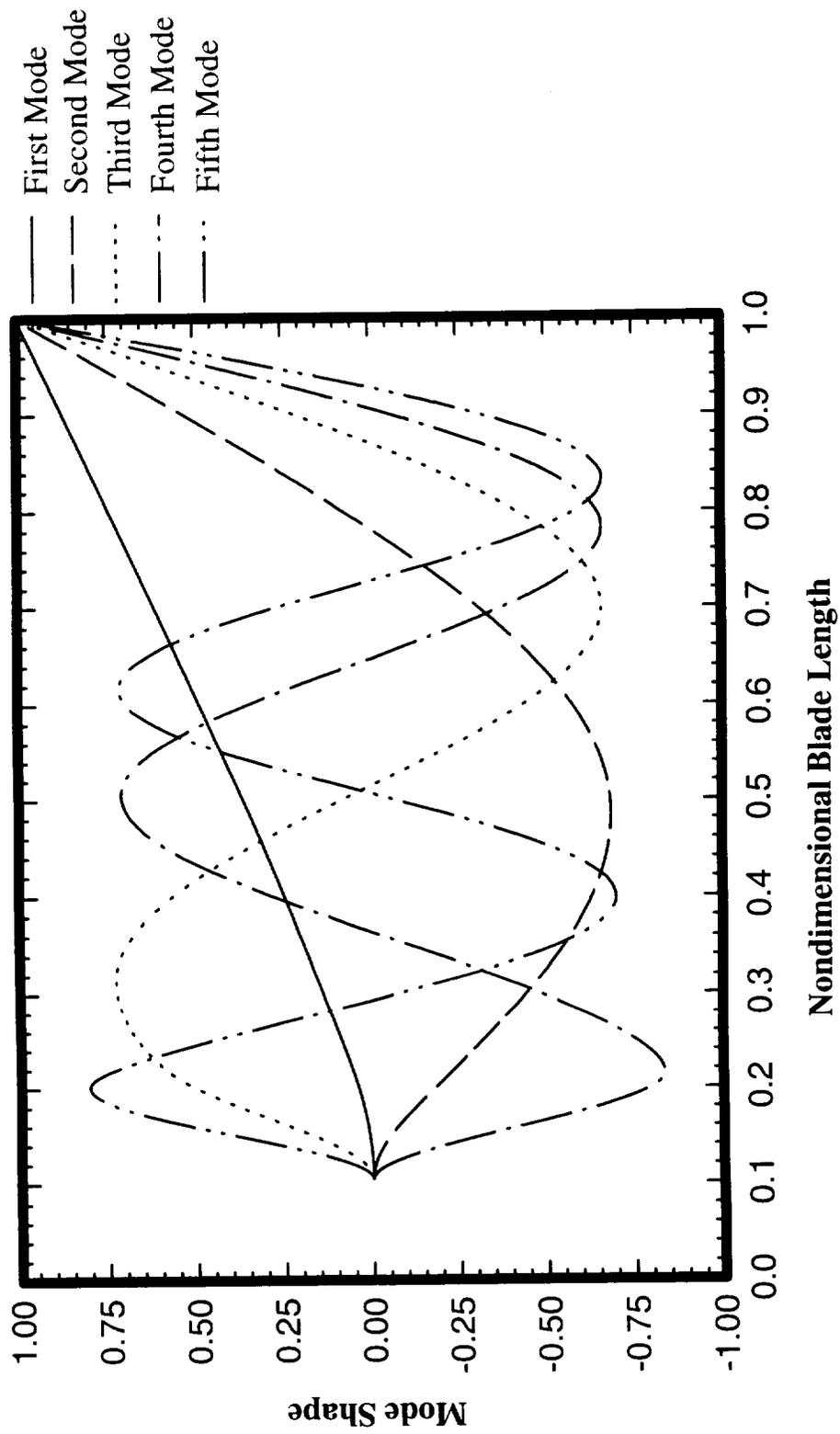
Figure 4: Nonrotating Lag Bending Modes for the Experimental Rotor Blade
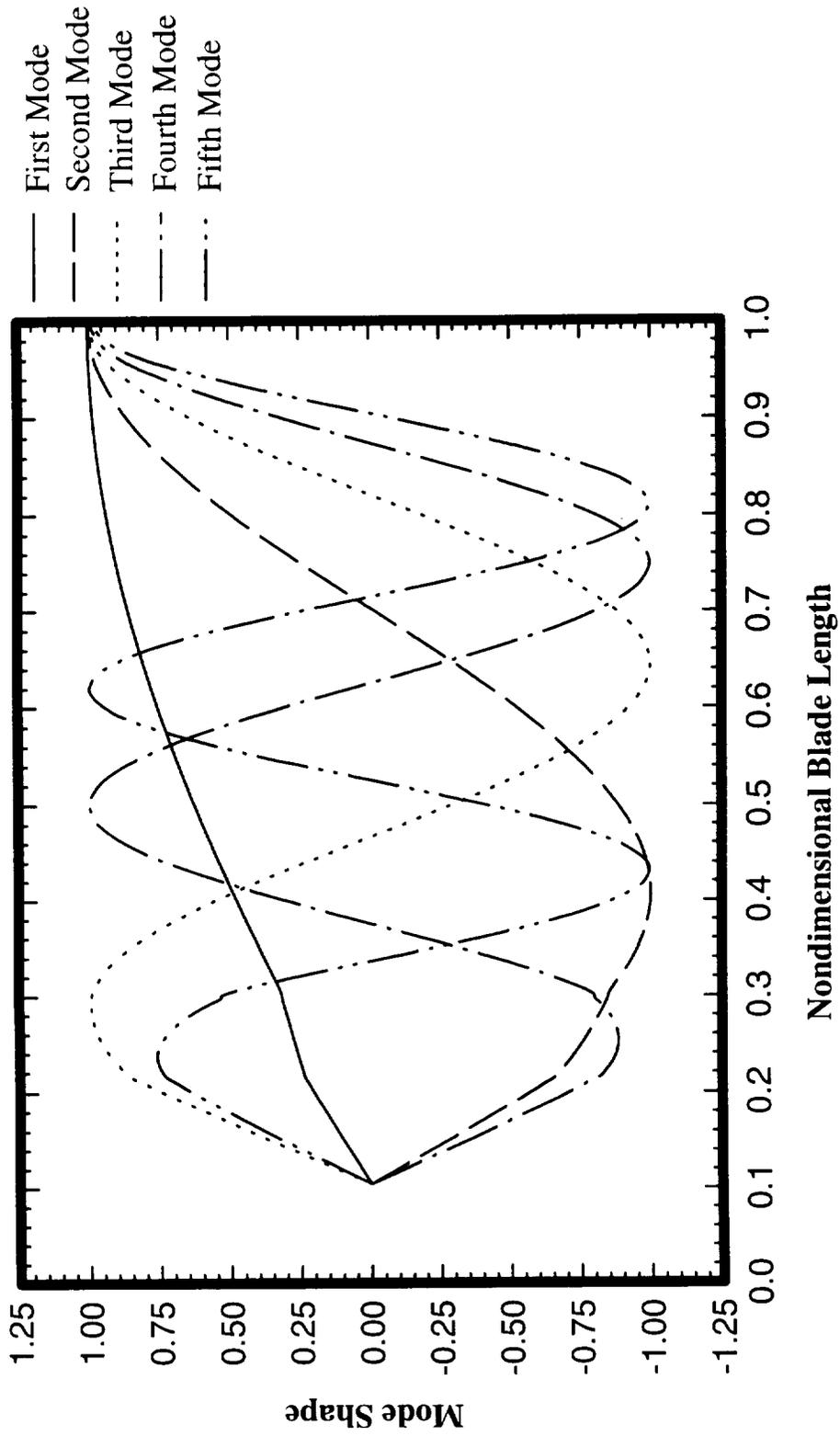
Figure 5: Nonrotating Torsion Modes for the Experimental Rotor Blade

15

Table 3: Predicted and Measured Nonrotating Frequencies for the Experimental Rotor

Mode	Flap		Lag		Torsion	
	Predicted Hz	Measured Hz	Predicted Hz	Measured Hz	Predicted Hz	Measured Hz
First	4.640	4.499	14.178	14.405	65.334	64.362
Second	28.358	26.775	131.407	—	193.683	—
Third	78.000	73.893	378.882	—	321.975	—
Fourth	151.618	—	719.131	—	457.828	—
Fifth	251.911	—	1199.689	—	601.468	—

16

$$C_{z_s} = a \sin \alpha_{ss} \cos \alpha_{ss} \qquad \alpha_{ss}^0 < \alpha < 45^0 \tag{1c}$$

$$C_{z_s} = a \sin \alpha_{ss} \cos \alpha_{ss} \sin 2\alpha \qquad 45^0 \le \alpha \le 135^0 \tag{1d}$$

$$C_{z_s} = -a \sin \alpha_{ss} \cos \alpha_{ss} \qquad 135^0 < \alpha < 166^0 \tag{1e}$$

$$C_{z_s} = C_{z_l} \qquad 166^0 \le \alpha \le 180^0 \tag{1f}$$

where $a = 6.28$ and $\alpha_{ss} = 14^0$. Figure 6 shows the quasisteady lift coefficient for $0^0 \le \alpha \le 360^0$. It also includes a comparison with the static test data from Ref. [11] and with the extrapolated linear-lift coefficient C_{z_l} according to Eq. (1a).

For the drag model, the quasisteady drag coefficient C_{d_s} and the constant drag coefficient C_{d_0} are:

$$C_{d_0} = 0.01 \tag{2a}$$

$$C_{d_s} = 1.05 - (1.05 - C_{d_0}) \cos 2\alpha \qquad 0^0 < \alpha < 360^0 \tag{2b}$$

The variations of these coefficients for $0^0 \le \alpha \le 360^0$ are shown in Fig. 7, which also includes test data from Ref. [11].

For the pitching moment model, the quasisteady moment coefficient C_{m_s} is given by

$$C_{m_s} = C_{m_0} \qquad 0^0 \le \alpha \le \alpha_{ss}^0 \tag{3a}$$

$$C_{m_s} = C_{m_0} - 0.0582257 \tan^{-1}(\alpha - \alpha_{ss}) \qquad \alpha_{ss}^0 < \alpha \le 20^0 \tag{3b}$$

$$C_{m_s} = C_{m_0} - 0.55 \sin(\alpha - 20^0) - 0.0842201 \cos(\alpha - 20^0) \qquad 20^0 < \alpha \le 101.2941^0 \tag{3c}$$

$$C_{m_s} = C_{m_0} - 0.55641 \cos[0.75(\alpha - 101.2941^0)] \qquad 101.2941^0 < \alpha \le 170^0 \tag{3d}$$

$$C_{m_s} = 0.3461497[0.1(\alpha - 170^0)] \qquad 170^0 < \alpha \le 180^0 \tag{3e}$$

where $C_{m_0} = 0.0$. Figure 8 shows the variation of C_{m_s} from Eqs. (3a)–(3e) and the test data from Ref. [11].

The dynamic stall parameters used in the ONERA stall model are the same as those for an NACA 23012 airfoil section; these are given in the Appendix; for additional details, see Ref. [6]. To include wake effects, we use the finite-state three-dimensional wake model, which is based on six harmonics and three radial shape functions for each harmonic; this leads to 39 wake states. Although a detailed convergence study with respect to the number of harmonics and radial shape functions has not been carried out in forward flight, the wake model should provide results close to the converged values for $C_T/\sigma_s < 0.05$.
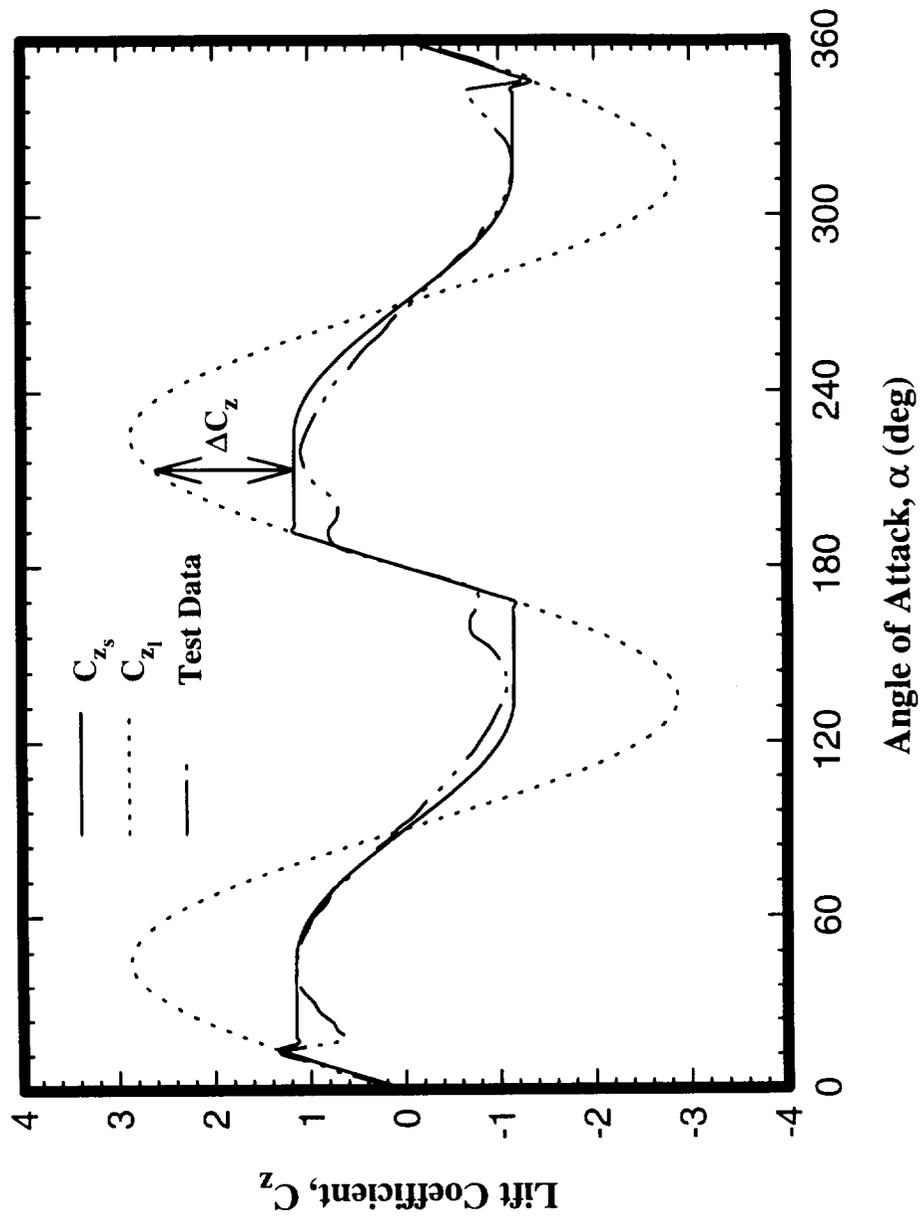
Figure 6: Variation of Airfoil Lift Coefficient for an NACA 0012 Airfoil Section
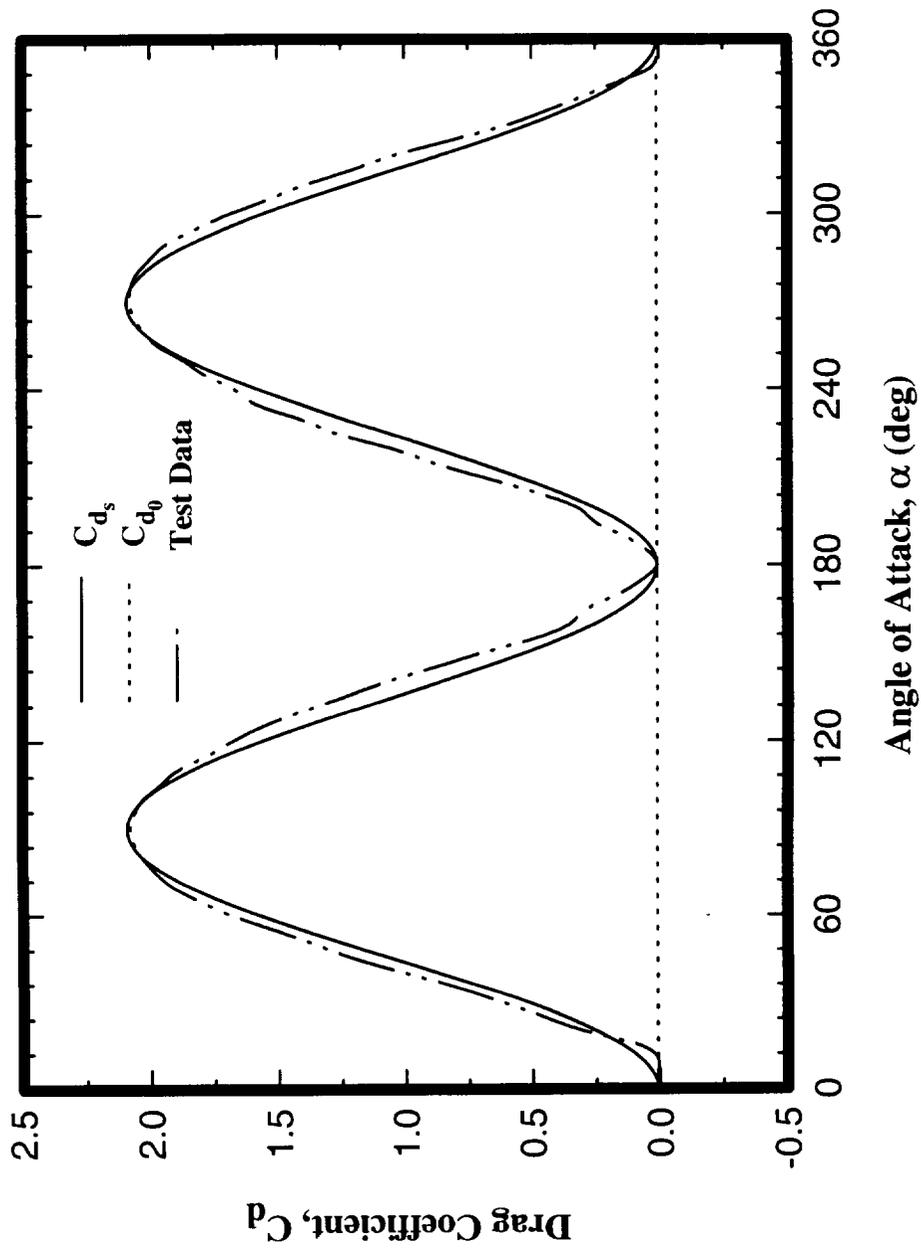
Figure 7: Variation of Airfoil Drag Coefficient for an NACA 0012 Airfoil Section
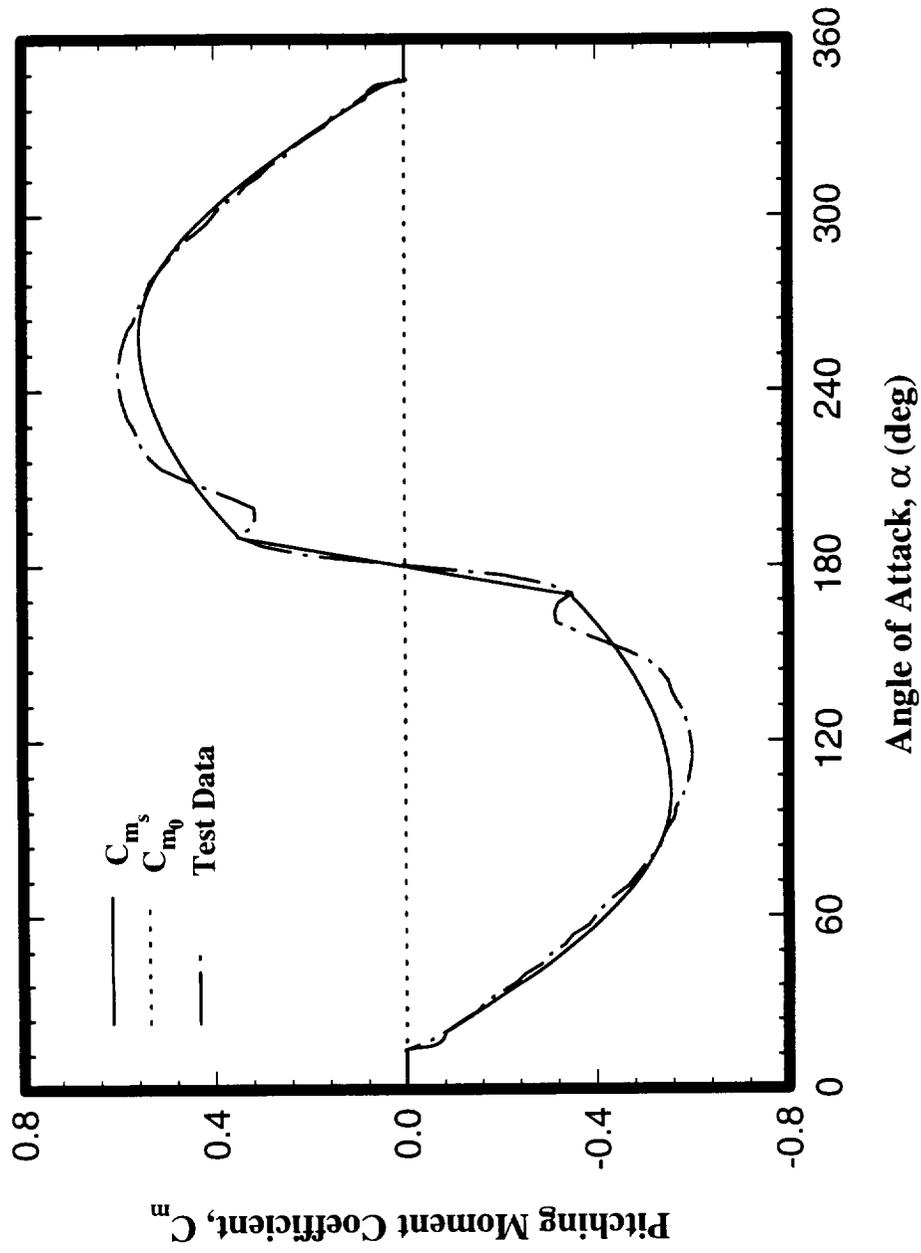
Figure 8: Variation of Airfoil Pitching Moment Coefficient for an NACA 0012 Airfoil Section

3.3 Trim Analysis

As detailed earlier, the collective pitch and shaft tilt angles are known control inputs. Therefore, trim analysis per se refers to finding the lateral and longitudinal cyclic control inputs for minimized 1/rev flap moment at the 12% radial station and to finding the corresponding initial conditions for the periodic responses. The trim analysis is based on the shooting method with damped Newton Iteration, which generates the FTM as a byproduct. The modal damping levels and frequencies are obtained from the eigenvalues and eigenvectors of the FTM [12]. This analysis still requires two additional trim equations that satisfy the required trim conditions of minimized 1/rev flap moment at $0.12R$. These trim equations are given in the next section.

3.3.1 Flap Moment Equations

Consider a generic material point on the blade at a radial location $\bar{x}$ from the hinge offset. As shown in Fig. 9, the generic point is subjected to inertial, aerodynamic and centrifugal forces. It is expedient to express the components of each of these forces in the undeformed blade coordinate system xyz. Let $\mathcal{L}_u$ and $\mathcal{L}_w$ represent the total horizontal and vertical forces parallel and perpendicular to the undeformed x-coordinate, respectively. Similarly, let $\mathcal{M}_v$ represent the total moment acting parallel to the undeformed y-coordinate and let $\bar{e}_f$ represent the $0.12R$ radial location about which the flap moment is computed. Following Ref. [13], we predict the flap moment by the force-integration approach, in which the sectional forces and moments are integrated over the blade span to obtain the total moment. Therefore, the total flap moment is given by

$$\mathcal{M}(\bar{e}_f, t) = \int_{\bar{e}_f}^{\bar{\ell}} \left\{ \mathcal{L}_u \left[\overline{w}(\bar{x}) - \overline{w}(\bar{e}_f) \right] - \mathcal{L}_w (\bar{x} - \bar{e}_f) + \mathcal{M}_v \right\} d\bar{x} \tag{4}$$

Now, we express the forces and moment in Eq. (4) as a sum of inertial and aerodynamic components. The inertial component includes contribution from the centrifugal forces as well. Thus we have

$$\mathcal{L}_u = \mathcal{L}_u^I + \mathcal{L}_u^A, \quad \mathcal{L}_w = \mathcal{L}_w^I + \mathcal{L}_w^A, \quad \mathcal{M}_v = \mathcal{M}_v^I + \mathcal{M}_v^A \tag{5}$$

21

where the superscripts I and A indicate that the contributions are of inertial and aerodynamic origin. Substituting Eq. (5) in Eq. (4), we get

$$
\begin{aligned}
\mathcal{M}(\overline{e}_f, t) &= \int_{\overline{e}_f}^{\overline{\ell}} \left\{ \mathcal{L}_u^I \left[\overline{w}(\overline{x}) - \overline{w}(\overline{e}_f) \right] - \mathcal{L}_w^I (\overline{x} - \overline{e}_f) + \mathcal{M}_v^I \right\} d\overline{x} \\
&\quad + \int_{\overline{e}_f}^{\overline{\ell}} \left\{ \mathcal{L}_u^A \left[\overline{w}(\overline{x}) - \overline{w}(\overline{e}_f) \right] - \mathcal{L}_w^A (\overline{x} - \overline{e}_f) + \mathcal{M}_v^A \right\} d\overline{x} \\
&= \mathcal{M}(\overline{e}_f)_{\text{inertial}} + \mathcal{M}(\overline{e}_f)_{\text{aerodynamic}}
\end{aligned}
\tag{6}
$$

The expressions for sectional inertial forces, $\mathcal{L}_u^I$ and $\mathcal{L}_w^I$, can be derived by applying Newton's second law:

$$
\mathcal{L}^I = \mathcal{L}_u^I \mathbf{i} + \mathcal{L}_v^I \mathbf{j} + \mathcal{L}_w^I \mathbf{k} = \iint \rho_s \mathbf{a} \, d\eta \, d\xi
\tag{7}
$$

Substituting for the blade acceleration relative to an inertial frame and performing the cross-sectional integrals, we get [6]

$$
\mathcal{L}_u^I = -\overline{m} \left[-2\dot{\overline{v}}\Omega - (\overline{x} + \overline{e}_h)\Omega^2 + \beta_{pc}\overline{w}\Omega^2 \right]
\tag{8}
$$

$$
\mathcal{L}_w^I = -\overline{m} \left[\ddot{\overline{w}} + 2\beta_{pc}\Omega\dot{\overline{v}} + \beta_{pc}\Omega^2(\overline{x} + \overline{e}_h) \right]
\tag{9}
$$

In deriving the above equations, we neglect the axial deformation.

Similarly, the sectional inertial moments can be derived from

$$
\mathcal{M}^I = \mathcal{M}_u^I \mathbf{i} + \mathcal{M}_v^I \mathbf{j} + \mathcal{M}_w^I \mathbf{k} = -\iint \rho_s \mathbf{s} \times \mathbf{a} \, d\eta \, d\xi
\tag{10}
$$

where $\mathbf{s}$ represents the moment arm (see Ref. [6]). Sustituting for $\mathbf{s}$ and $\mathbf{a}$ and performing the cross-sectional integrals, we get

$$
\begin{aligned}
\mathcal{M}_v^I &= -\overline{m} \left[-\ddot{\overline{v}}' + \Omega^2\overline{v}' \right] \left\{ (\overline{k}_{m_2}^2 - \overline{k}_{m_1}^2) \sin\theta\cos\theta \right\} \\
&\quad - \overline{m} \left[-\ddot{\overline{w}}' + 2\Omega\dot{\theta}' + \Omega^2\overline{w}' + \Omega^2\beta_{pc} \right] \left\{ \overline{k}_{m_2}^2 \sin^2\theta + \overline{k}_{m_1}^2 \cos^2\theta \right\}
\end{aligned}
\tag{11}
$$

Substituting Eqs. (8), (9) and (11) for the inertial part in Eq. (6) and after nondimensionalization, we get

$$
\frac{\mathcal{M}_{\text{inertial}}}{\rho_\infty b\Omega^2 R^4} = \overline{\mathcal{M}}(e_f, \psi)_{\text{inertial}} = \frac{6a}{\gamma} \int_{e_f}^{\ell} \{ 2m\,\dot{v}\,[w(x) - w(e_f)]
$$

22
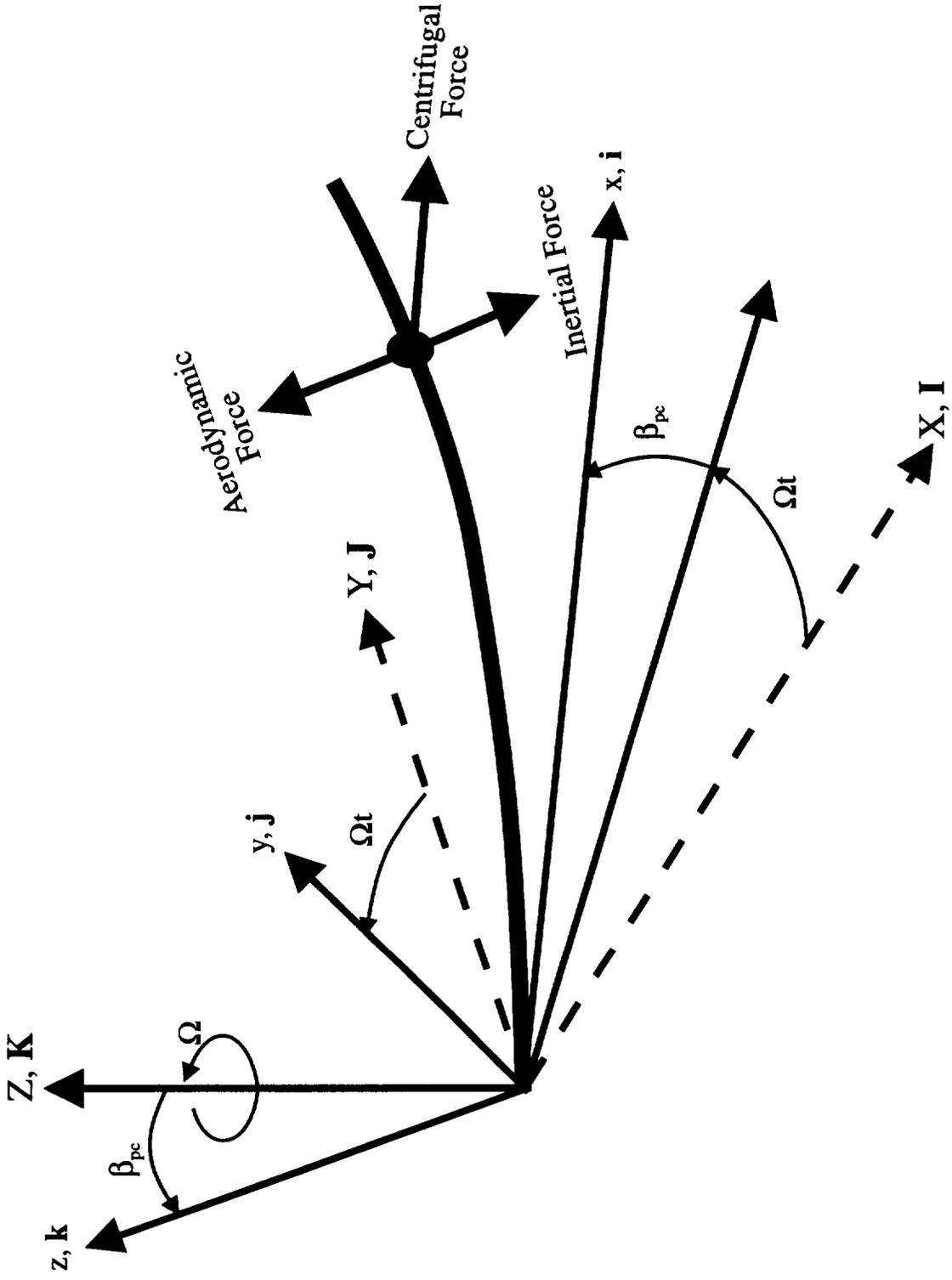
Figure 9: Blade Coordinate Systems and Sectional Forces

23

$$+ \quad m(x + e_h)\left[w(x) - w(e_f)\right]$$

$$- \quad \beta_{pc} m\, w\left[w(x) - w(e_f)\right] + m\,\ddot{w}(x - e_f) + 2\beta_{pc} m\,\dot{v}(x - e_f)$$

$$+ \quad \beta_{pc} m(x - e_f)(x + e_h) + m k_{m_2}^2 \ddot{v}' \sin\theta\cos\theta - m k_{m_2}^2 v' \sin\theta\cos\theta$$

$$+ \quad m k_{m_2}^2 \ddot{w}' \sin^2\theta - m k_{m_2}^2 w' \sin^2\theta - 2\dot{\theta}' m k_{m_2}^2 \sin^2\theta$$

$$- \quad m k_{m_2}^2 \beta_{pc} \sin^2\theta \} \, dx \tag{12}$$

Now, substitution of modal expansions for w and v in Eq. (12) gives

$$
\begin{aligned}
\overline{\mathcal{M}}(e_f, \psi)_{\text{inertial}} &= \frac{6a}{\gamma} \Big\{ \sum_{i=1}^{NOM} \sum_{j=1}^{NOM} \left[2FM_{ij}^1 \dot{V}_i W_j - \beta_{pc} FM_{ij}^2 W_i W_j \right] \\
&\quad + \sum_{i=1}^{NOM} \left[FM_i^3 W_i + FM_i^4 \ddot{W}_i + 2\beta_{pc} FM_i^5 \dot{V}_i \right] \\
&\quad + \sum_{i=1}^{NOM} \left[FM_i^6 \sin\theta\cos\theta \ddot{V}_i - FM_i^6 \sin\theta\cos\theta V_i \right] \\
&\quad + \sum_{i=1}^{NOM} \left[FM_i^7 \sin^2\theta \ddot{W}_i - FM_i^7 \sin^2\theta W_i \right] \\
&\quad + \beta_{pc} FM^8 - (2\dot{\theta} + \beta_{pc}) \sin^2\theta FM^9 \Big\}
\end{aligned}
\tag{13}
$$

The aerodynamic contribution to flap moment is obtained from sectional aerodynamic forces and moments, which are calculated at the mid point of each aerodynamic element. Hence, we use a force-summation scheme instead of integrating the forces and moments along the length of the blade. Thus, in terms of sectional aerodynamic forces and moments, the flap moment due to aerodynamics can be obtained as

$$
\begin{aligned}
\frac{\mathcal{M}(\overline{e}_f, \psi)_{\text{aerodynamic}}}{\rho_\infty b \Omega^2 R^4} &= \overline{\mathcal{M}}(e_f, \psi)_{\text{aerodynamic}} \\
&= \sum_{n=1}^{NEL} \left[\mathcal{L}_u^A \{ w(x_f) - w(e_f) \} - \mathcal{L}_w^A x_f + \mathcal{M}_v^A \right]_n \Delta x_n
\end{aligned}
\tag{14}
$$

In the above equation, x_{f_n} and Δx_n represent the radial distance of the mid point from the $0.12R$ radial station and the length of the n-th aerodynamic element, respectively. Expressing Eq. (14) in terms of sectional aerodynamic forces and moments, we get

$$\mathcal{L}_u^A = -(v' L_v + w' L_w) \tag{15}$$

24

$$\mathcal{L}_w^A = L_w \tag{16}$$

$$\mathcal{M}_v^A = v'M_\phi \tag{17}$$

where L_v, L_w and M_ϕ are the sectional aerodynamic forces and moments described in Ref. [6]. Substitution of Eqs. (15)–(17) into Eq. (14) gives

$$
\begin{aligned}
\overline{\mathcal{M}}(e_f, \psi)_{\text{aerodynamic}} &= \sum_{n=1}^{NEL} [-(v'L_v + w'L_w)[w(x_f) - w(e_f)] \\
&\quad - L_w x_f + v'M_\phi]_n \Delta x_n
\end{aligned}
\tag{18}
$$

Substituting modal expansions, we rewrite the above equation as

$$
\begin{aligned}
\overline{\mathcal{M}}(e_f, \psi)_{\text{aerodynamic}} &= \sum_{n=1}^{NEL} \{ \sum_{i=1}^{NOM} \sum_{j=1}^{NOM} \left[-FM_{ij}^{10} V_i W_j L_{v_n} - FM_{ij}^{11} W_i W_j L_{w_n} \right] \\
&\quad + \sum_{i=1}^{NOM} FM_i^{12} V_i M_{\phi_n} - L_{w_n} x_{f_n} \}
\end{aligned}
\tag{19}
$$

Similarly, with the substitution of Eqs. (13) and (19) in Eq. (6), the total flap moment at the radial location e_f is given by

$$
\begin{aligned}
\overline{\mathcal{M}}(e_f) &= \frac{6a}{\gamma} \{ \sum_{i=1}^{NOM} \sum_{j=1}^{NOM} \left[2FM_{ij}^1 \dot{V}_i W_j - \beta_{pc} FM_{ij}^2 W_i W_j \right] \\
&\quad + \sum_{i=1}^{NOM} \left[FM^3 W_i + FM_i^4 \ddot{W}_i + 2\beta_{pc} FM_i^5 \dot{V}_i \right] \\
&\quad + \sum_{i=1}^{NOM} \left[FM_i^6 \sin\theta\cos\theta \ddot{V}_i - FM_i^6 \sin\theta\cos\theta V_i \right] \\
&\quad + \sum_{i=1}^{NOM} \left[FM_i^7 \sin^2\theta \ddot{W}_i - FM_i^7 \sin^2\theta W_i \right] \\
&\quad + \beta_{pc} FM^8 - (2\dot{\theta} + \beta_{pc})\sin^2\theta FM^9 \} \\
&\quad + \sum_{n=1}^{NEL} \{ \sum_{i=1}^{NOM} \sum_{j=1}^{NOM} \left[-FM_{ij}^{10} V_i W_j L_{v_n} - FM_{ij}^{11} W_i W_j L_{w_n} \right] \\
&\quad + \sum_{i=1}^{NOM} FM_i^{12} V_i M_{\phi_n} - L_{w_n} x_{f_n} \}
\end{aligned}
\tag{20}
$$

The Galerkin-type integrals accounting for spatial contributions are detailed in Ref. [6].

3.3.2 Trim Equations

Equation (20) gives the total flap moment acting at the radial station e_f; that is, at the 12% radial station. To obtain the 1/rev components of flap moment, we expand Eq. (20) in terms of Fourier series as

$$\overline{\mathcal{M}}(e_f, \psi) = \overline{\mathcal{M}}_0 + \sum_{n=1}^{\infty} \left[\overline{\mathcal{M}}_{nc} \cos(n\psi) + \overline{\mathcal{M}}_{ns} \sin(n\psi) \right] \tag{21}$$

For $n = 1$, we get

$$\overline{\mathcal{M}}(e_f, \psi) = \overline{\mathcal{M}}_0(e_f) + \overline{\mathcal{M}}_{1c}(e_f) \cos \psi + \overline{\mathcal{M}}_{1s}(e_f) \sin \psi \tag{22}$$

where

$$\overline{\mathcal{M}}_{1c}(e_f) = \frac{1}{\pi} \int_0^{2\pi} \overline{\mathcal{M}}(e_f, \psi) \cos \psi \, d\psi \tag{23}$$

$$\overline{\mathcal{M}}_{1s}(e_f) = \frac{1}{\pi} \int_0^{2\pi} \overline{\mathcal{M}}(e_f, \psi) \sin \psi \, d\psi \tag{24}$$

Therefore, the required trim conditions are

$$\overline{\mathcal{M}}_{1c}(e_f) = \frac{1}{\pi} \int_0^{2\pi} \overline{\mathcal{M}}(e_f, \psi) \cos \psi \, d\psi = 0 \tag{25}$$

$$\overline{\mathcal{M}}_{1s}(e_f) = \frac{1}{\pi} \int_0^{2\pi} \overline{\mathcal{M}}(e_f, \psi) \sin \psi \, d\psi = 0 \tag{26}$$

Thus, Eqs. (25) and (26) represent the trim equations, which are solved together with the response periodicity conditions.

3.3.3 Steady Flap Moment Based on the Curvature Method

Concomitant to the force-integration method, the steady flapping moment at the radial location e_f is also estimated by the curvature method. That is,

$$\overline{\mathcal{M}}(e_f, \psi) = \frac{\mathcal{M}(\overline{e}_f, t)}{m_r \Omega^2 R^2} = \left[\Lambda_2 \frac{\partial^2 w}{\partial x^2} \right]_{e_f} \tag{27}$$

In terms of mode shapes and generalized coordinates, Eq. (27) is expressed as

$$\overline{\mathcal{M}}(e_f, \psi) = \sum_{i=1}^{NOM} \{\Lambda_2 \Psi_i''\}_{e_f} W_i(\psi) \tag{28}$$

Therefore, the steady flap moment is given by

$$\overline{\mathcal{M}}_0(e_f) = \frac{1}{2\pi} \int_0^{2\pi} \overline{\mathcal{M}}(e_f, \psi) \, d\psi \tag{29}$$

26

4 Correlations

We begin the correlation with the nonrotating and rotating frequencies of the blade modes in flap bending, lag bending and torsion. We then correlate with the lag regressive-mode damping, control settings of lateral and longitudinal cyclic pitch angles and finally root flapping moment at the 12% radial station. The baseline parameters for these predictions are identified in Table 4.

Table 3 shows a comparison between the data and predicted *nonrotating* frequencies for flap bending, lag bending and torsion modes; the data are available for three fundamental flap-lag-torsion modes as well as for the second and third modes in flap bending. The correlation is very good in that the maximum error in the prediction with respect to the data hardly exceeds 5.5%. Figure 10 shows the variation of the rotating frequencies with rotor rotational speed Ω for the first two flap-lag-torsion modes. For example, in forward flight $\Omega = 1700$ rpm and the corresponding predictions of the dimensionless (dimensional) rotating frequencies for the fundamental flap-lag-torsion modes are 1.13 (32.02 Hz), 0.7 (19.83 Hz) and 2.86 (81.03 Hz), respectively. The rotating-frequency data are available over a range of Ω values for the first lag mode only, and here as well, the correlation is very good. For completeness, Fig. 10 also includes the nonrotating-frequency data on the fundamental flap-lag-torsion and second-flap bending modes.

Compared to the frequency data in Table 3 and Fig. 10, the data on damping level, cyclic pitch controls and root flapping moment are far more extensive [9, 10]. Accordingly, we present the correlation with these data in three phases: lag regressive-mode damping in the first phase (Figs. 11−14), lateral and longitudinal cyclic pitch controls in the second phase (Figs. 15−22), and finally root flapping moment in the third phase (Figs. 23−30). Following Maier [10], we select four typical test cases with a two-degree precone, for which the updated database is available: three-degree collective with three cases of shaft angle $\alpha_s = 0^0$, 3^0 and 6^0, and 5.9-degree collective with shaft angle $\alpha_s = 6^0$. The analytical predictions are from the quasisteady stall, dynamic stall, and dynamic stall and wake aerodynamic theories. As seen from the data in Fig. 11 ($\theta_0 = 3^0$ and $\alpha_s = 0^0$), the damping increases slowly up to an advance ratio of 0.2, and thereafter it more or less decreases with

27

Table 4: Baseline Parameters for the Experimental Rotor

Lift curve slope, a $(1/rad)$	6.283
Lock number, γ (based on $a = 6.283$)	7.5896
Profile drag coefficient, C_{d_0}	0.01
Camber of NACA 0012 airfoil section, α_c	0.0^0
Lift coefficient at $\alpha = 0$, C_{l_0}	0.0
Pitching moment coefficient at $\alpha = 0$, C_{m_0}	0.0
Quasisteady stall angle of NACA 0012 airfoil section, α_{ss}	$\pm 14^0$
Rotor solidity, σ_s	0.0962
Hinge offset, e_h (in)	4.7
Blade root cutout, r_c (in)	13.76
Blade precone, β_{pc} (deg)	2
Number of aerodynamic elements, NEL	5
Number of modes, NOM	5

increasing μ. Thus, the data exhibit a convex trend of damping variation with μ. Overall, this trend of the data is well predicted by all three theories. Furthermore, the thrust level C_T/σ_s is low throughout the data range ($0 \leq \mu \leq 0.31$); in fact, it is less than 0.03, and for $\mu > 0.2$, it slowly decreases with increasing advance ratio. Given the low-thrust condition, this is expected. The comparative aspects of the correlation by three theories are instructive as well. For example, despite some overprediction for $\mu < 0.05$, the dynamic stall theory provides good correlation throughout. Similarly, the quasisteady stall theory closely follows and underpredicts the dynamic stall theory. This underprediction, though marginal, is consistently observed throughout the data range. Compared to these two theories, the dynamic stall and wake theory provides overall better correlation in that it picks up the finer variations of the experimental data. For example, for $0 \leq \mu \leq 0.05$, it predicts a nearly constant damping level and agrees with the data better, and for $\mu > 0.15$, it gradually follows the dynamic stall theory. The minor differences between the quasisteady stall and dynamic stall theories are due to unsteady lift effects; differences between dynamic stall and dynamic stall and wake theories are due to dynamic wake effects.

In Fig. 12, $\theta_0 = 3^0$ and $\alpha_s = 3^0$. Here as well, the data show a convex trend of

the damping level. The thrust level, which is about 0.01 in hover, increases to 0.022 for $\mu \approx 0.1$ and thereafter decreases to 0.013 at $\mu = 0.31$. Since the thrust level is low, all three aerodynamic theories provide good correlation. In particular, the dynamic stall and wake theory reduces the overpredictions of the quasisteady stall and dynamic stall theories for $\mu < 0.1$ and gradually follows the other two theories for $\mu > 0.2$.

Now, we come to Fig. 13 for $\theta_0 = 3^0$ and $\alpha_s = 6^0$. As seen from the data, the damping level very slowly increases with increasing advance ratio for $\mu \leq 0.1$ and thereafter, it sharply decreases. The thrust level is about 0.01 in hover and increases to a maximum value of 0.017 at $\mu = 0.15$ and thereafter decreases with increasing μ; in fact, it is nearly zero at $\mu = 0.31$. The predictions from the quasisteady stall and dynamic stall theories show slowly increasing damping up to $\mu \approx 0.1$ and thereafter decreasing damping. However, the rate of decrease in damping is small. Moreover, these two theories somewhat overpredict damping for $0 \leq \mu \leq 0.05$. By comparison, the dynamic stall and wake theory improves the correlation for $\mu \leq 0.15$, and for $\mu > 0.15$, it slowly merges with the other two theories. This merging is expected since the thrust level, which is low to begin with, decreases with increasing μ for $\mu > 0.15$ and more or less reduces to zero at $\mu = 0.31$. In summary, the correlation from the dynamic stall and wake theory is adequate for $\mu \leq 0.2$ and needs quantitative corrections for $\mu > 0.2$, which merits further investigation.

Figure 14 is for $\theta_0 = 5.9^0$ and $\alpha_s = 6^0$, and the data are available from a near-hovering condition with $\mu = 0.04$ to a fairly high-speed condition with $\mu = 0.36$. Despite some data scattering around $\mu = 0.05$ and 0.35, the data show that the lag damping increases for $0.04 \leq \mu \leq 0.15$ and decreases for $\mu > 0.15$. We also mention that the thrust level increases from 0.034 in hover to 0.045 at $\mu \approx 0.1$ and decreases to 0.02 at $\mu = 0.36$. Overall, all three theories predict the trend of the data. However, the dynamic stall theory and the quasisteady stall theory (except at $\mu \approx 0.15$) overpredict damping consistently. The differences between the quasisteady stall and dynamic stall theories are mainly due to unsteady lift effects, which increase with increasing collective pitch; see Fig. 13. The dynamic stall and wake theory significantly reduces the overpredictions of the quasisteady stall and dynamic stall theories and thereby improves the correlation. Overall, the dynamic stall and wake theory provides good correlation.

In Figs. 15–17, we present the correlation for lateral cyclic-pitch angle θ_c for $\alpha_s = 0^0$, 3^0 and $\alpha_s = 6^0$, respectively. In all three figures, the data show known trends: θ_c is zero at $\mu = 0.0$, increases suddenly around $\mu = 0.05$ and thereafter slowly decreases with increasing advance ratio. The rate of decrease is higher in Fig. 17 than in Figs. 15 and 16. The predictions from the quasisteady stall and dynamic stall theories are nearly the same for all three values of α_s. And these predictions show that the lateral cyclic pitch required to minimize 1/rev flapping moment is negative and that its magnitude monotonically increases with increasing advance ratio. Although these trends of the predictions are at best consistent with those of the data for $\mu \geq 0.05$, overall they are quantitatively inaccurate. But inclusion of wake effects dramatically improves the correlation, both quantitatively and qualitatively. In particular, the dynamic stall and wake theory predicts the sudden increase around $\mu = 0.05$; that is, in the transition regime when the flow over the rotor disk is associated with a large amount of shed and trailing vorticities. With increasing μ, the dynamic stall and wake theory predicts the decreasing trend of the data. However, this rate of decrease is relatively higher and, hence, the correlation needs further quantitative correction for $\mu > 0.2$.

In Fig. 18, $\theta_0 = 5.9^0$ and $\alpha_s = 6^0$. Here as well, the data show a variation for θ_c similar to that in Figs. 15–17; that is, suddenly increasing at $\mu = 0.05$ and thereafter decreasing with increasing advance ratio. As seen from Fig. 18, both the dynamic stall and quasisteady stall theories fail to predict this variation and are not acceptable. By comparison, the dynamic stall and wake theory not only predicts this variation but also provides good correlation throughout. In summary, Figs. 15–18 show that it is important to include wake effects in the prediction of lateral cyclic pitch angle θ_c and that the correlation in Figs. 16 and 17 merits further improvement at high speed conditions, say, $\mu > 0.25$.

Now, we show the correlation for longitudinal cyclic pitch angle θ_s for four cases: three-degree collective with $\alpha_s = 0^0$, 3^0 and 6^0 in Figs. 19–21, respectively, and 5.9^0-collective with $\alpha_s = 6^0$ in Fig. 22. The data are available from hover to an advance ratio of 0.31 and show that negative θ_s is required for the present trim condition of minimizing 1/rev root flapping moment. As for the details, we begin with Fig. 19; the data show that θ_s is nearly zero up to $\mu \approx 0.05$ and that thereafter it increases (negative) with increasing μ. The predictions from the quasisteady stall and dynamic stall theories show that θ_s essentially

increases (negative) with increasing μ, and the predictions from these two theories are nearly identical. Compared to the data, however, this rate of increase is milder. Moreover, the theories fail to capture the finer details in the variations of θ_s with μ at low advance ratios, say for $\mu < 0.1$. By comparison, the dynamic stall and wake theory predicts that θ_s is nearly constant for $\mu \leq 0.075$. Thereafter, however, it basically follows the other two theories and, all in all, requires a bit of quantitative improvement for $\mu > 0.1$. Similar trends are observed for $\alpha_s = 3^0$ in Fig. 20. In summary, as seen from Figs. 19 and 20, the quasisteady stall and dynamic stall theories provide satisfactory correlation and the dynamic stall and wake theory follows the other two theories with noteworthy improvements for $\mu < 0.05$ and some overpredictions for $0.05 \leq \mu \leq 0.1$.

In Fig. 21 the data show a similar variation for θ_s as in Figs. 19 and 20. Here as well, the predictions from the quasisteady stall and dynamic stall theories agree, and they correlate well with the data. The dynamic stall and wake theory brings the theory closer to the data at $\mu = 0.05$ but it also takes the theory somewhat away from the data at $\mu = 0.1$. For $\mu > 0.1$ it virtually merges with the other two theories. Overall, all three theories provide good correlation.

The data in Fig. 22 show that θ_s (negative) increases with increasing advance ratio. The predictions from the quasisteady stall and dynamic stall theories are nearly identical and provide adequate correlation. The dynamic stall and wake theory slightly improves the correlation for $\mu > 0.25$, but compared to the other two stall theories, it also slightly overpredicts for $\mu < 0.25$. Nevertheless, it also provides adequate correlation overall.

The next four figures show the correlation for the root flap moment from the curvature method. The three-degree collective case with $\alpha_s = 0^0$, 3^0 and 6^0 is covered in Figs. 23−25, respectively, and the 5.9-degree collective case with $\alpha_s = 6^0$ is covered in Fig. 26. The data show that the flap moment increases with increasing μ up to a certain value of μ, say, around 0.2 in Figs. 23 and 24 and around 0.15 in Figs. 25 and 26, and that it decreases thereafter; that is, a convex-type variation. Surprisingly, the predictions from all three theories are nearly identical. Although these three theories predict the trend of the data, they underpredict (negative) flapping moment throughout the data range except in Fig. 25 ($\theta_o = 3^0$ and $\alpha_s = 6^0$) for $\mu > 0.25$ and in Fig. 26 at $\mu \approx 0.36$.

31

Figures 27−30 are based on the force integration method. Here as well, the predictions from the three aerodynamic theories are nearly identical and they consistently underpredict the flapping moment for all values of μ. Nevertheless, they predict the trend of the data for all four cases: $\alpha_s = 0^0$, 3^0 and 6^0 with $\theta_0 = 3^0$ and $\alpha_s = 6^0$ with $\theta_0 = 5.9^0$. Overall, the required quantitative improvements in Figs. 23−30 merit further investigation.

5   Toward Improving the Correlations

We are pursuing a two-pronged approach toward improving the preceding correlation. The first approach is based on improving the dynamic stall characteristics and the results are presented in the next section. The second approach is based on adapting a transient-response analysis [14] somewhat similar to the moving block analysis. It is still in a developmental stage and the research is continuing.

5.1   NACA0012 Dynamic Stall Characteristics

Thus far, the correlations in Figs. 11−30 are based on the dynamic stall parameters of an NACA 23012 airfoil section used in Ref. [3]. It needs to be emphasized that the database on dynamic stall parameters is extremely limited and that the state of the art does not permit an accurate description of these parameters, no matter which airfoil. (Throughout, the quasisteady stall parameters of an NACA 0012 airfoil section are used.) Given this background, it is instructive to study the sensitivity of the preceding correlations to the dynamic stall parameters. That study is presented in Figs. 31−50, in which the correlations are based on the dynamic stall parameters of an NACA 0012 airfoil section used in Ref. [8]. These correlations are also presented in three phases: Figs. 31−34 on lag-regressive mode damping levels, Figs. 35−38 on lateral cyclic pitch control input, Figs. 39−42 on longitudinal cyclic pitch control input, and Figs. 43−50 on root flap moment.

Figures 31−33 show the sensitivity of lag-regressive mode damping to dynamic stall parameters for $\theta_0 = 3^0$ with $\alpha_s = 0^0$, 3^0 and 6^0, respectively, and Fig. 34 for $\theta_0 = 5.9^0$ and $\alpha_s = 6^0$. Overall, Figs. 31−34 show that the sensitivity of the damping predictions to changes in the dynamic stall parameters is negligible. The remaining sets of correlations

further demonstrate this negligible sensitivity, Figs. 35—42 with respect to the lateral cyclic pitch control and longitudinal cyclic pitch control angles and Figs. 43—50 with respect to the root flap moment.

6 Concluding Remarks

The preceding correlation covers a comprehensive database ($0.0 \leq \mu \leq 0.36$, $0^0 \leq \theta_s \leq 5.9^0$, $0^0 \leq \alpha_s \leq 6^0$) on lag damping, lateral and longitudinal cyclic pitch angles and root flap moment. Overall, the dynamic stall and wake theory provides fairly good correlation. A major finding is that inclusion of dynamic wake dramatically improves the correlation for the lateral cyclic pitch angle θ_c. We are continuing this correlation effort to cover additional data received recently from the AFDD and to adapt a transient-response-analysis method of Ref. [14], which provides a means of predicting damping levels and frequencies without perturbations as required in Floquet analysis.

Acknowledgments
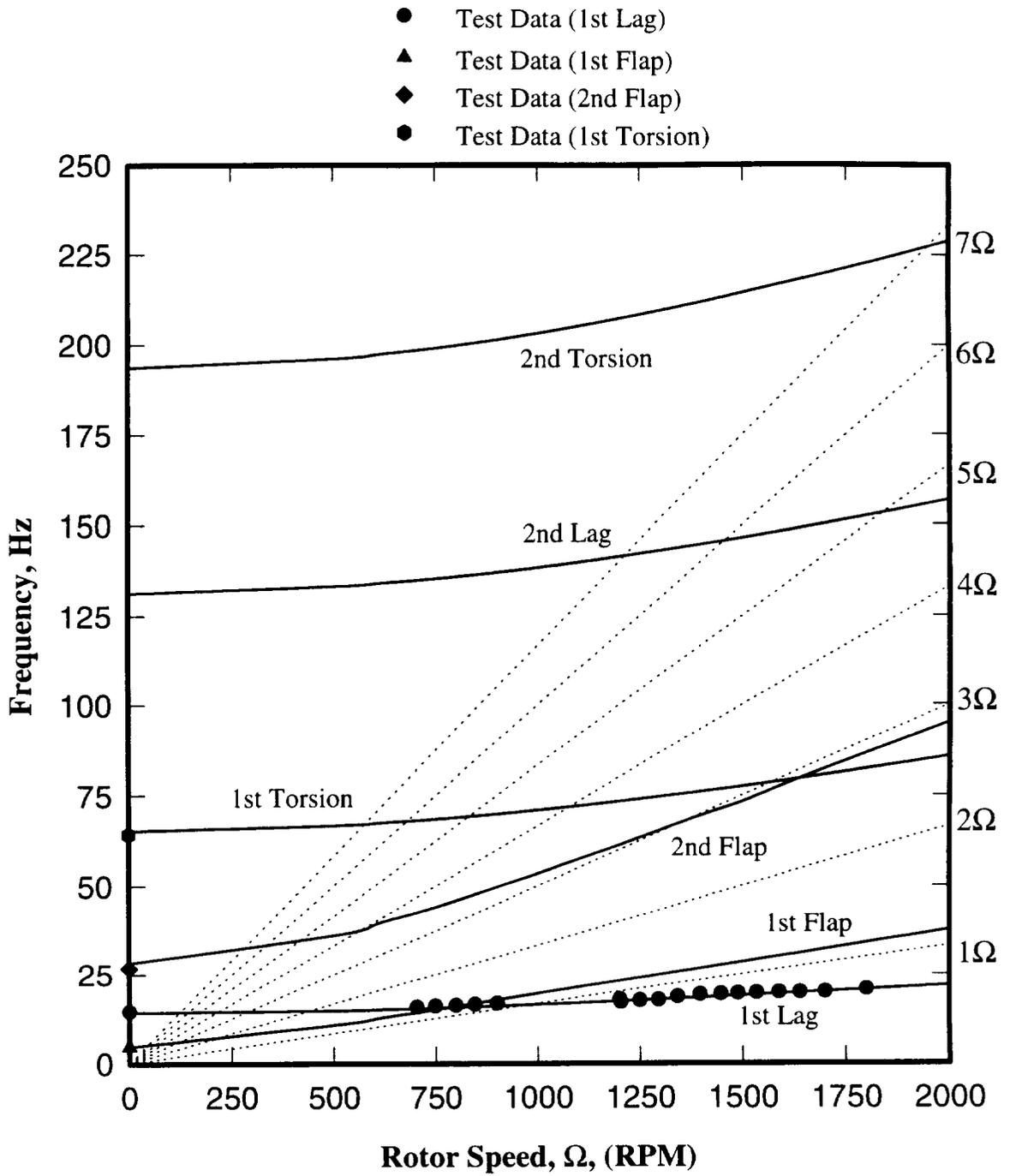
Figure 10: Fan Diagram for Rotating Frequencies of the Experimental Rotor
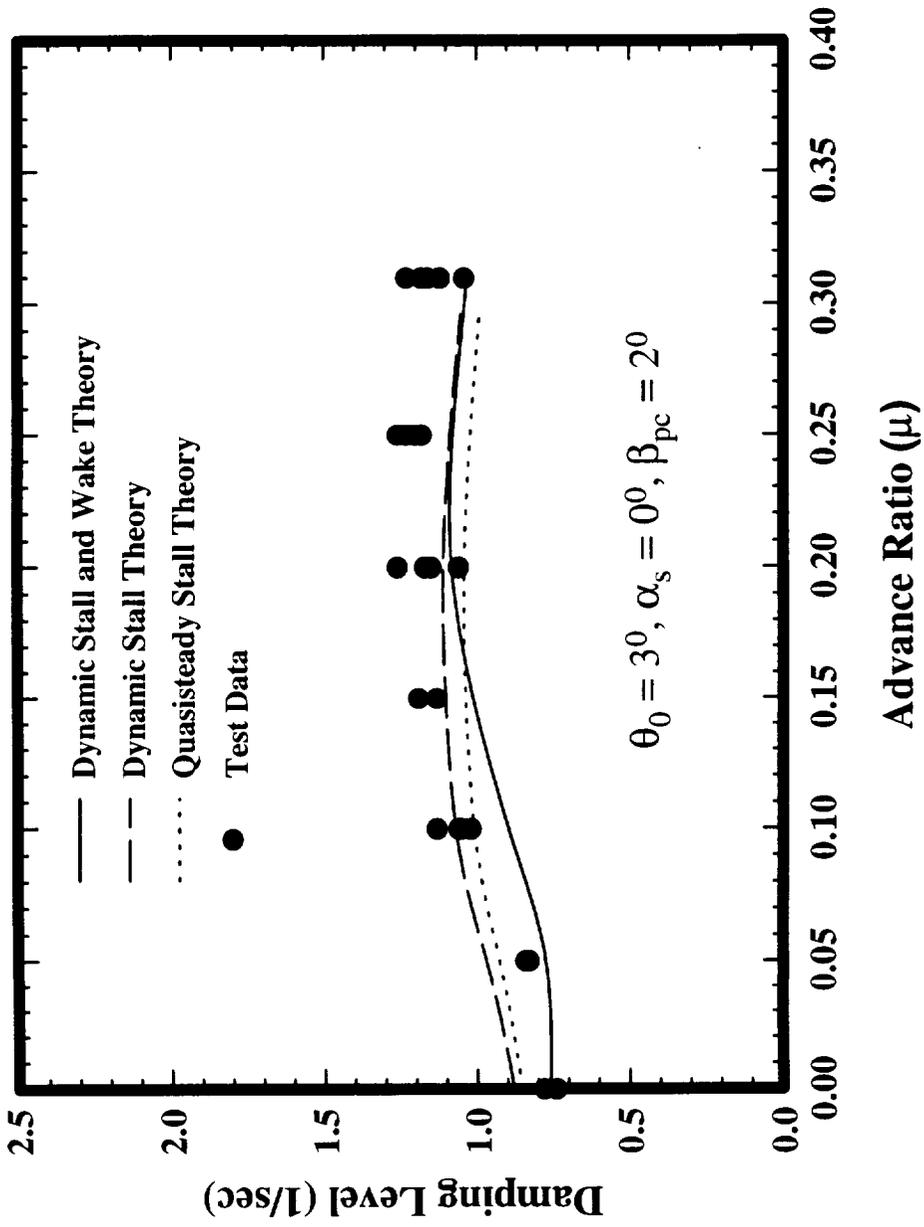
Figure 11: Effects of Aerodynamic Modeling on Lag Damping Correlation

for $\theta_0 = 3^0$ and $\alpha_s = 0^0$
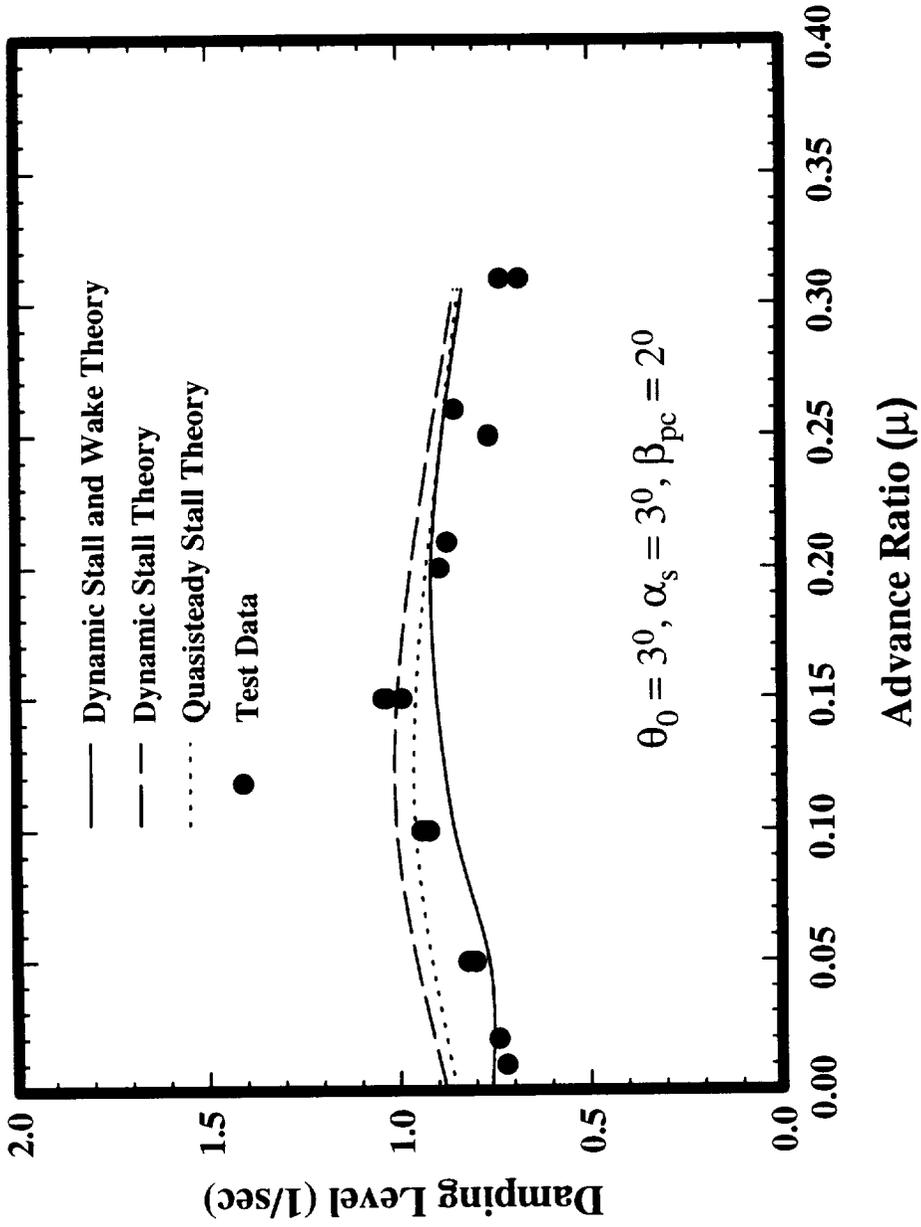
Figure 12: Effects of Aerodynamic Modeling on Lag Damping Correlation
for $\theta_0 = 3^0$ and $\alpha_s = 3^0$

$\theta_0 = 3^0$, $\alpha_s = 3^0$, $\beta_{pc} = 2^0$
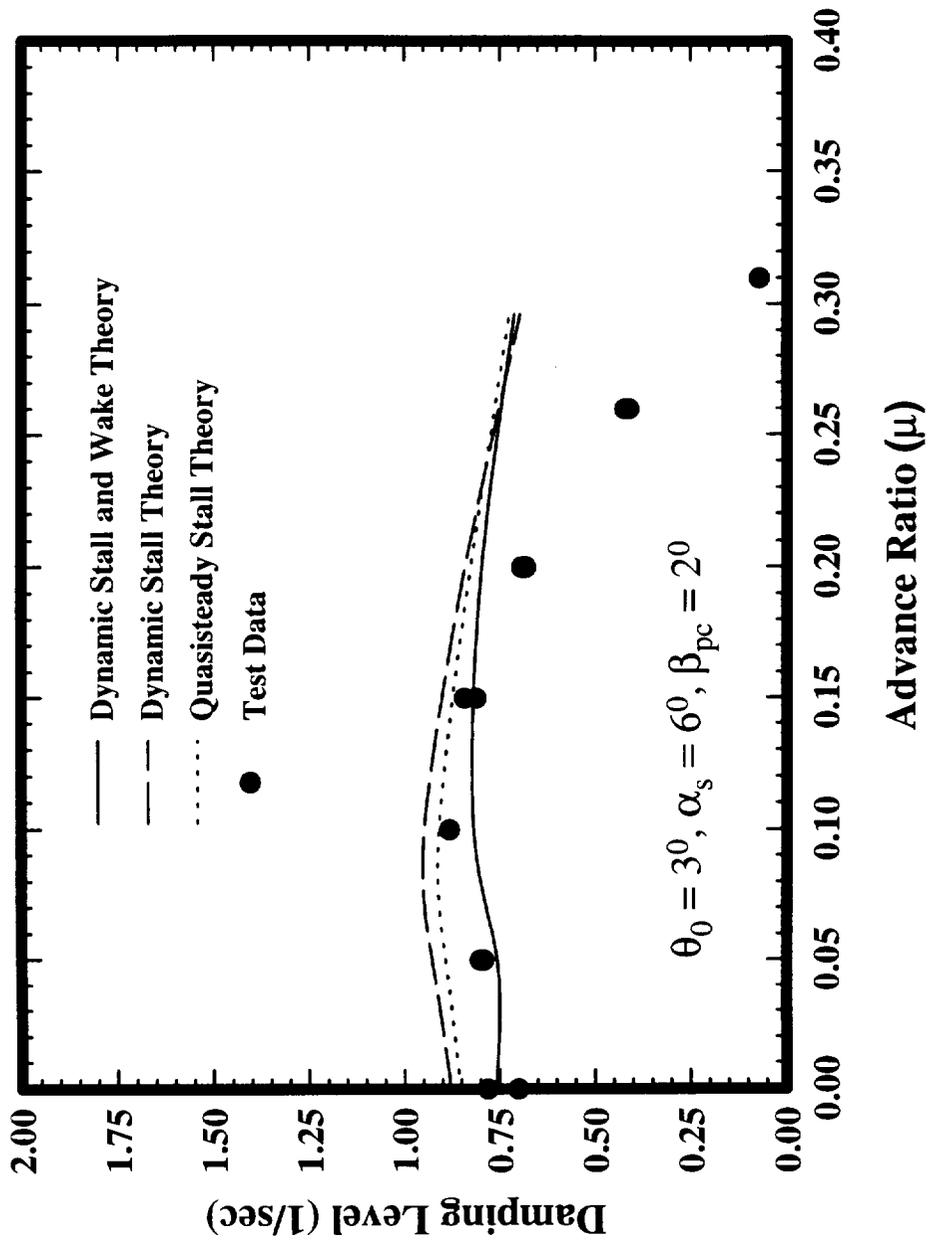
Figure 13: Effects of Aerodynamic Modeling on Lag Damping Correlation for $\theta_0 = 3^0$ and $\alpha_s = 6^0$
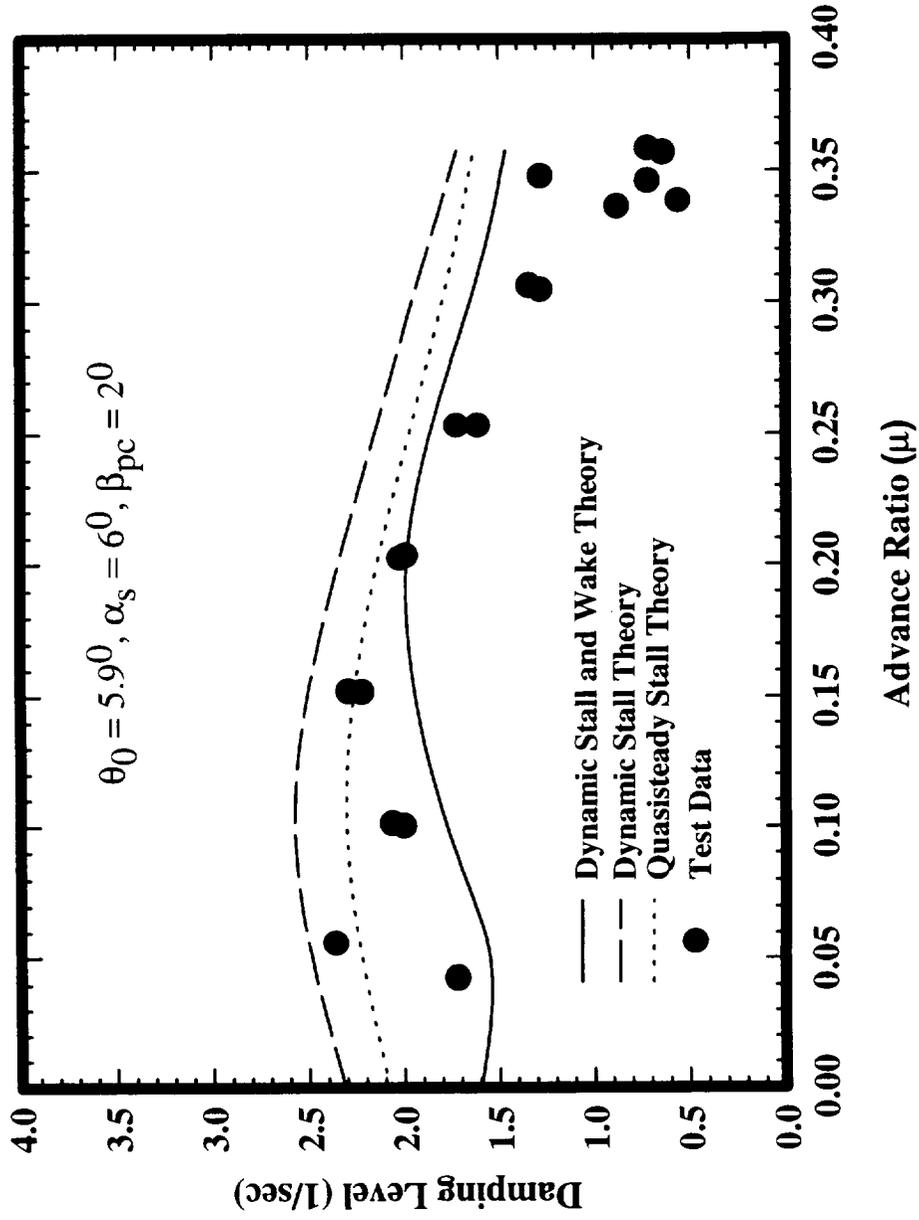
Figure 14: Effects of Aerodynamic Modeling on Lag Damping Correlation

for $\theta_0 = 5.9^0$ and $\alpha_s = 6^0$

38
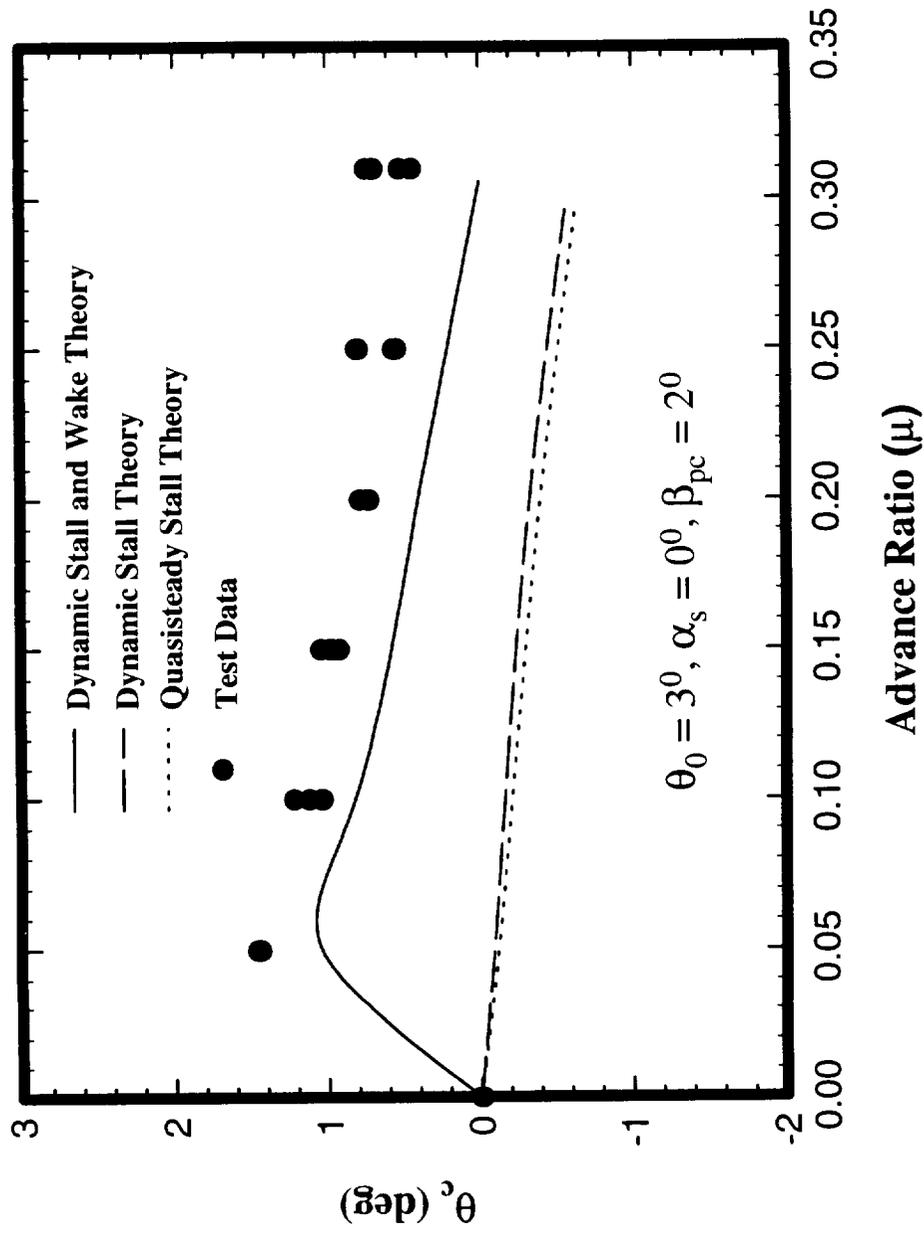
Figure 15: Effects of Aerodynamic Modeling on Lateral-Cyclic Pitch Correlation for $\theta_0 = 3^0$ and $\alpha_s = 0^0$

$\theta_0 = 3^0$, $\alpha_s = 0^0$, $\beta_{pc} = 2^0$

Legend:
— Dynamic Stall and Wake Theory
– – Dynamic Stall Theory
···· Quasisteady Stall Theory
● Test Data

Y-axis: θ_c (deg)
X-axis: Advance Ratio (μ)
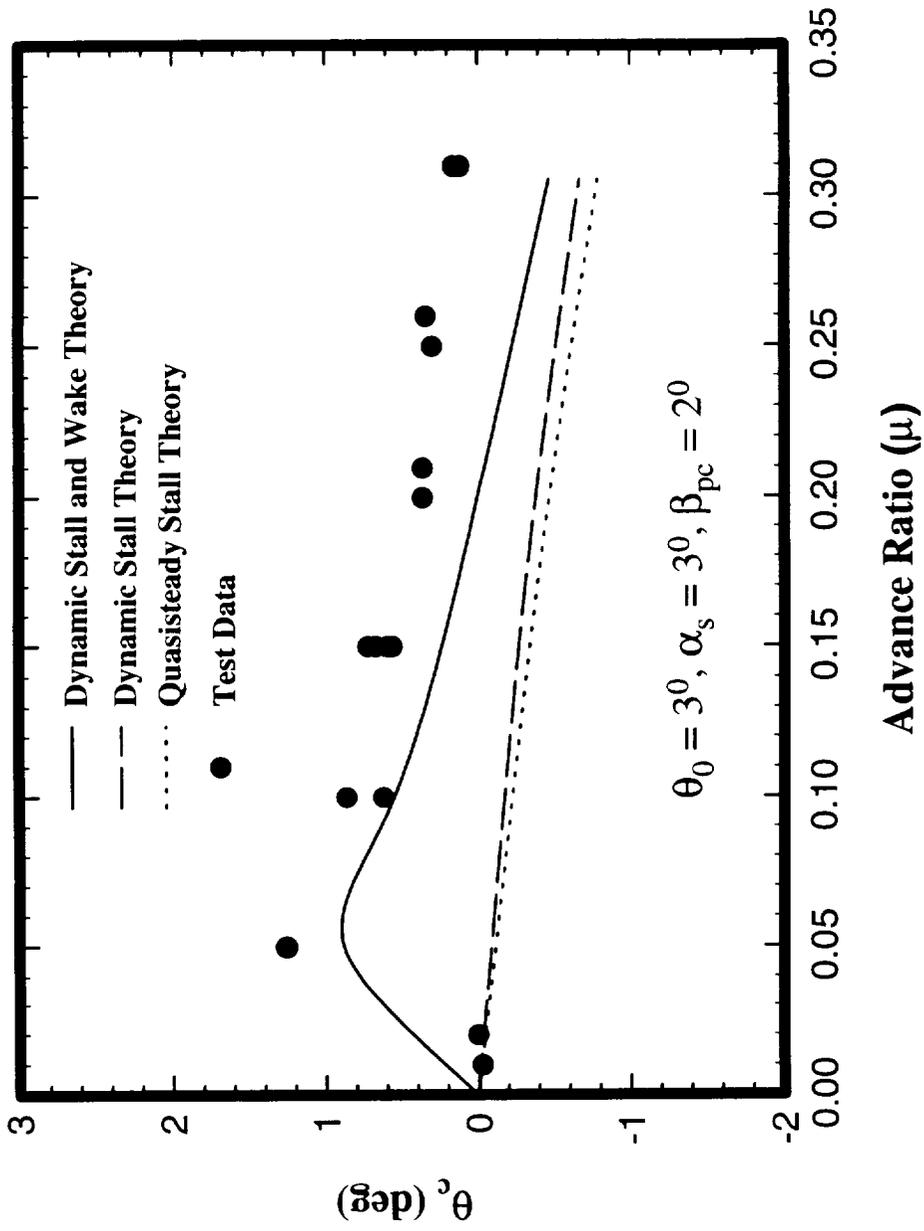
Figure 16: Effects of Aerodynamic Modeling on Lateral-Cyclic Pitch Correlation for $\theta_0 = 3^0$ and $\alpha_s = 3^0$
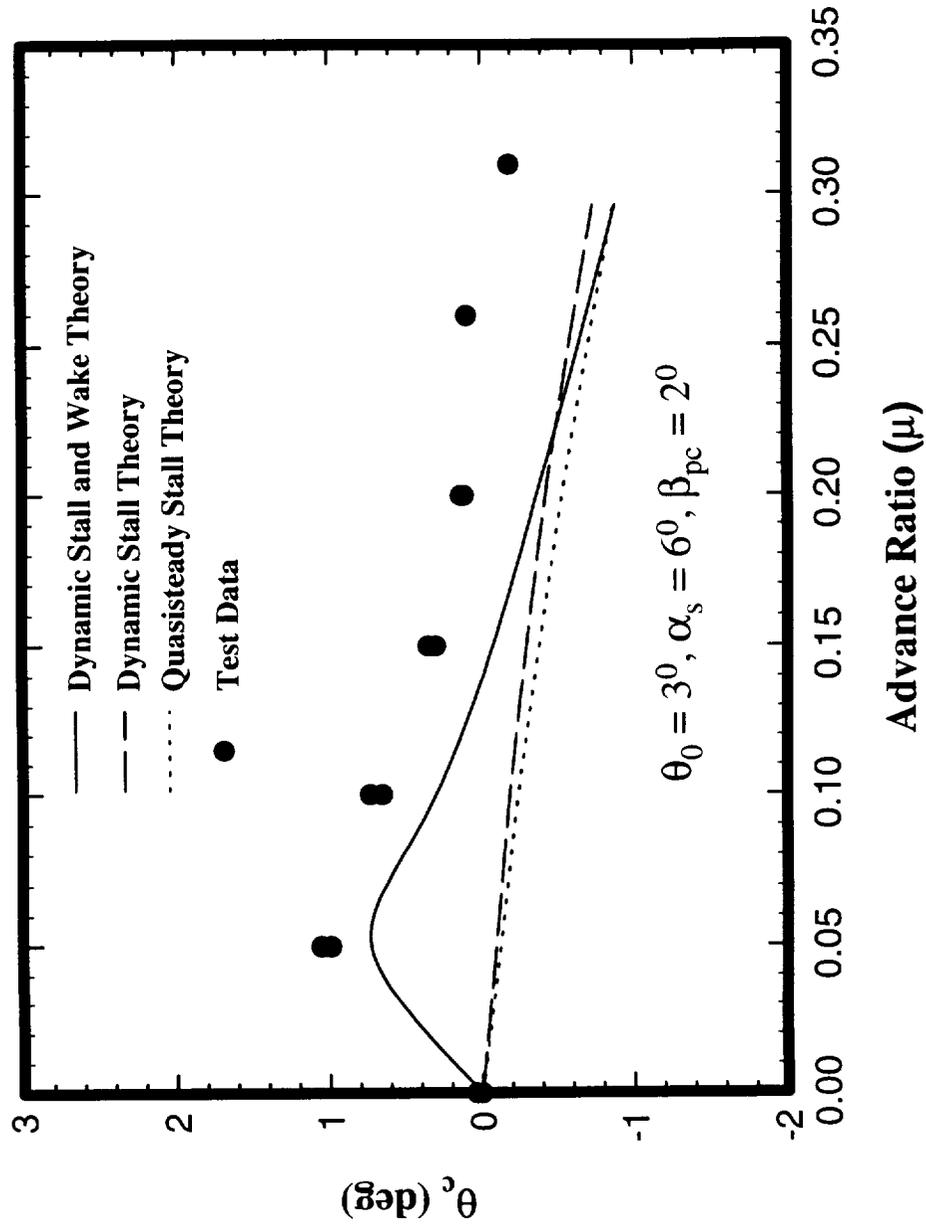
Figure 17: Effects of Aerodynamic Modeling on Lateral-Cyclic Pitch Correlation
for $\theta_0 = 3^0$ and $\alpha_s = 6^0$
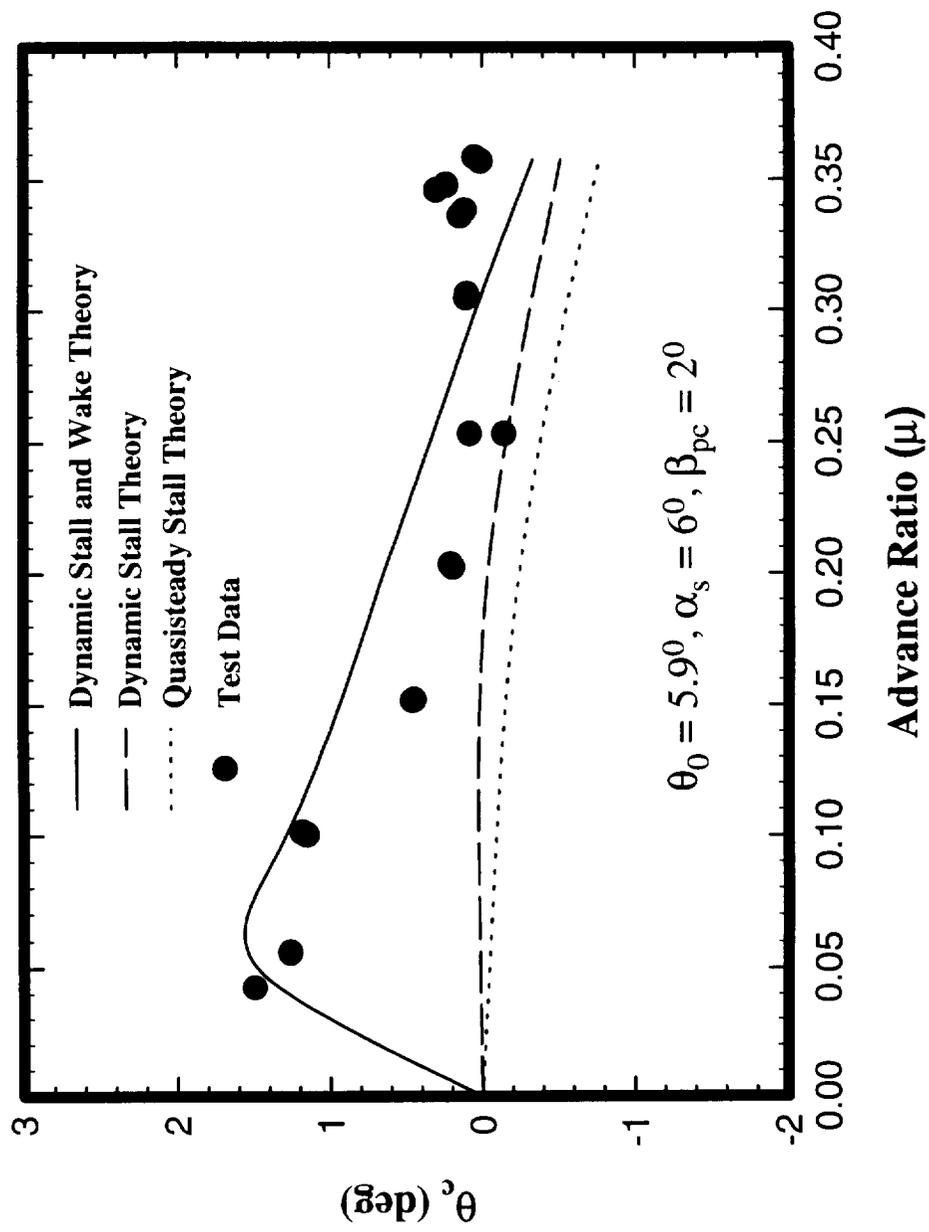
Figure 18: Effects of Aerodynamic Modeling on Lateral-Cyclic Pitch Correlation

for $\theta_0 = 5.9^0$ and $\alpha_s = 6^0$
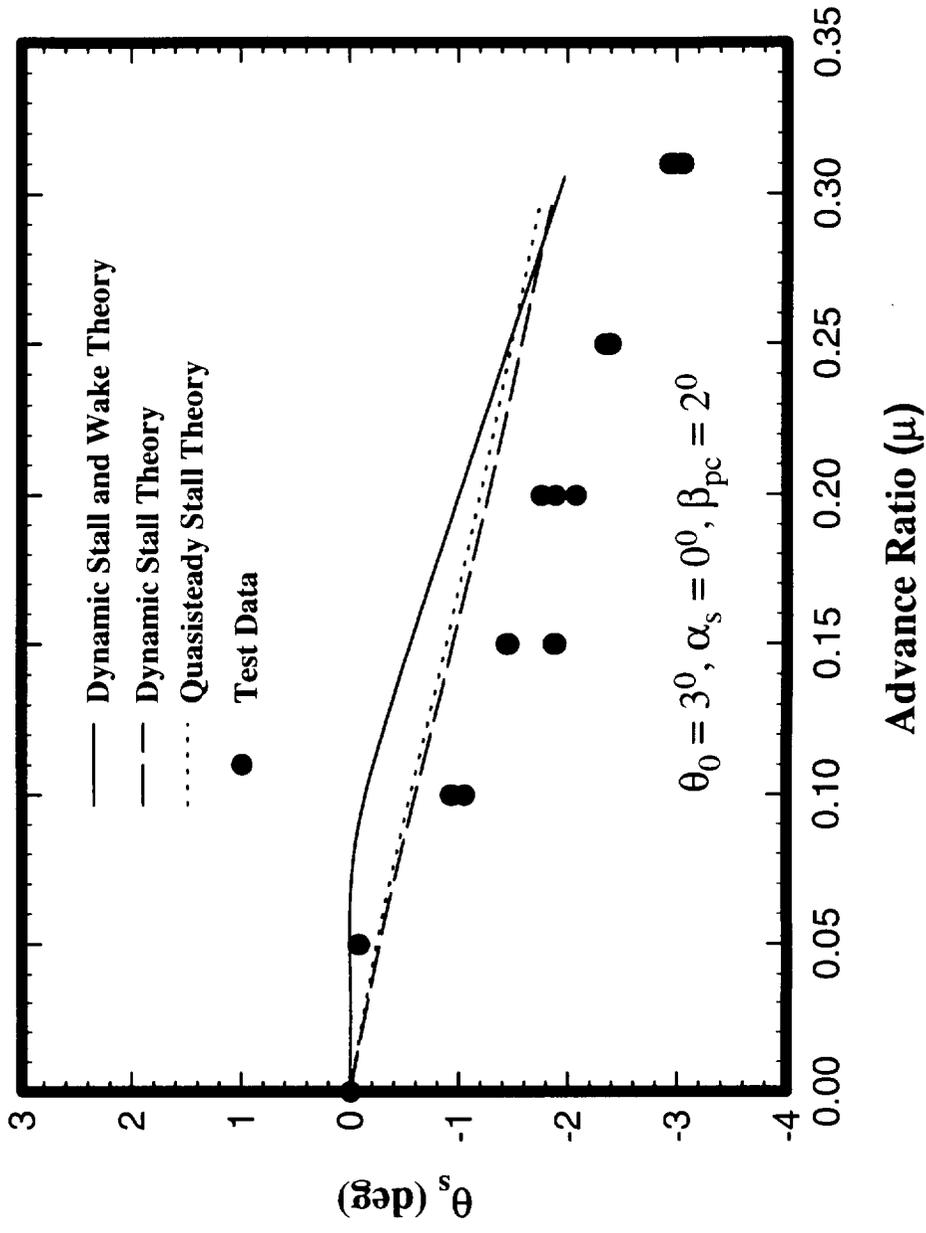
Figure 19: Effects of Aerodynamic Modeling on Longitudinal-Cyclic Pitch Correlation for $\theta_0 = 3^0$ and $\alpha_s = 0^0$
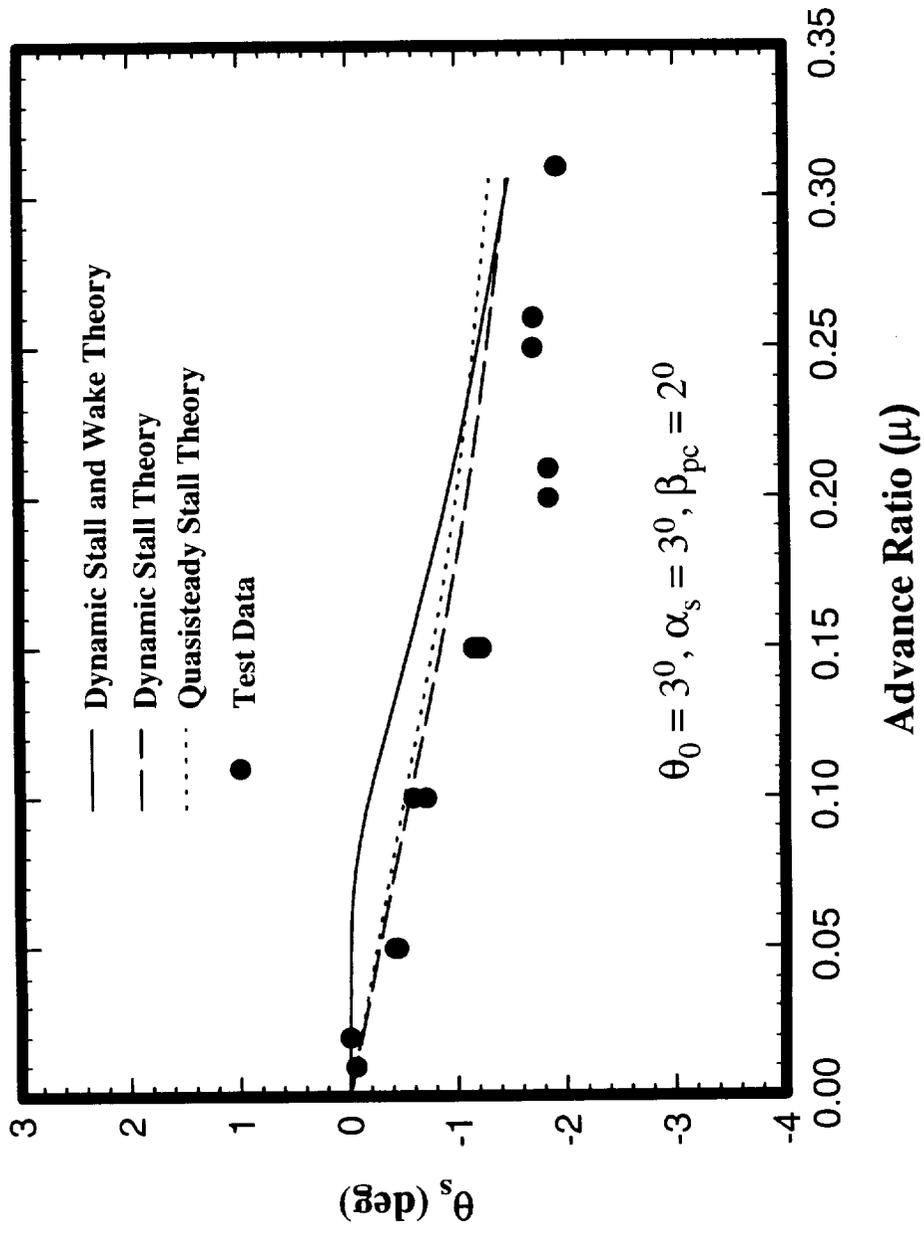
Figure 20: Effects of Aerodynamic Modeling on Longitudinal-Cyclic Pitch Correlation for $\theta_0 = 3^0$ and $\alpha_s = 3^0$
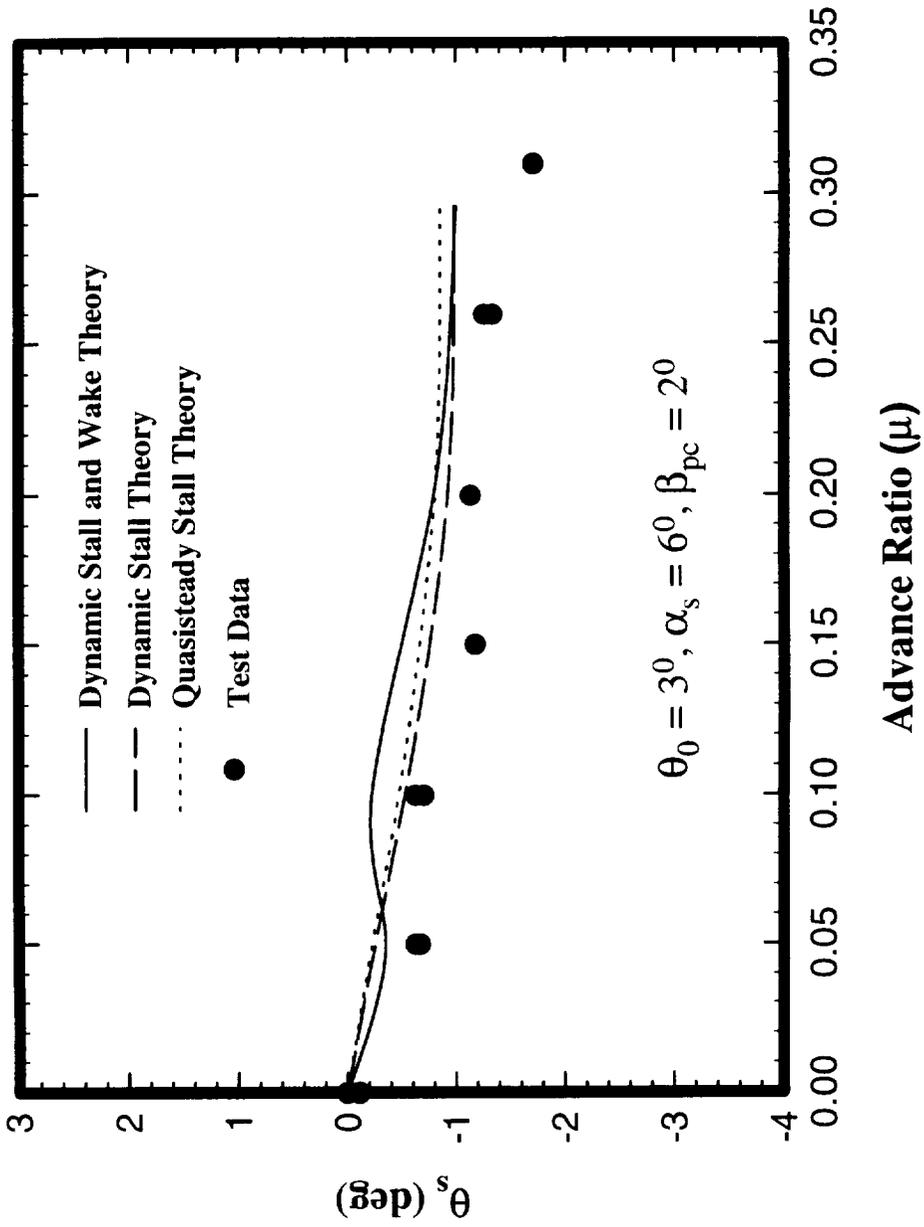
Figure 21: Effects of Aerodynamic Modeling on Longitudinal-Cyclic Pitch Correlation for $\theta_0 = 3^0$ and $\alpha_s = 6^0$
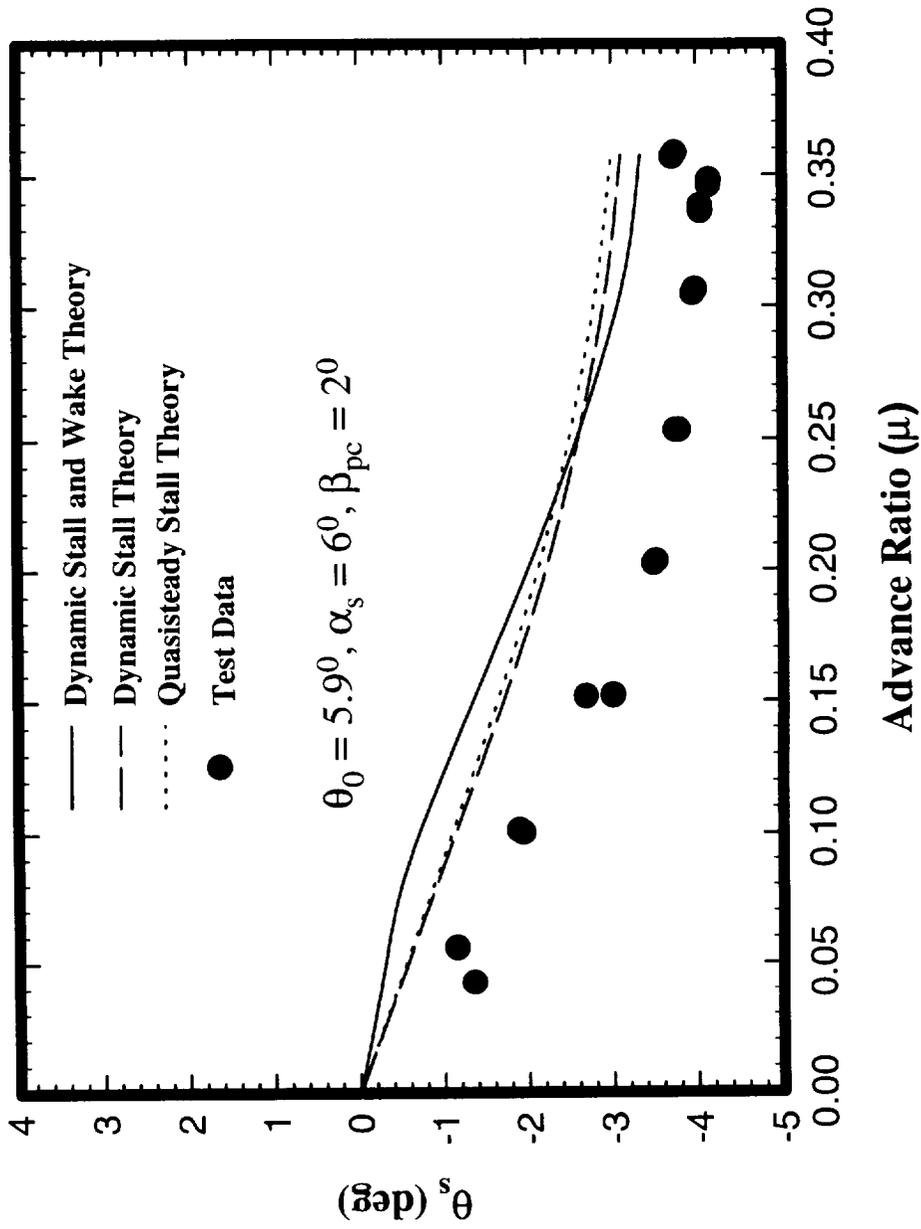
Figure 22: Effects of Aerodynamic Modeling on Longitudinal-Cyclic Pitch Correlation for $\theta_0 = 5.9^0$ and $\alpha_s = 6^0$

46
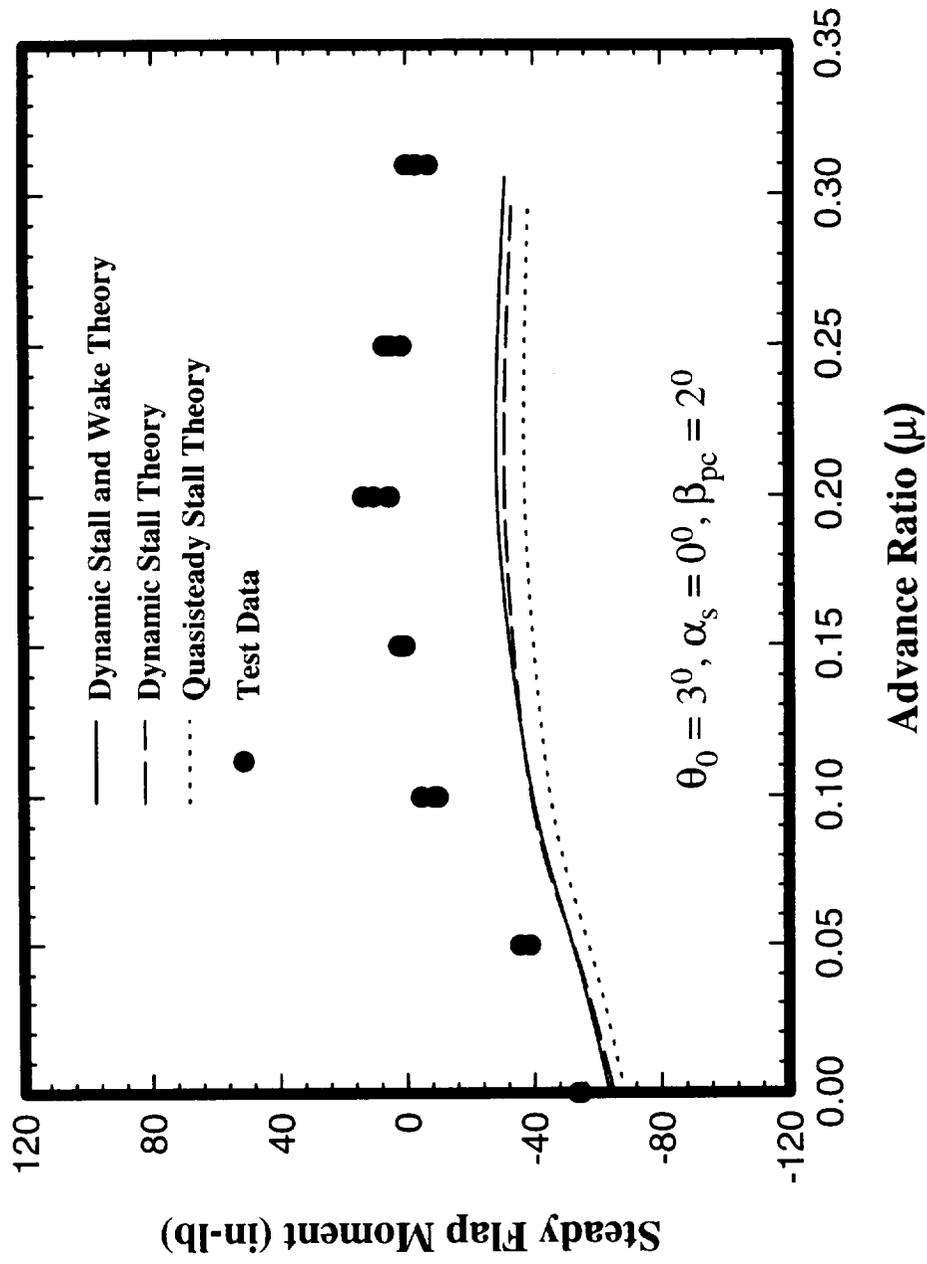
Figure 23: Effects of Aerodynamic Modeling on Flapping Moment Correlation from the Curvature Method for $\theta_0 = 3^0$ and $\alpha_s = 0^0$
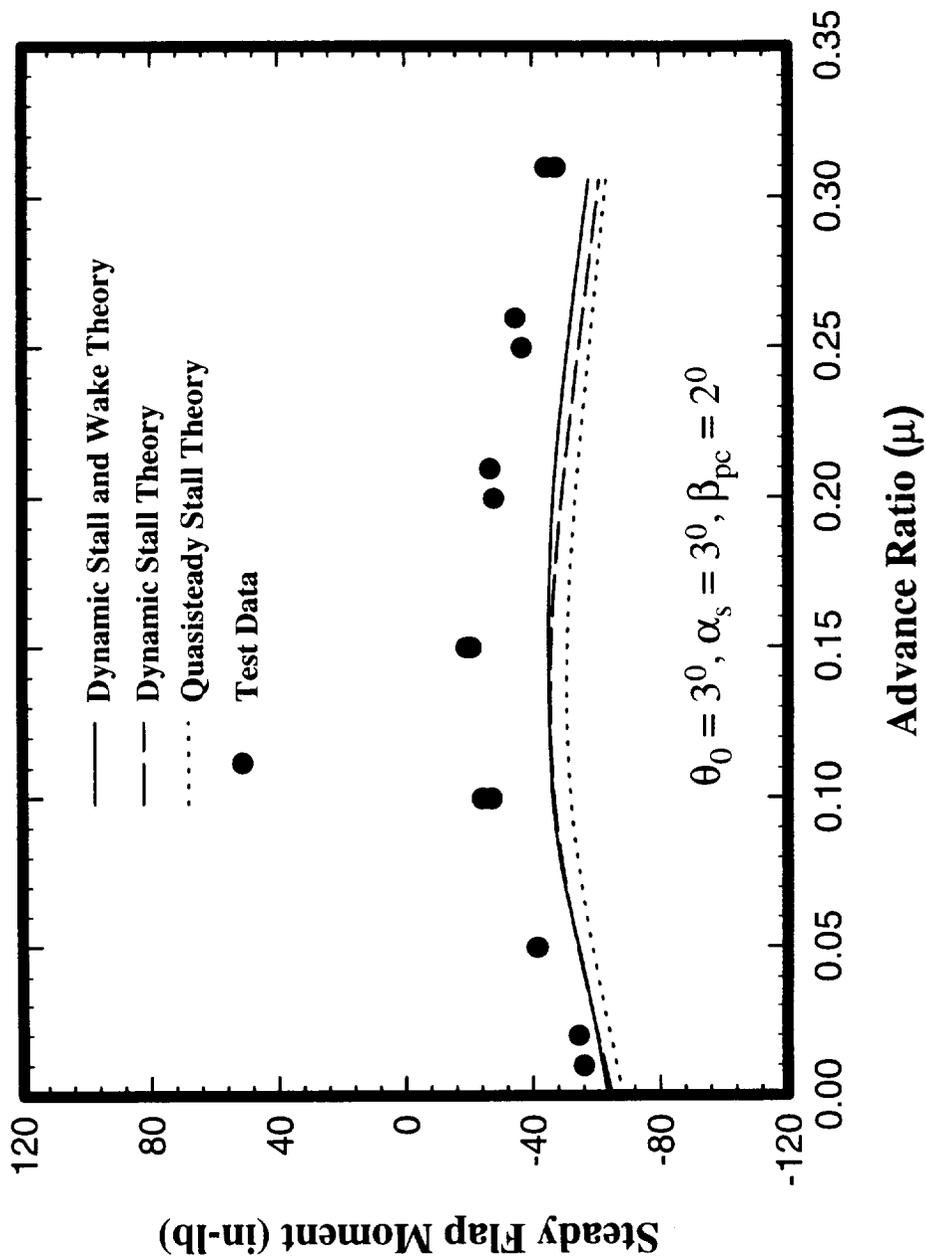
Figure 24: Effects of Aerodynamic Modeling on Flapping Moment Correlation from the Curvature Method for $\theta_0 = 3^0$ and $\alpha_s = 3^0$
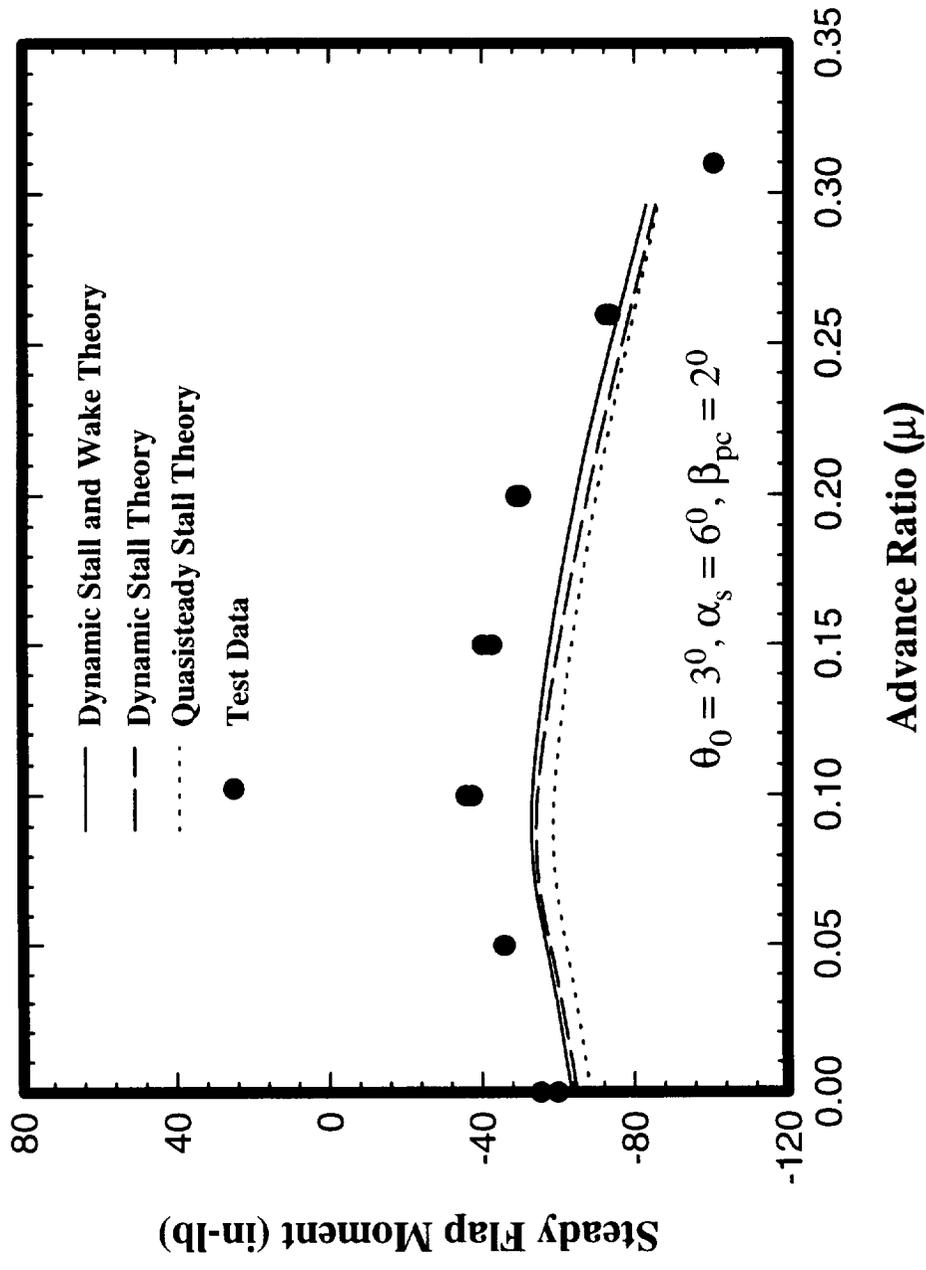
Figure 25: Effects of Aerodynamic Modeling on Flapping Moment Correlation from the Curvature Method for $\theta_0 = 3^0$ and $\alpha_s = 6^0$

49
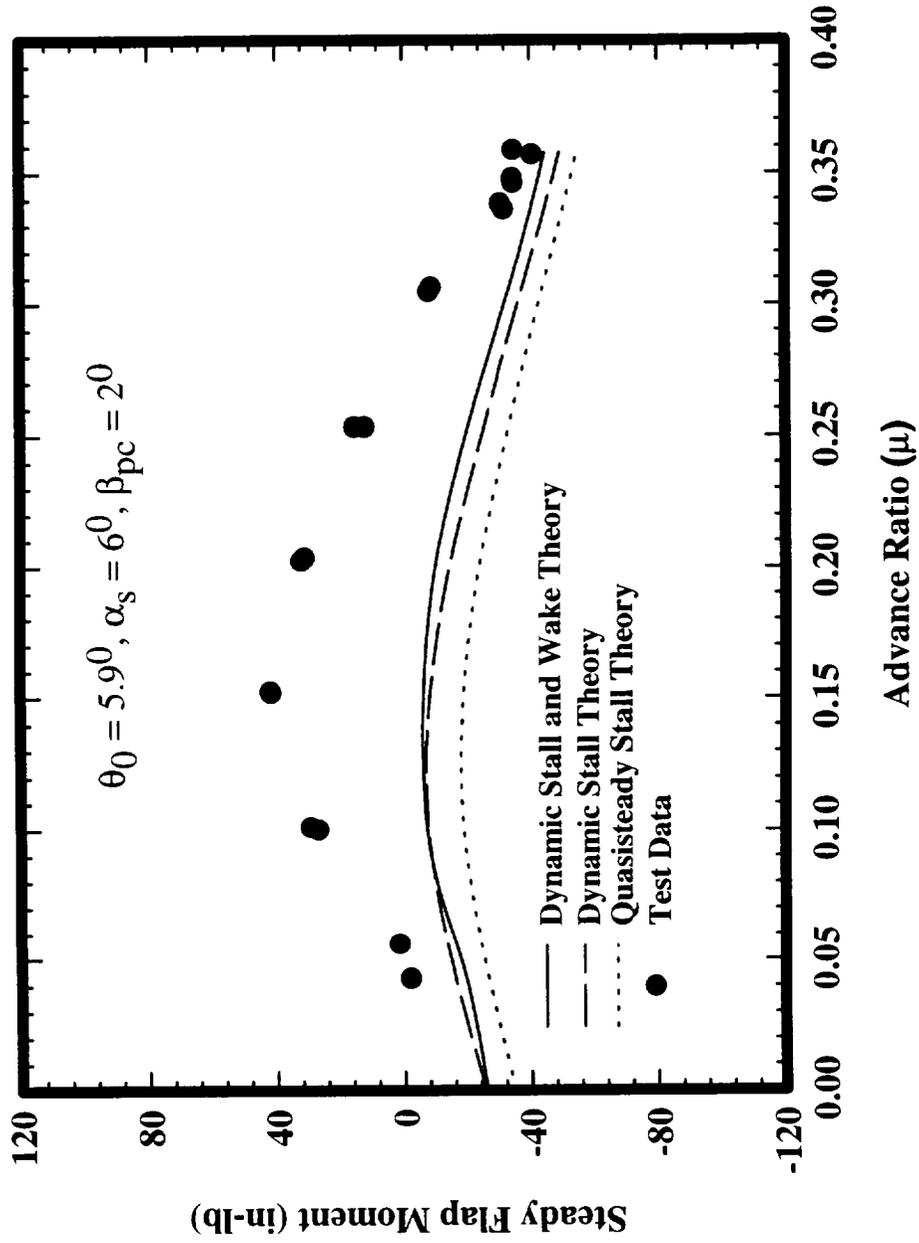
Figure 26: Effects of Aerodynamic Modeling on Flapping Moment Correlaion from the Curvature Method for $\theta_0 = 5.9^0$ and $\alpha_s = 6^0$

50
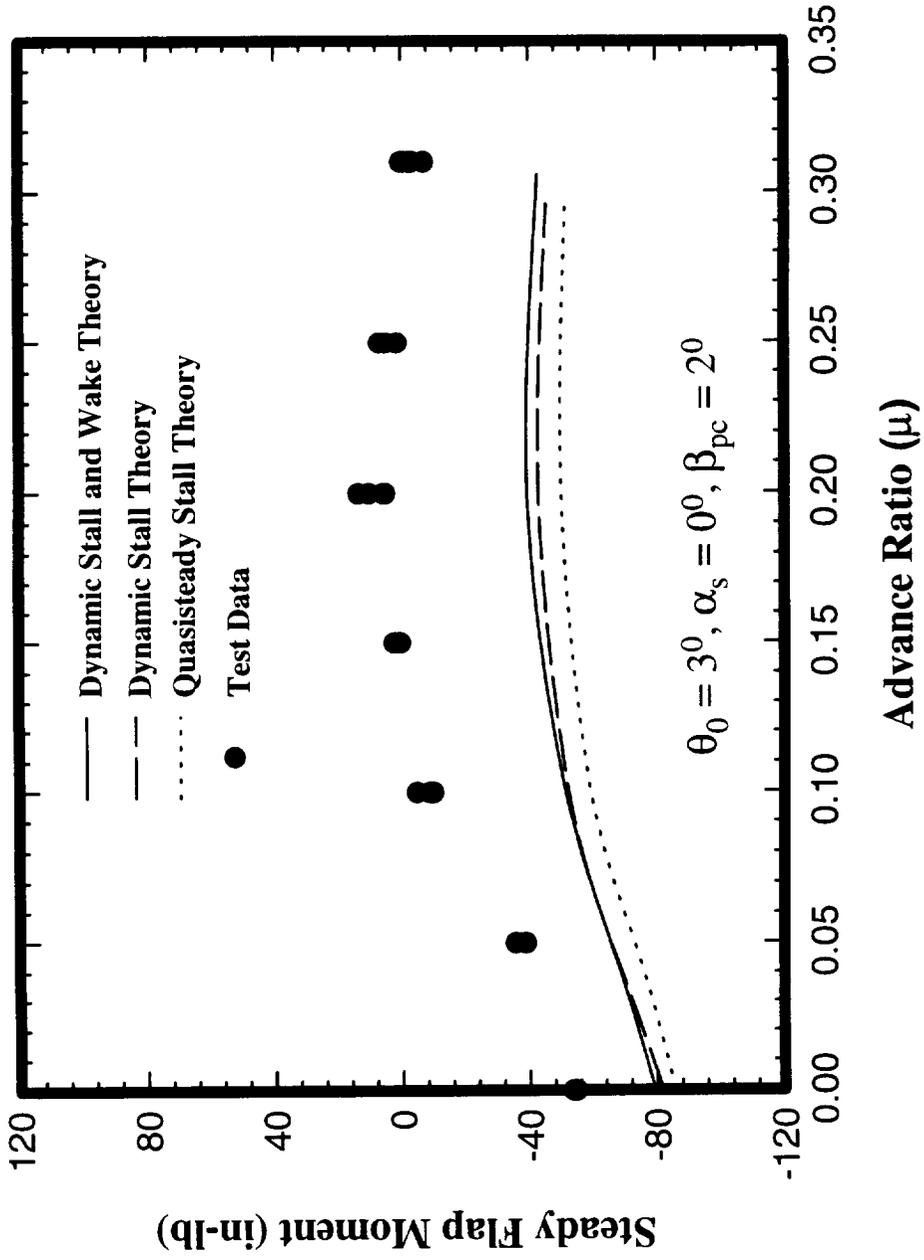
Figure 27: Effects of Aerodynamic Modeling on Flapping Moment Correlation from the Force-Integration Method for $\theta_0 = 3^0$ and $\alpha_s = 0^0$
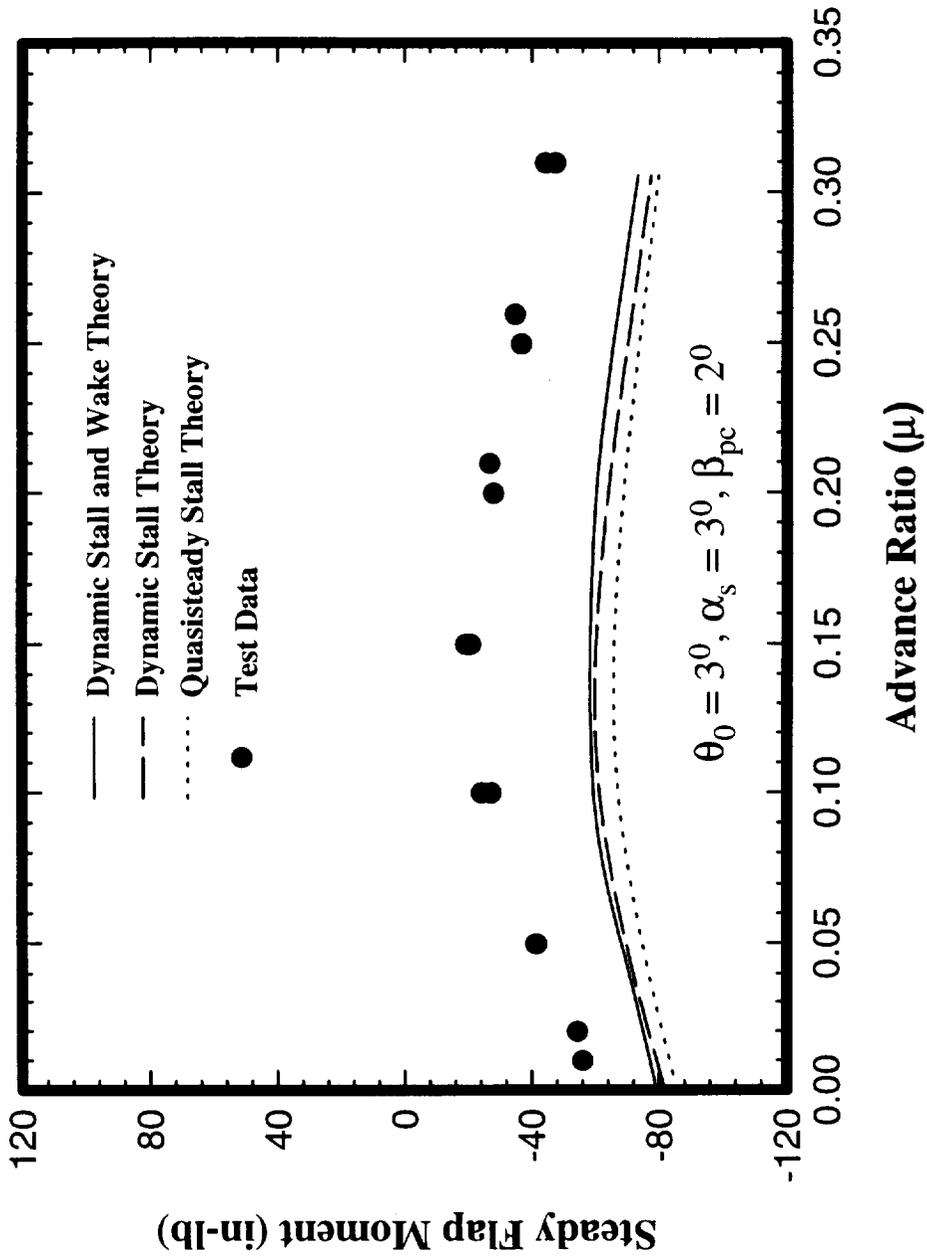
Figure 28: Effects of Aerodynamic Modeling on Flapping Moment Correlation from the Force-Integration Method for $\theta_0 = 3^0$ and $\alpha_s = 3^0$

52
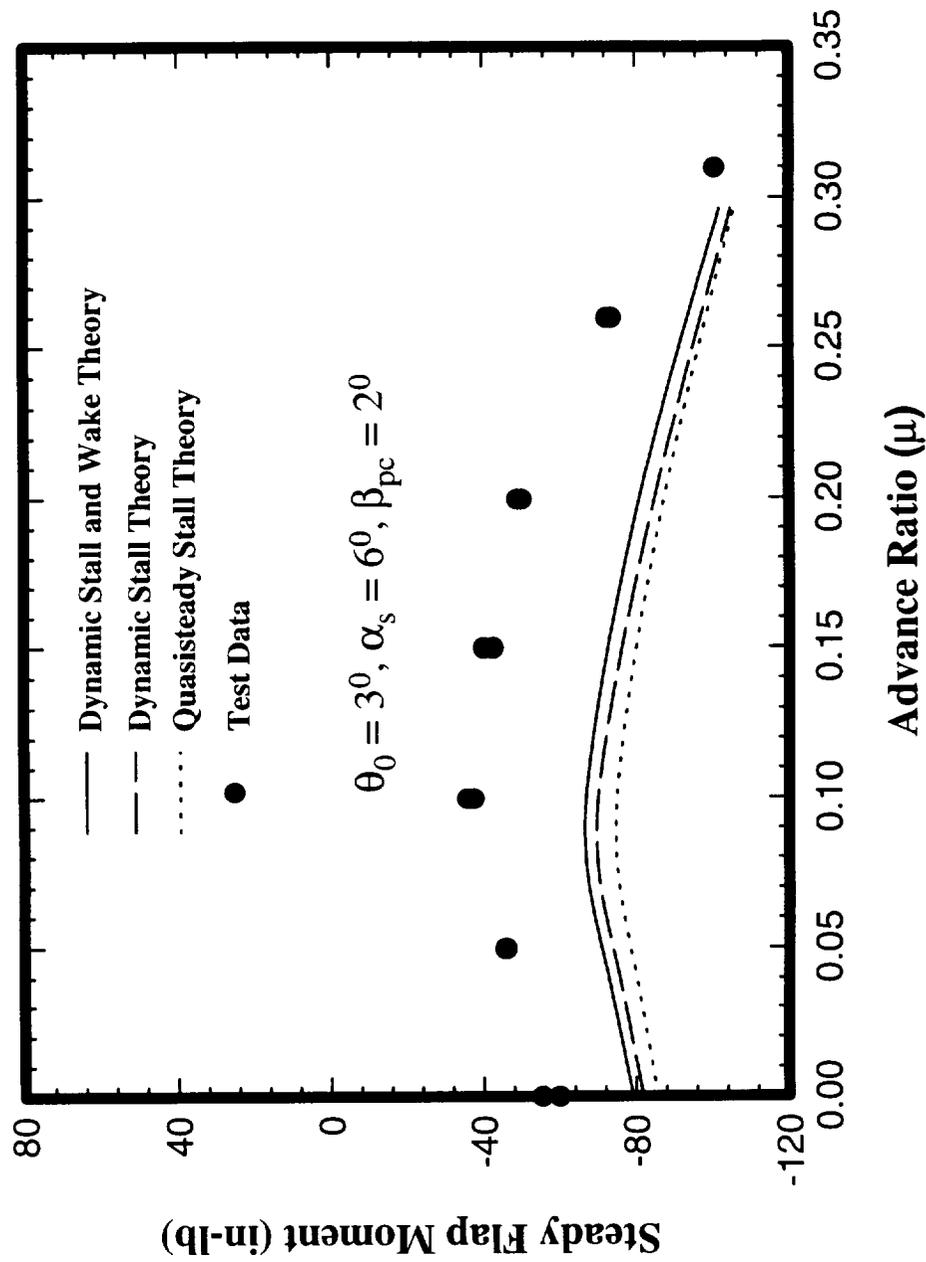
Figure 29: Effects of Aerodynamic Modeling on Flapping Moment Correlation from the Force-Integration Method for $\theta_0 = 3^0$ and $\alpha_s = 6^0$

53
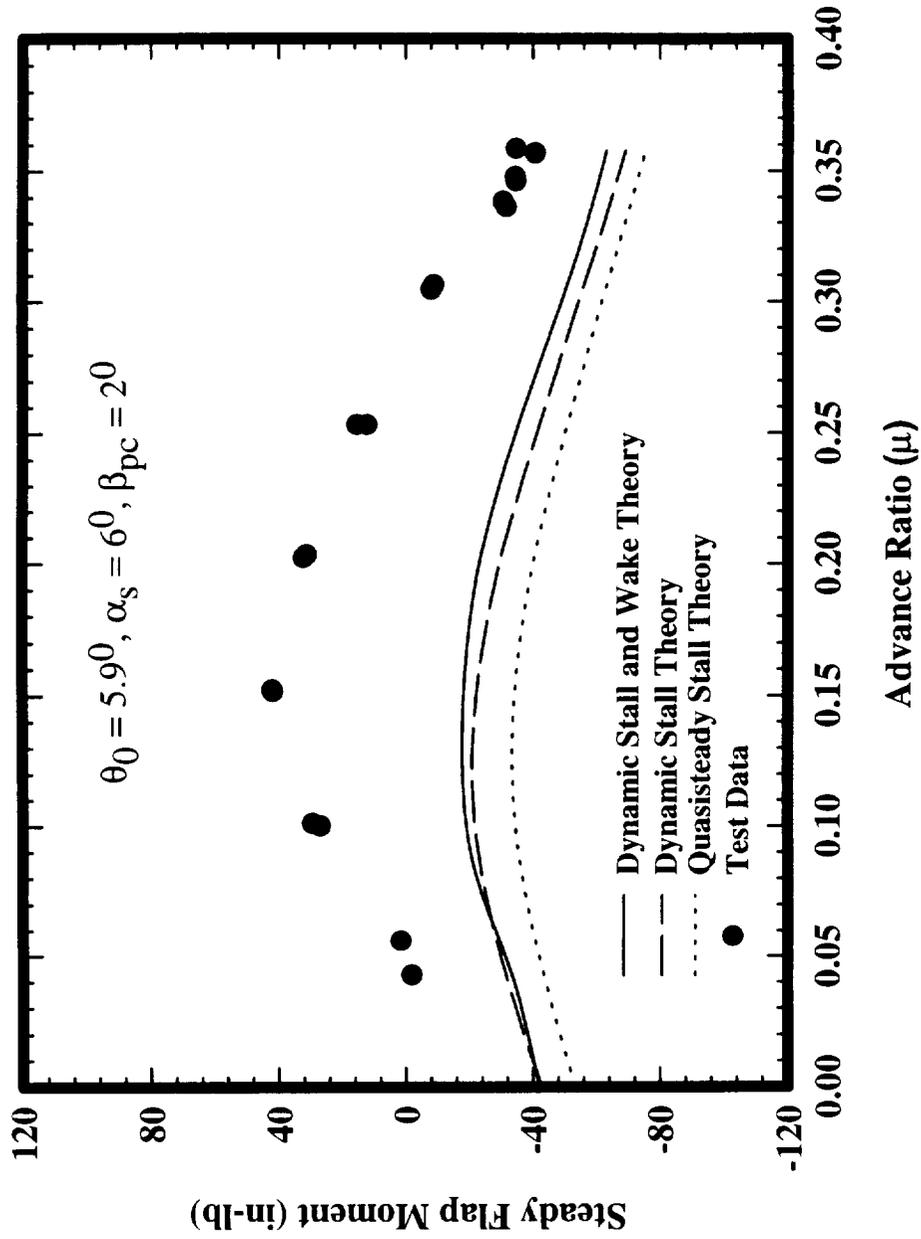
Figure 30: Effects of Aerodynamic Modeling on Flapping Moment Correlation from the Force-Integration Method for $\theta_0 = 5.9^0$ and $\alpha_s = 6^0$
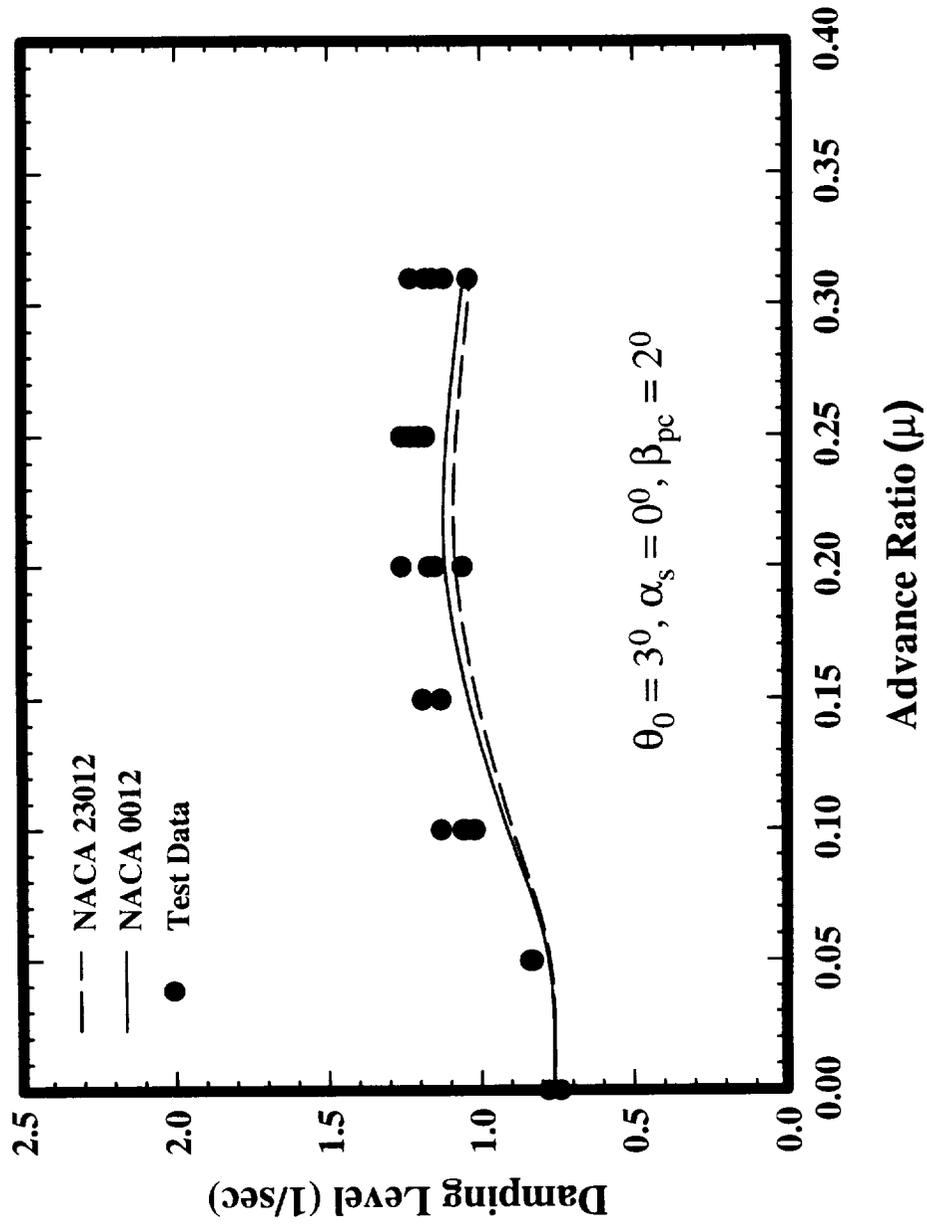
Figure 31: Effects of Dynamic Stall Parameters on Lag Damping from the Dynamic Stall and Wake Theory for $\theta_0 = 3^0$ and $\alpha_s = 0^0$
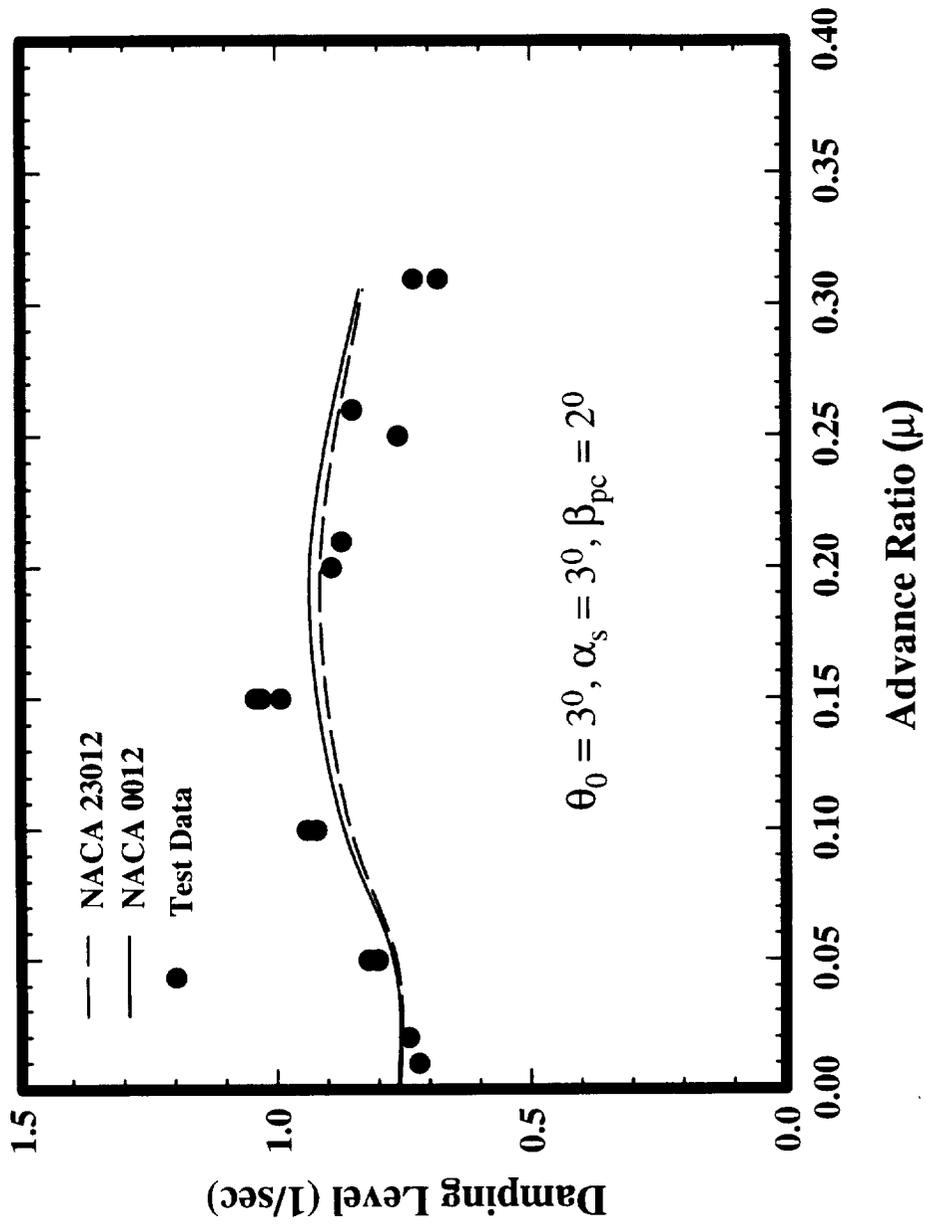
Figure 32: Effects of Dynamic Stall Parameters on Lag Damping from the Dynamic Stall and Wake Theory for $\theta_0 = 3^0$ and $\alpha_s = 3^0$
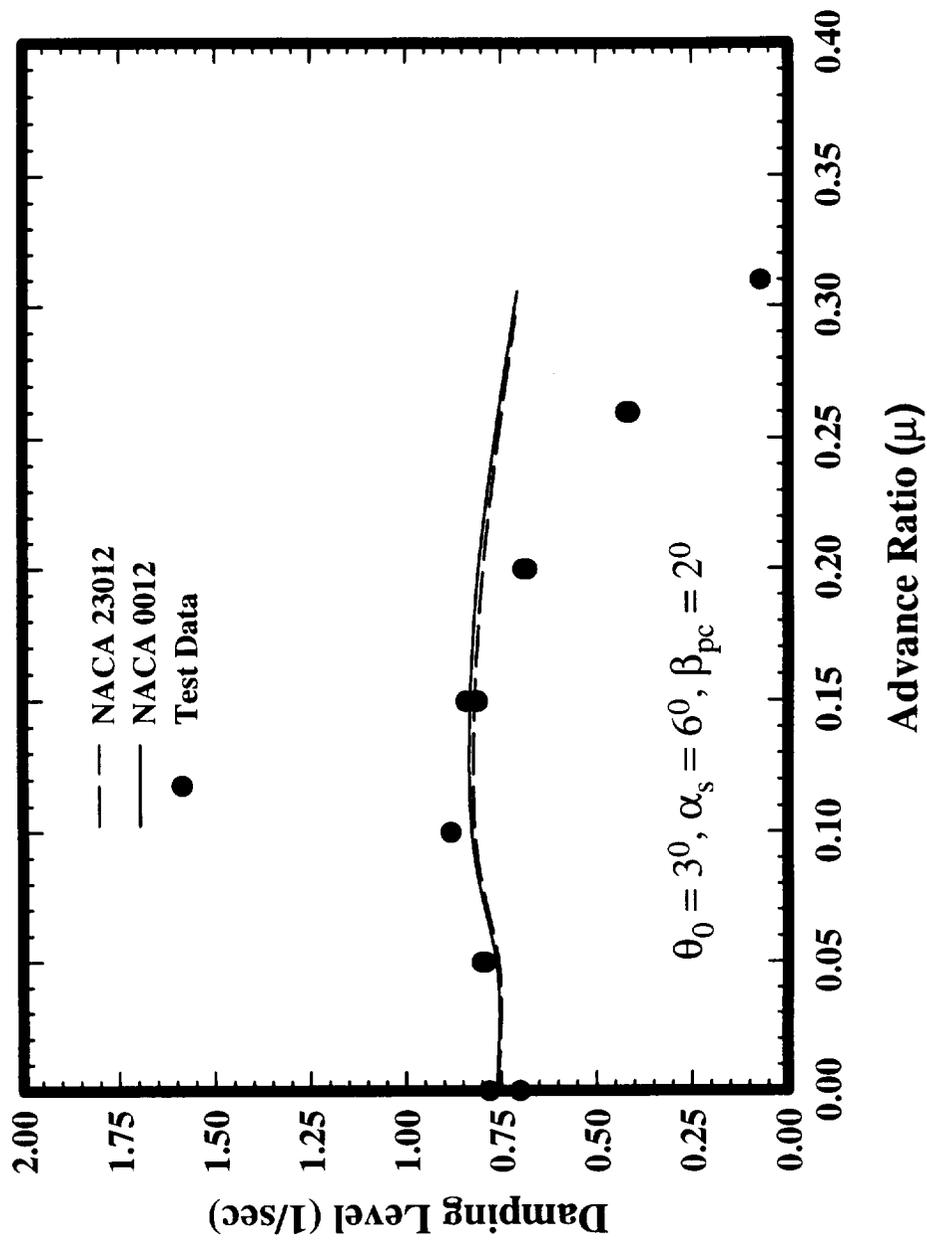
Figure 33: Effects of Dynamic Stall Parameters on Lag Damping from the Dynamic Stall and Wake Theory for $\theta_0 = 3^0$ and $\alpha_s = 6^0$
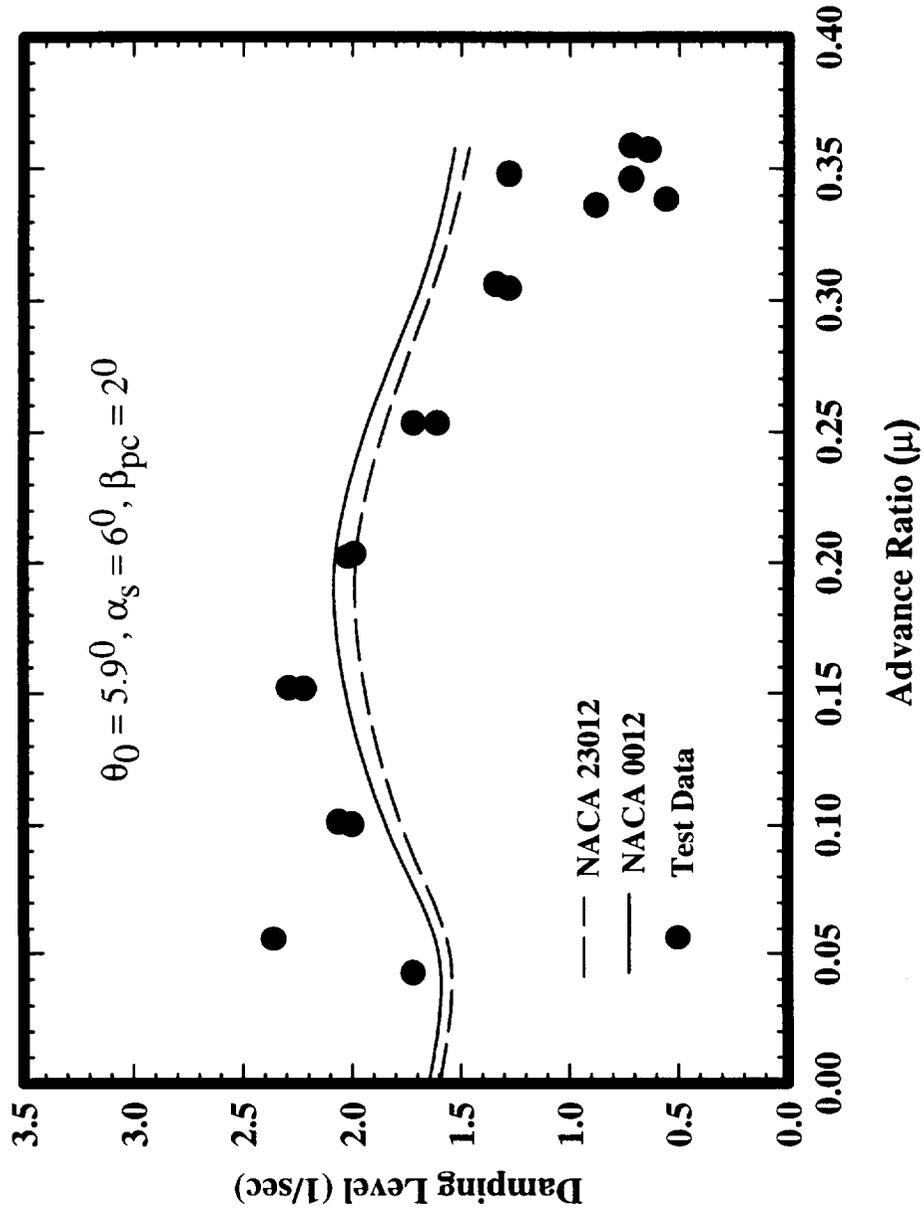
Figure 34: Effects of Dynamic Stall Parameters on Lag Damping from the Dynamic Stall and Wake Theory for $\theta_0 = 5.9^0$ and $\alpha_s = 6^0$
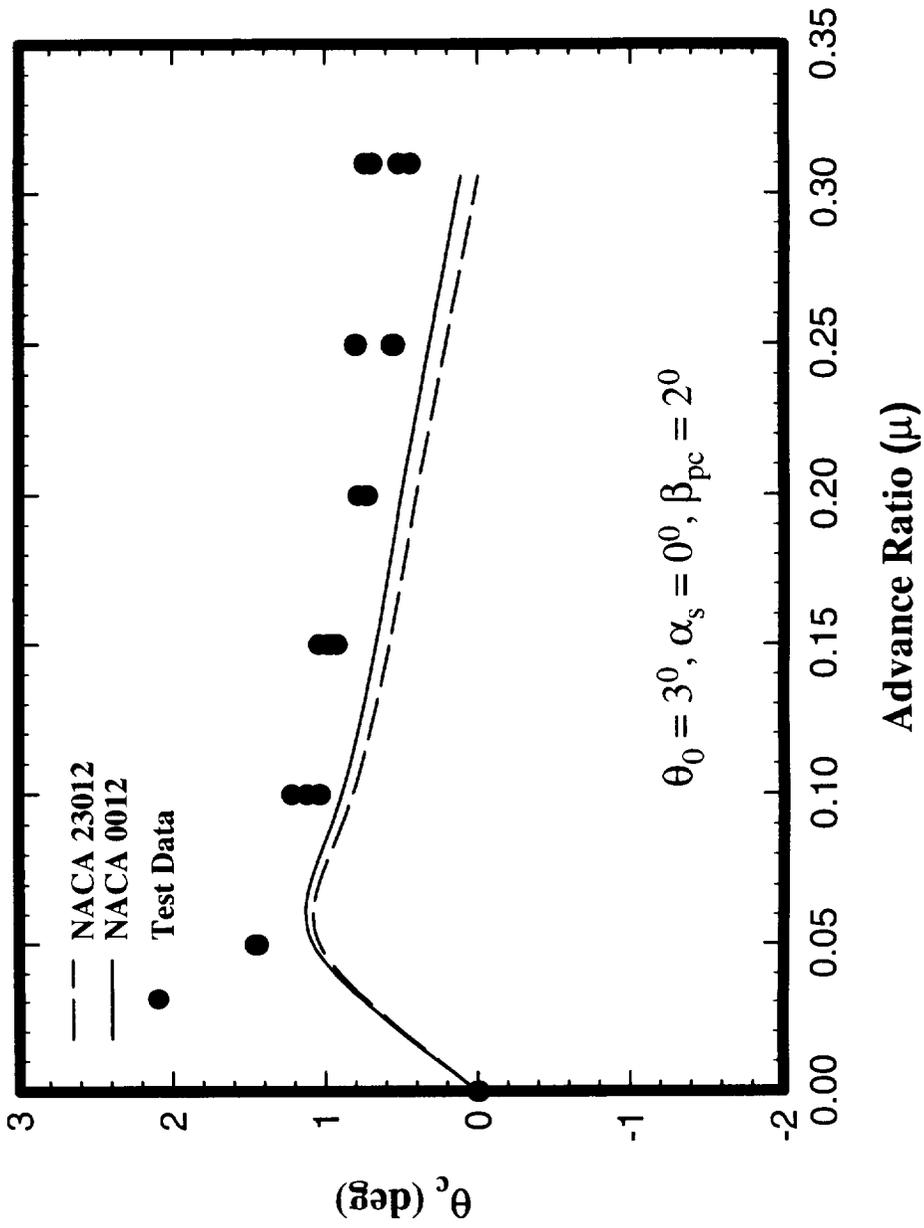
Figure 35: Effects of Dynamic Stall Parameters on Lateral-Cyclic Pitch Angle from the Dynamic Stall and Wake Theory for $\theta_0 = 3^0$ and $\alpha_s = 0^0$
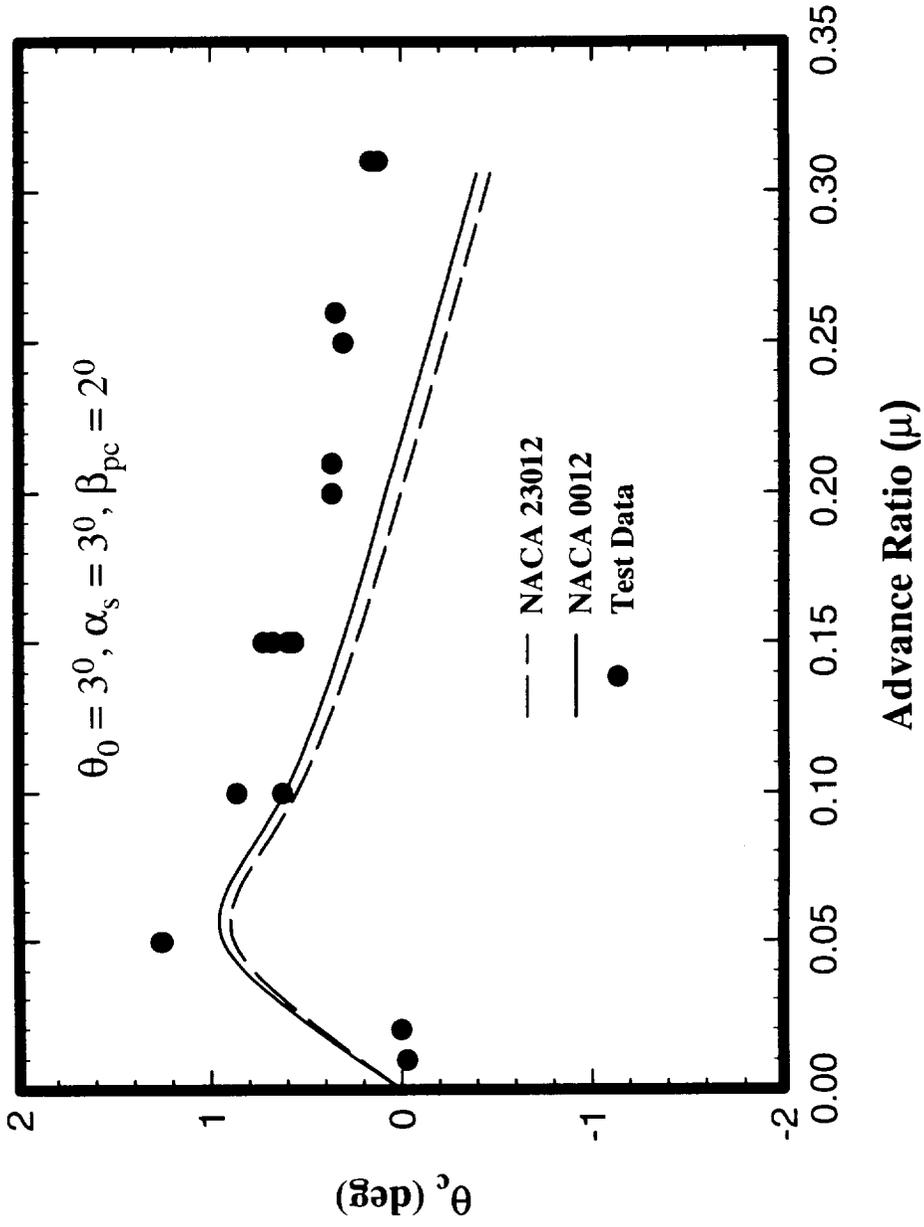
Figure 36: Effects of Dynamic Stall Parameters on Lateral-Cyclic Pitch Angle from the Dynamic Stall and Wake Theory for $\theta_0 = 3^0$ and $\alpha_s = 3^0$
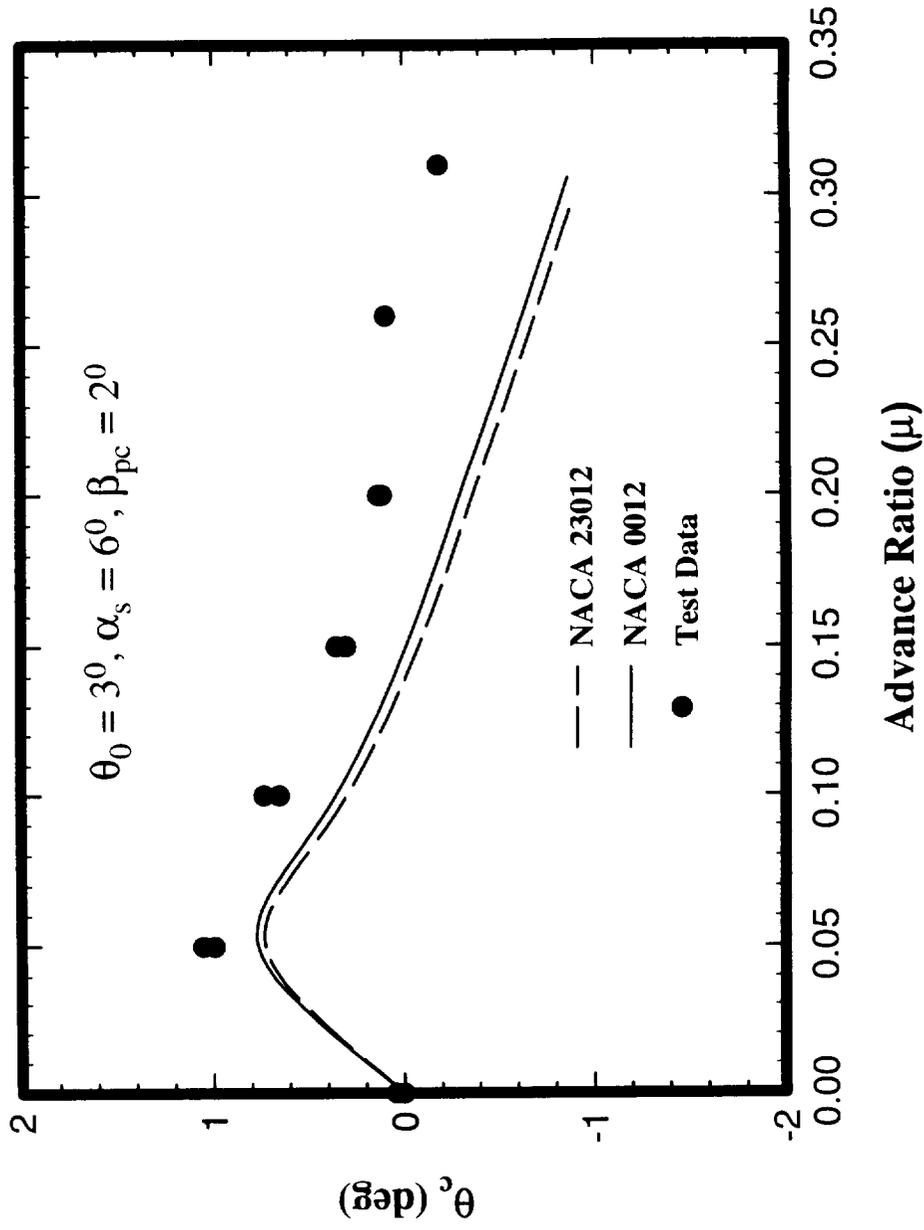
Figure 37: Effects of Dynamic Stall Parameters on Lateral-Cyclic Pitch Angle from the Dynamic Stall and Wake Theory for $\theta_0 = 3^0$ and $\alpha_s = 6^0$
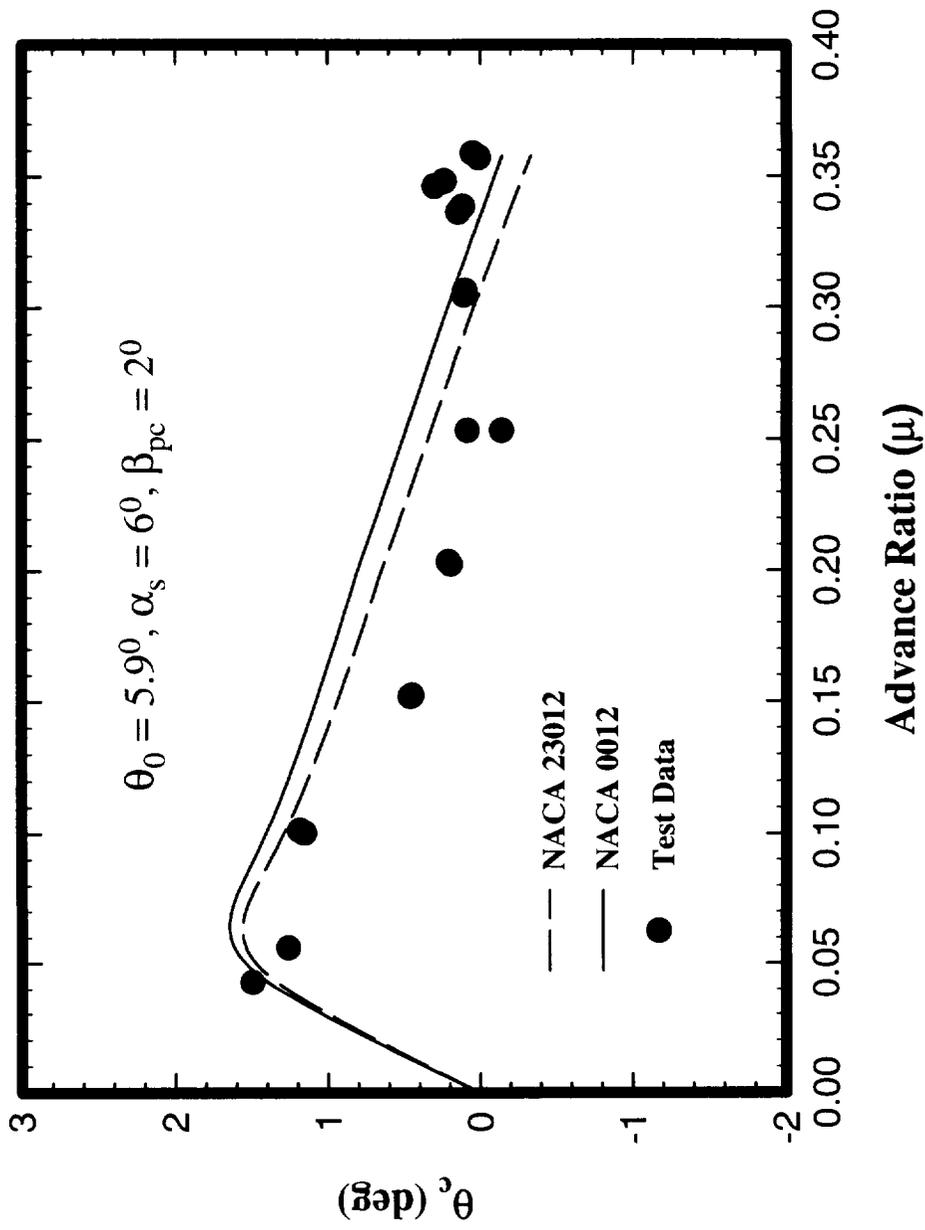
Figure 38: Effects of Dynamic Stall Parameters on Lateral-Cyclic Pitch Angle from the Dynamic Stall and Wake Theory for $\theta_0 = 5.9^0$ and $\alpha_s = 6^0$
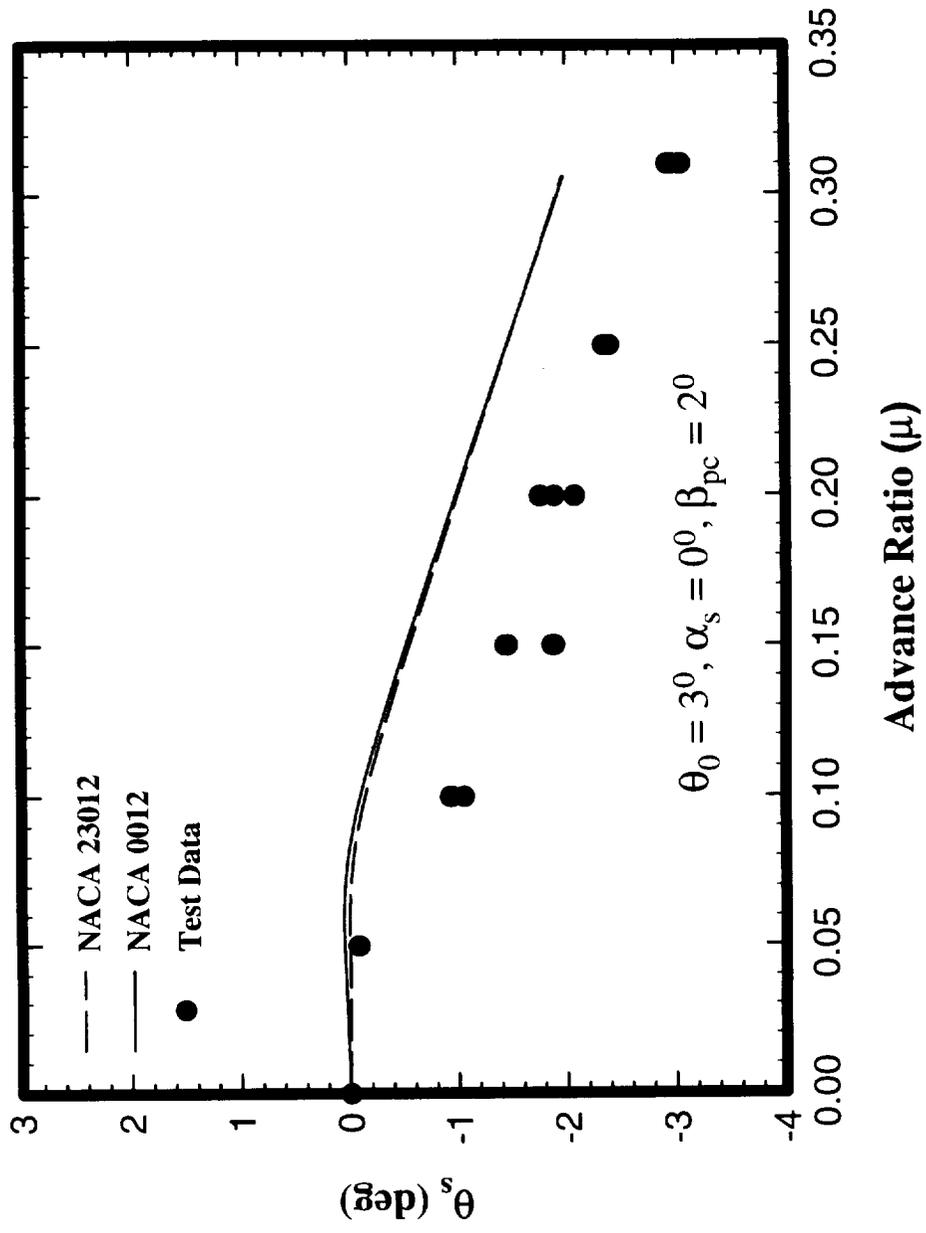
Figure 39: Effects of Dynamic Stall Parameters on Longitudinal-Cyclic Pitch Angle from the Dynamic Stall and Wake Theory for $\theta_0 = 3^0$ and $\alpha_s = 0^0$
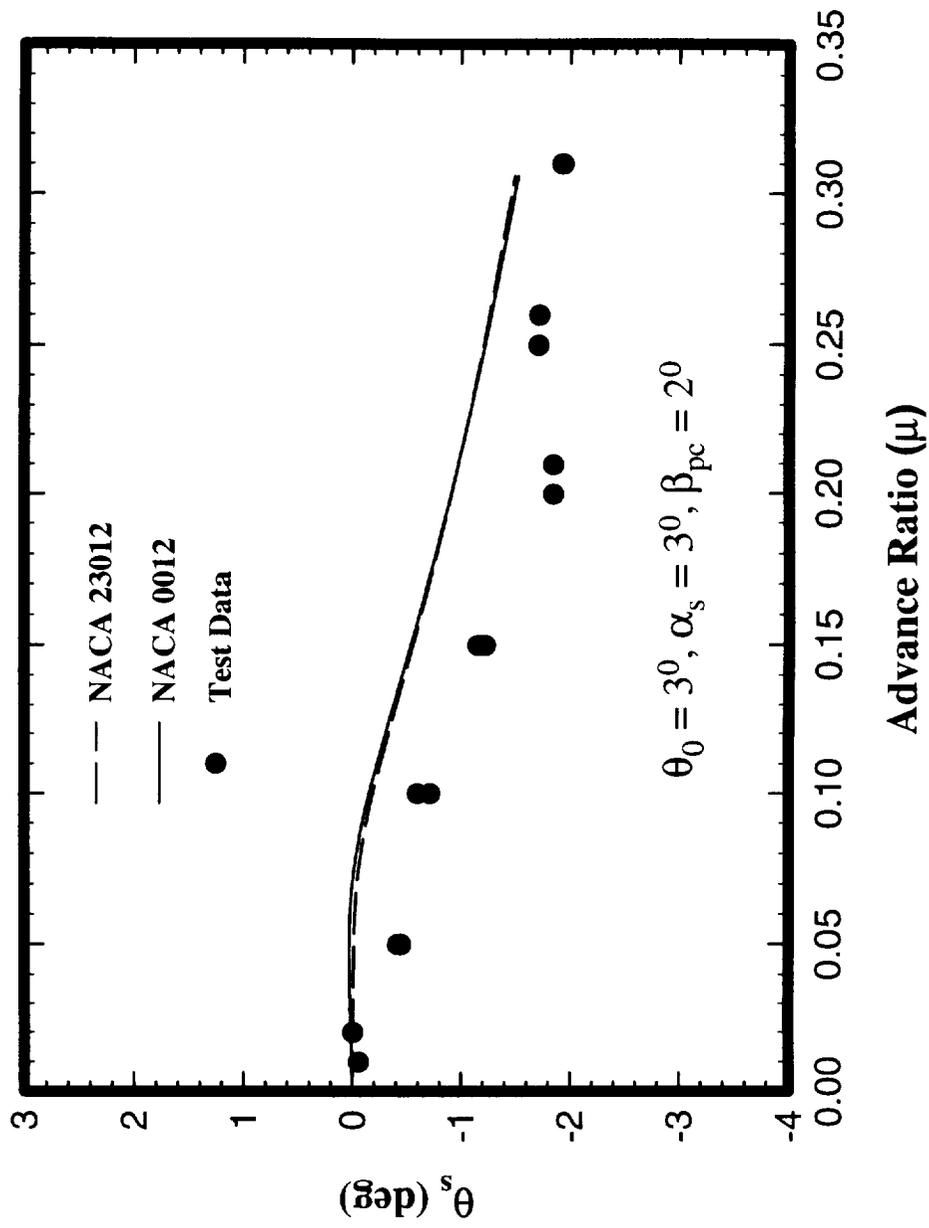
Figure 40: Effects of Dynamic Stall Parameters on Longitudinal-Cyclic Pitch Angle from the Dynamic Stall and Wake Theory for $\theta_0 = 3^0$ and $\alpha_s = 3^0$
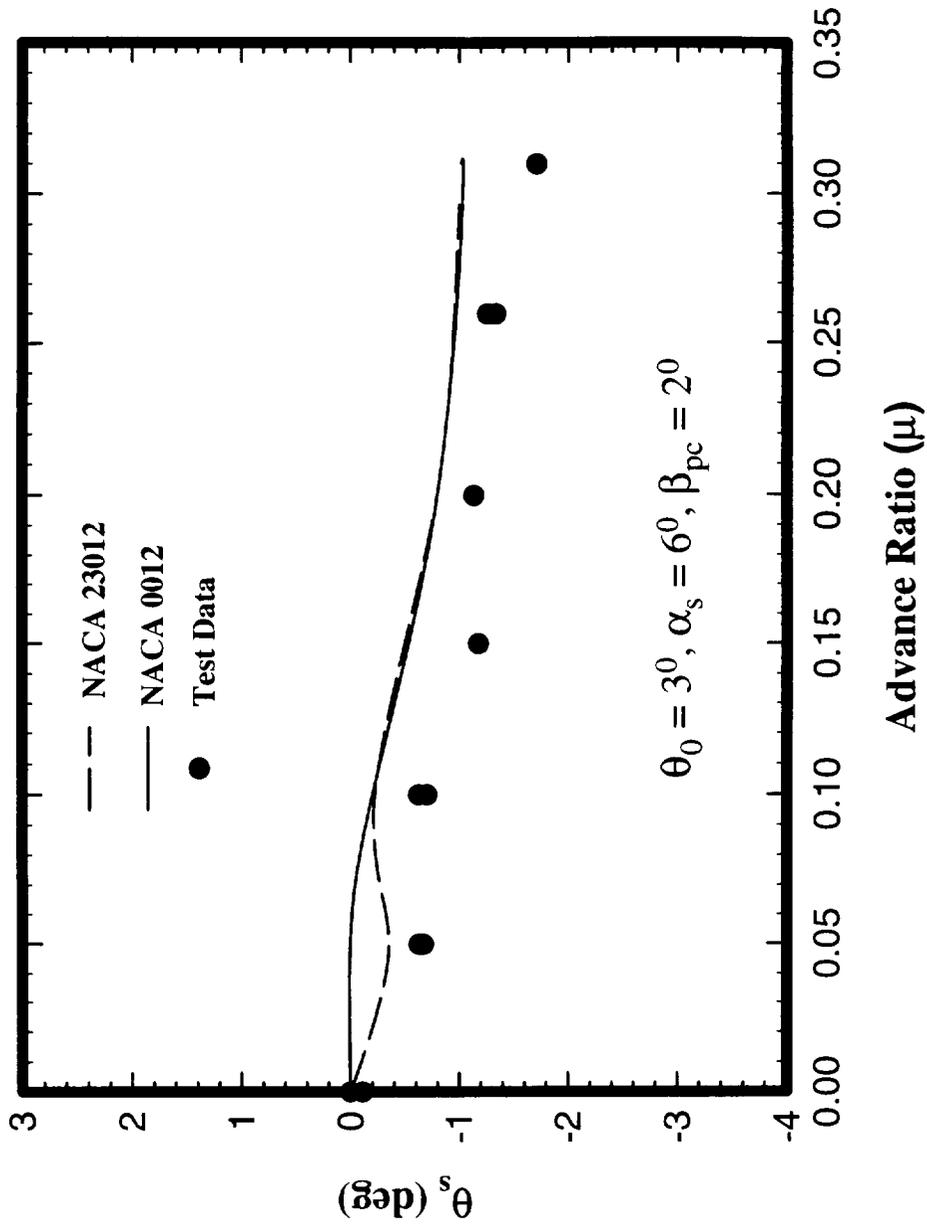
Figure 41: Effects of Dynamic Stall Parameters on Longitudinal-Cyclic Pitch Angle from the Dynamic Stall and Wake Theroy for $\theta_0 = 3^0$ and $\alpha_s = 6^0$

65
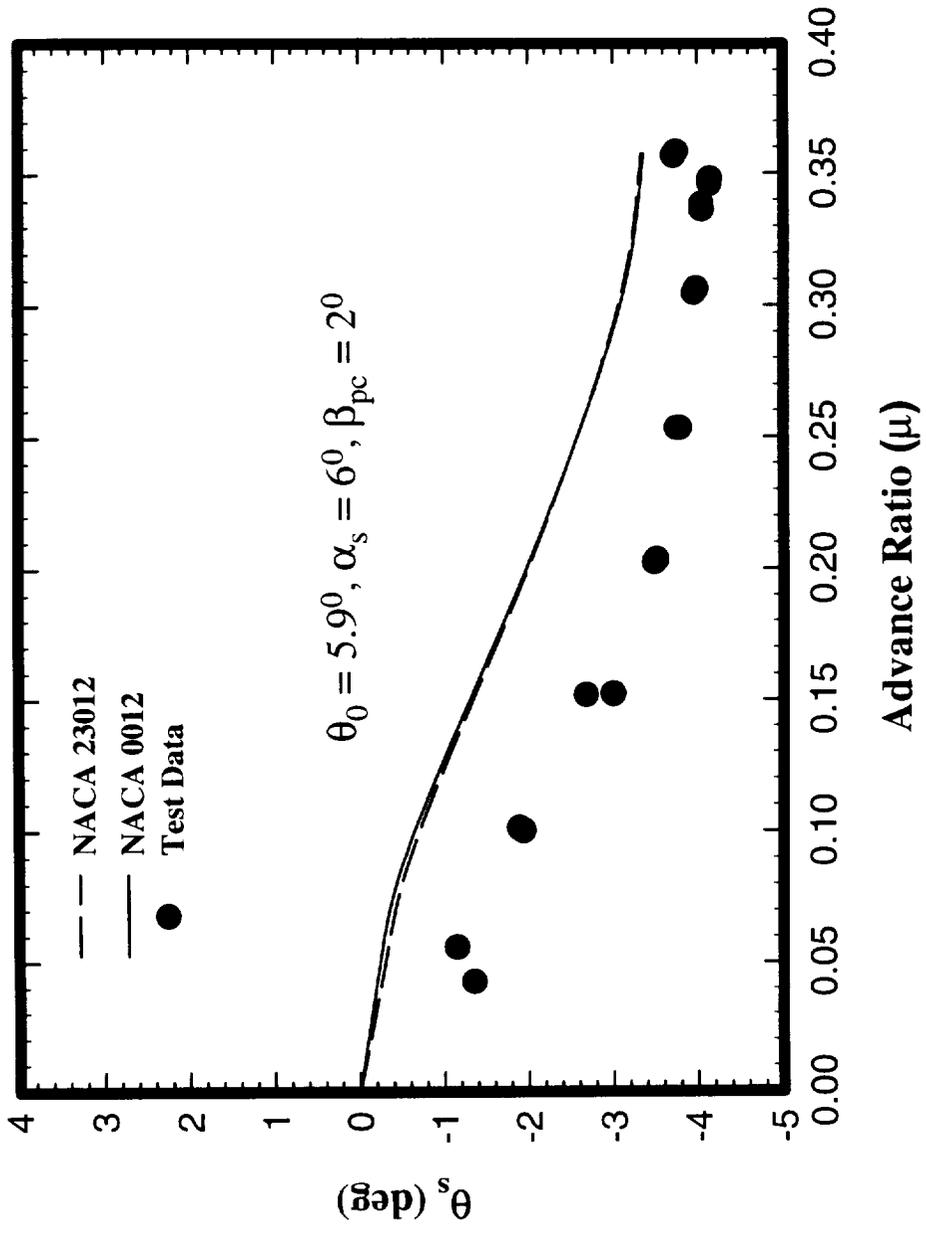
Figure 42: Effects of Dynamic Stall Parameters on Longitudinal-Cyclic Pitch Angle from the Dynamic Stall and Wake Theory for $\theta_0 = 5.9^0$ and $\alpha_s = 6^0$
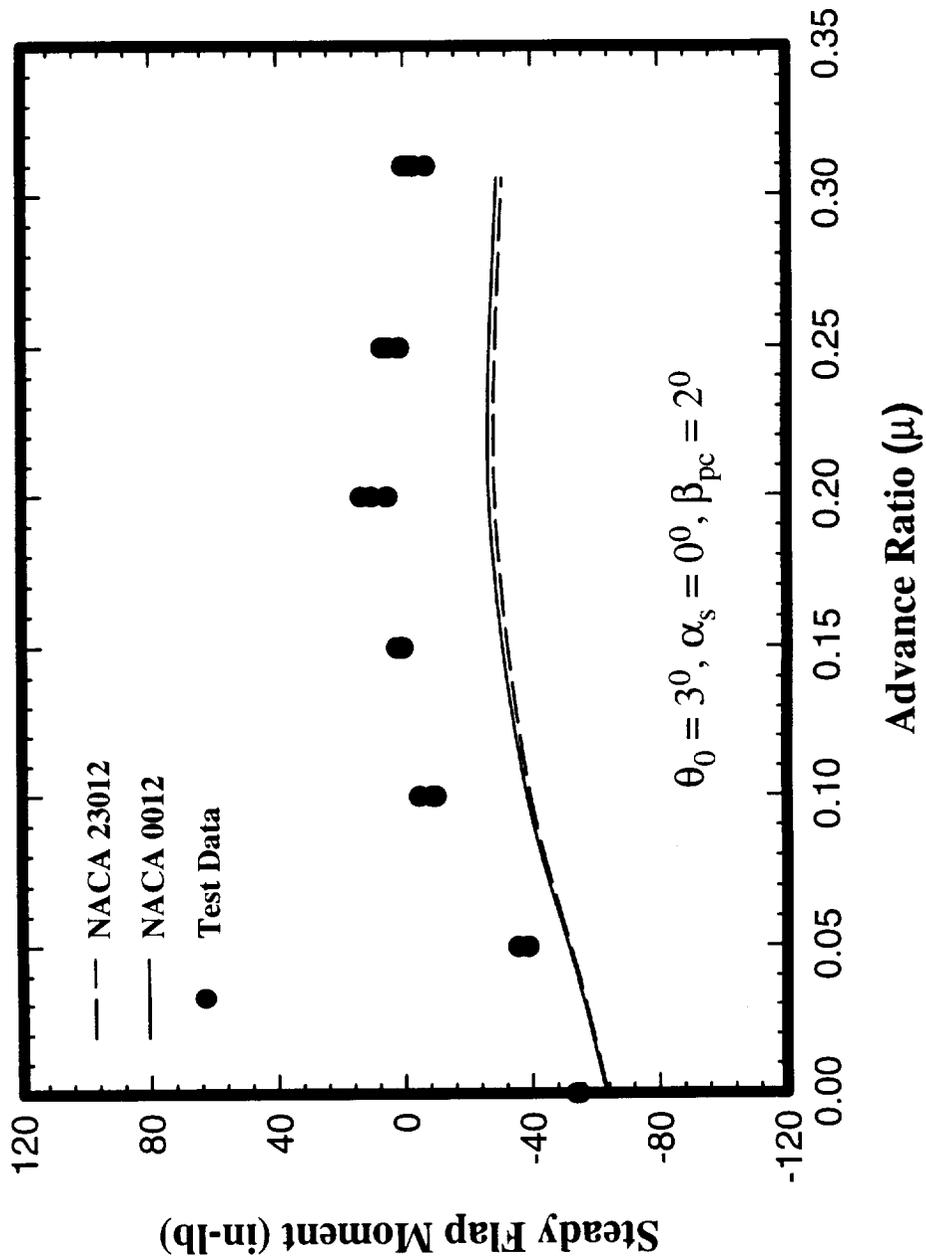
Figure 43: Effects of Dynamic Stall Parameters on Flapping Moment Based on the Curvature Method from the Dynamic Stall and Wake Theory for $\theta_0 = 3^0$ and $\alpha_s = 0^0$
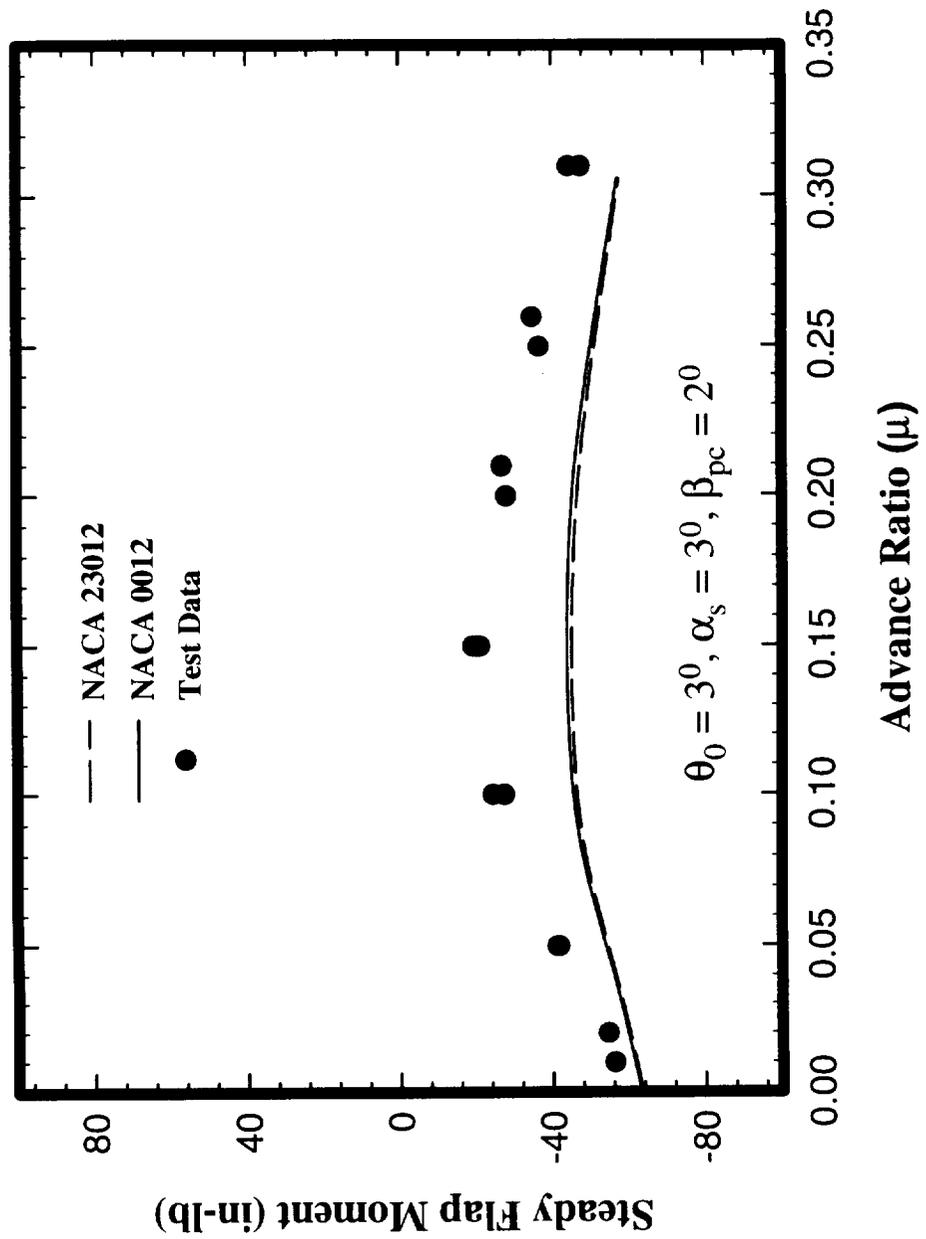
Figure 44: Effects of Dynamic Stall Parameters on Flapping Moment Based on the Curvature Method from the Dynamic Stall and Wake Theory for $\theta_0 = 3^0$ and $\alpha_s = 3^0$

68
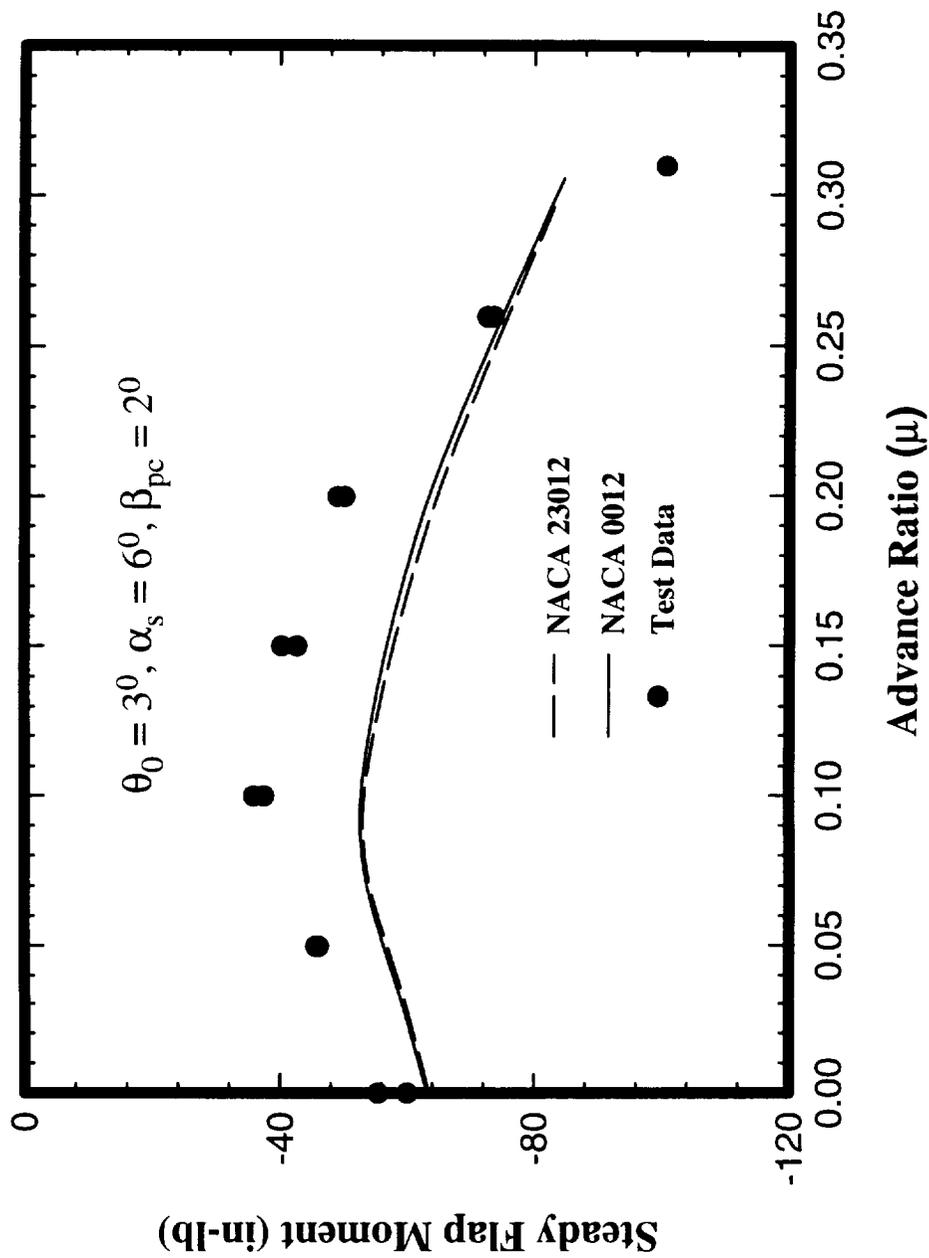
Figure 45: Effects of Dynamic Stall Parameters on Flapping Moment Based on the Curvature Method from the Dynamic Stall and Wake Theory for $\theta_0 = 3^0$ and $\alpha_s = 6^0$
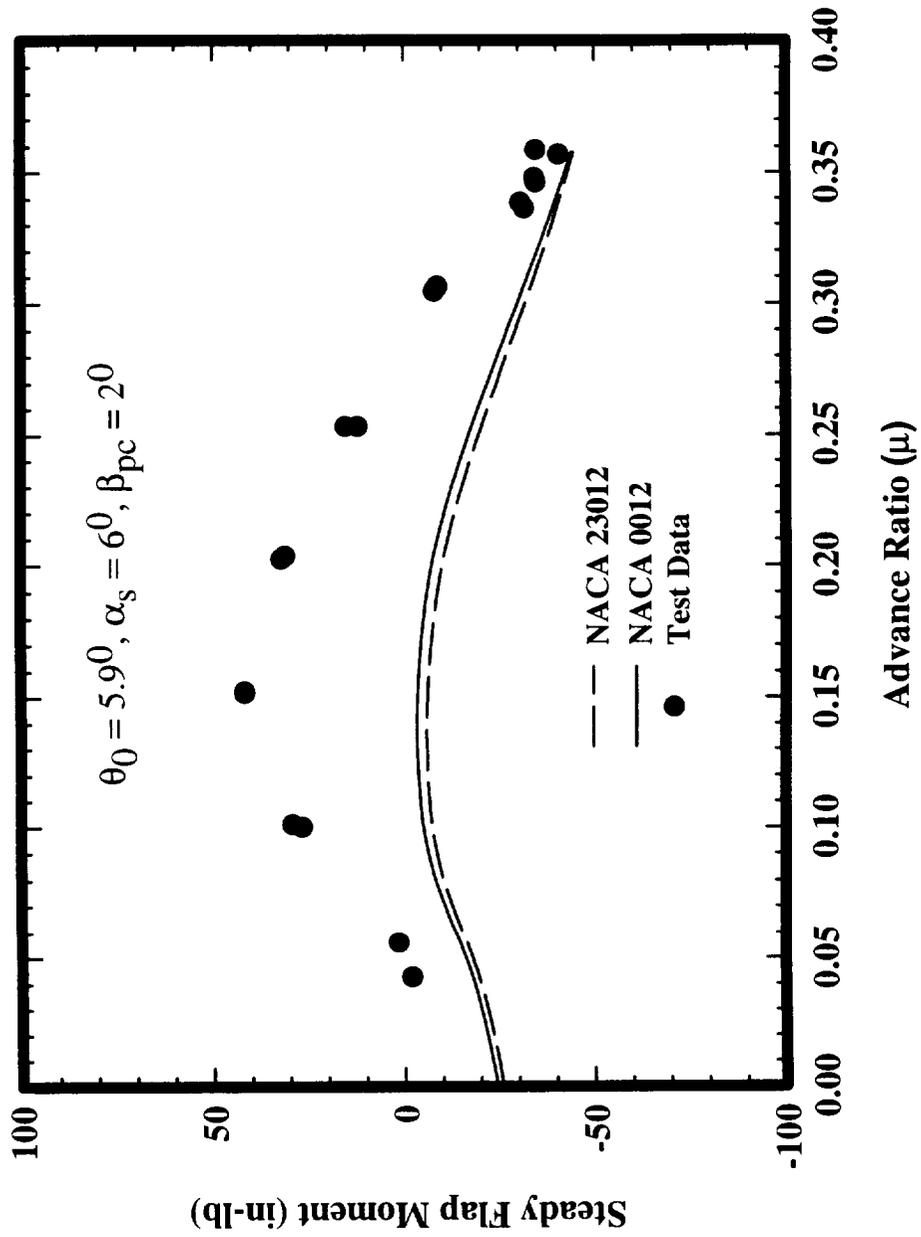
Figure 46: Effects of Dynamic Stall Parameters on Flapping Moment Based on the Curvature Method from the Dynamic Stall and Wake Theory for $\theta_0 = 5.9^0$ and $\alpha_s = 6^0$
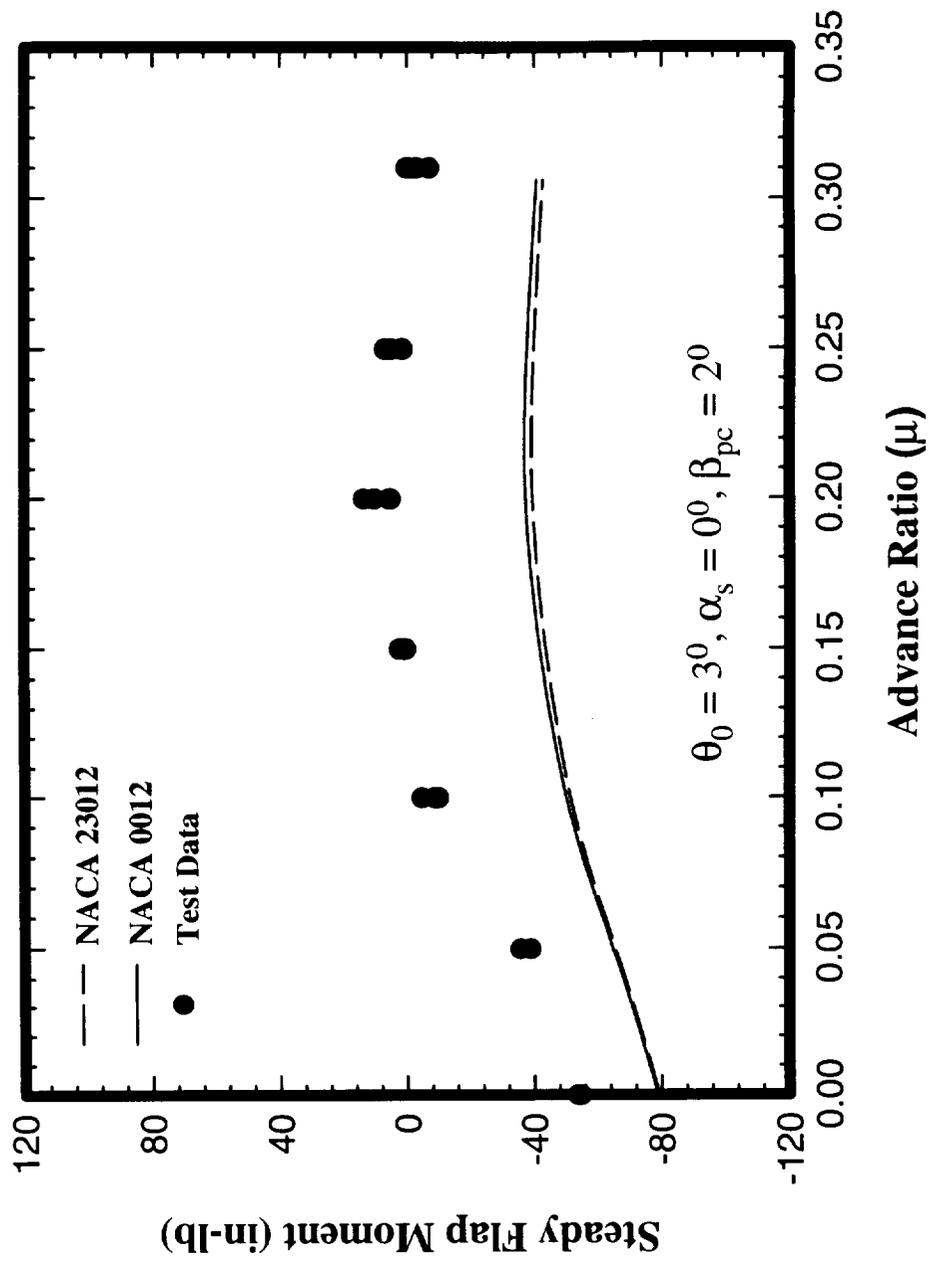
Figure 47: Effects of Dynamic Stall Parameters on Flapping Moment Based on the
Force-Integration Method from the Dynamic Stall and Wake Theory for $\theta_0 = 3^0$ and $\alpha_s = 0^0$
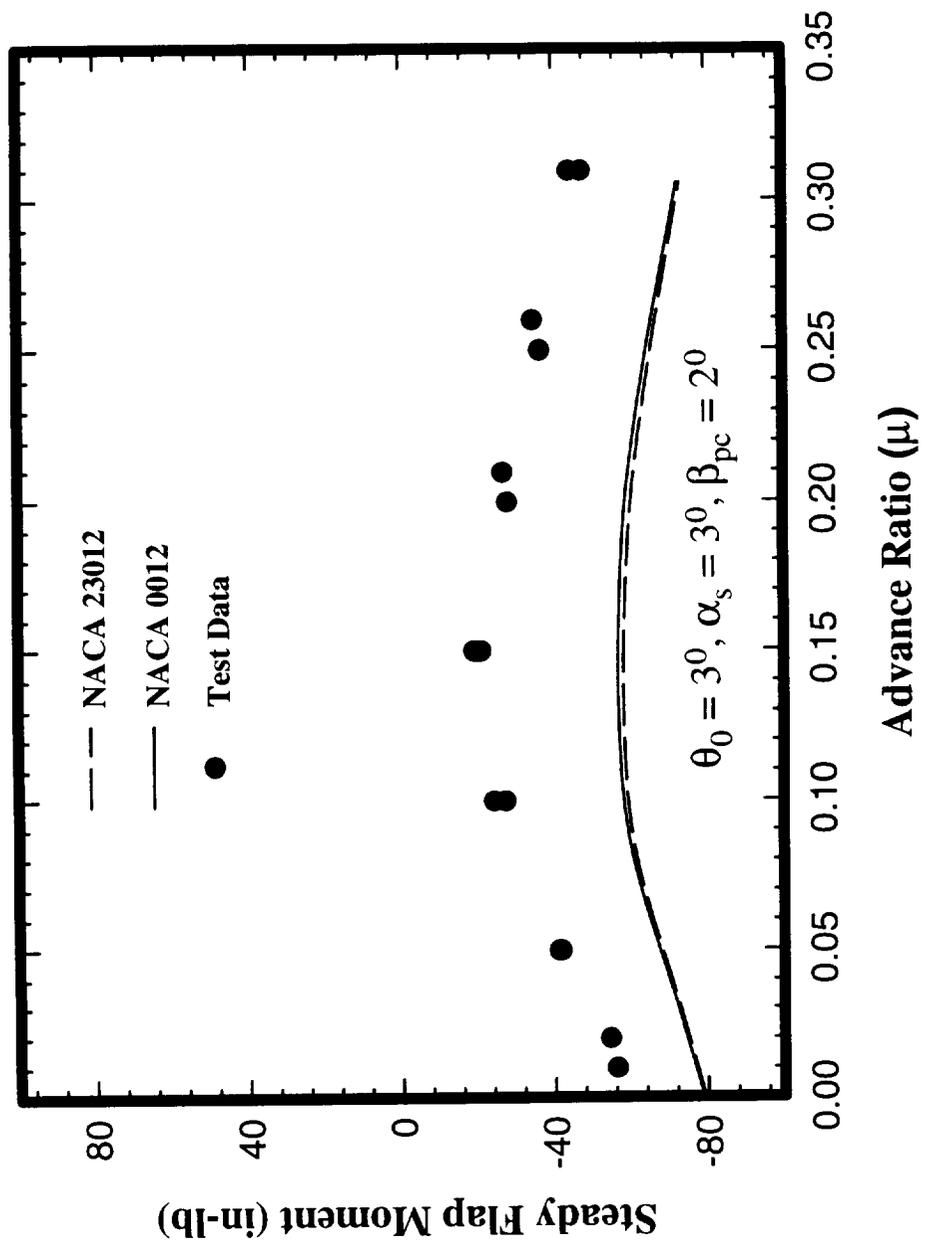
Figure 48: Effects of Dynamic Stall Parameters on Flapping Moment Based on the Force-Integration Method from the Dynamic Stall and Wake Theory for $\theta_0 = 3^0$ and $\alpha_s = 3^0$
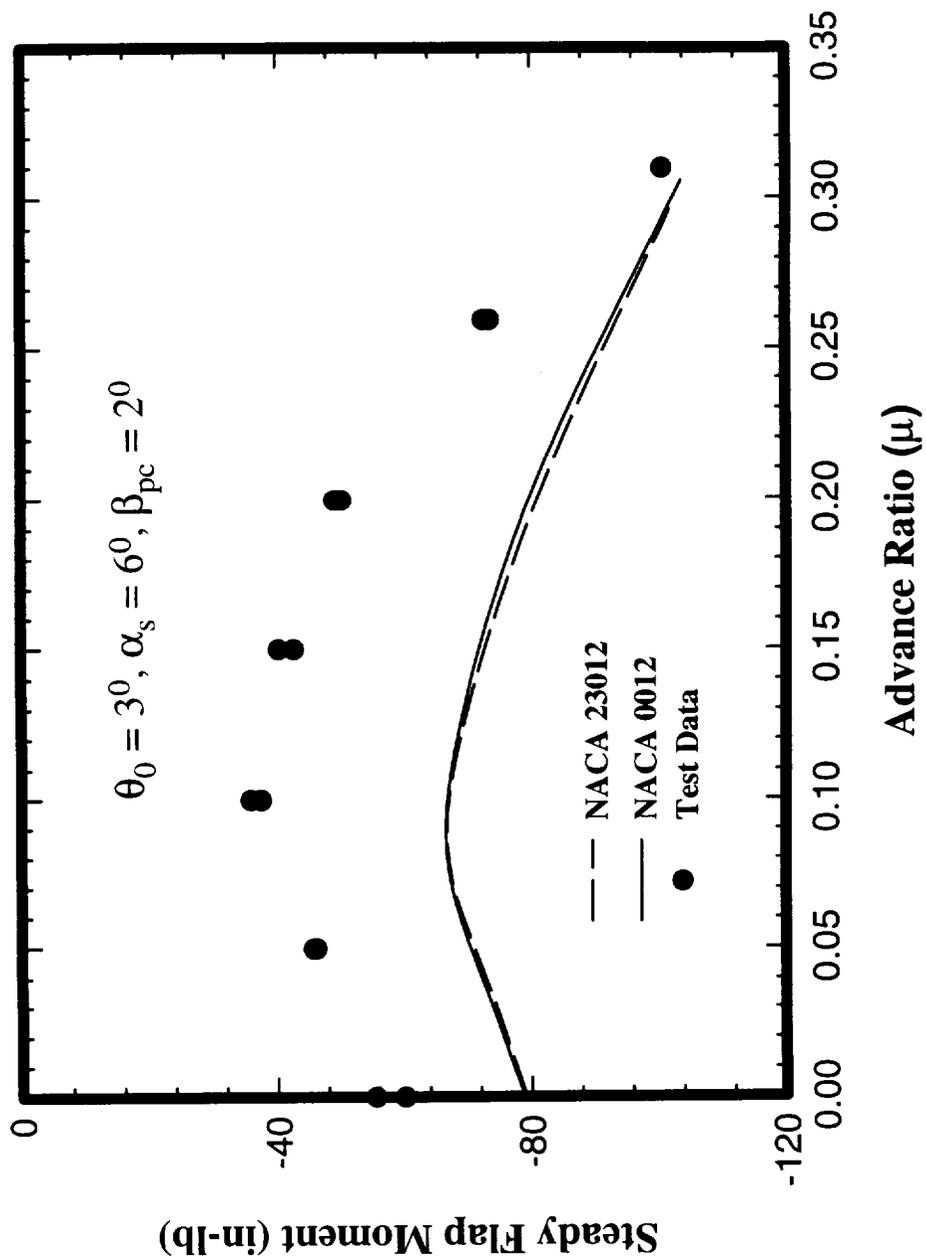
Figure 49: Effects of Dynamic Stall Parameters on Flapping Moment Based on the Force-Integration Method from the Dynamic Stall and Wake Theory for $\theta_0 = 3^0$ and $\alpha_s = 6^0$
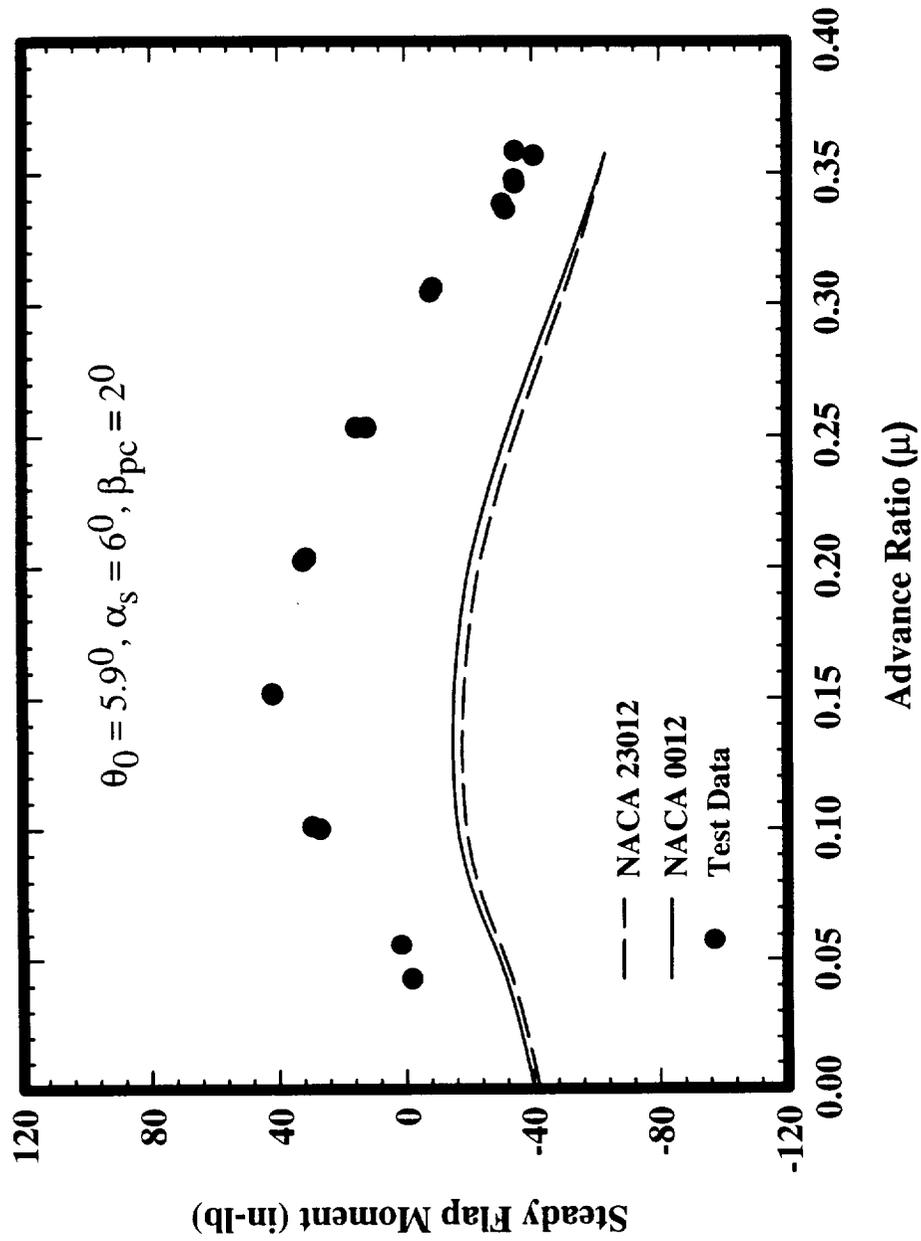
Figure 50: Effects of Dynamic Stall Parameters on Flapping Moment Based on the Force-Integration Method from the Dynamic Stall and Wake Theory for θ_0 5.9⁰ and $\alpha_s = 6^0$

References

[1] McNulty, M. J., "Flap-Lag Stability Data for a Small Scale Isolated Hingeless Rotor in Forward Flight," NASA TM 102189, Apr 1989.

[2] Gaonkar, G. H., McNulty, M. J. and Nagabhushanam, J., "An Experimental and Analytical Investigation of Isolated Rotor Flap-Lag Stability in Forward Flight," *Journal of the American Helicopter Society*, Vol. 35, (2), pp. 25-34, Jun 1990.

[3] Barwey, D., Gaonkar, G. H. and Ormiston, R. A., "Investigation of Dynamic Stall Effects on Isolated Rotor Flap-Lag Stability with Experimental Correlation," *Journal of the American Helicopter Society*, Vol. 36, (4), pp. 12-24, Oct 1991.

[4] Barwey, D. and Gaonkar, G. H., "Dynamic-Stall and Structural-Modeling Effects on Helicopter Blade Stability with Experimental Correlation," *AIAA Journal*, Vol. 32, (4), pp. 811-819, Apr 1994.

[5] Subramanian, S., Chunduru, S. and Gaonkar, G. H., "Effects of Dynamic Stall and Three-Dimensional Wake on Aeroelastic Stability of Isolated Hingeless Rotors with Experimental Correlation," Proceedings of the 50*th* Annual Forum of the American Helicopter Society, Washington, D.C., May 11−13, 1994 (also submitted to the *Journal of the American Helicopter Society*).

[6] Subramanian, S., *Dynamic Stall and Three-Dimensional Wake Effects on Trim and Stability of Isolated Rotors with Experimental Correlation and Parallel Fast-Floquet Analysis*, Ph.D. Thesis, College of Engineering, Florida Atlantic University, Boca Raton, FL, Aug 1996.

[7] Torok, M. S. and Chopra, I., "Hingeless Rotor Aeroelastic Stability Analysis With Refined Aerodynamic Modeling," *Journal of the American Helicopter Society*, Vol. 36, (4), pp. 48-56, Oct 1991.

[8] Tang, D, M. and Dowell, E. H., "Damping Prediction for a Stalled Rotor in Flap-Lag with Experimental Correlation," *Journal of the American Helicopter Society*, Vol. 40, (4), pp. 79-89, Oct 1995.

[9] Maier, T. H., Sharpe, D. L. and Lim, J., "Fundamental Investigation of Hingeless Rotor Aeroelastic Stability, Test Data and Correlation," Proceedings of the American Helicopter Society 51st Annual Forum, Forth Worth, TX, May 9-11, 1995.

[10] Maier, T. H., "Experimental Data for ADM Experimental Rotor," Private Communications, Jan 23, 1996 and June 24, 1996.

[11] Critzos, C. C., Heyson, H. H. and Boswinkle, Jr., R. W., "Aerodynamic Characteristics of NACA 0012 Airfoil Section at Angles of Attack From 0^0 to 180^0," NACA Tech Note 3361, Jan 1965.

[12] Nagabhushanam, J. and Gaonkar, G. H., "Automatic Identification of Modal Damping from Floquet Analysis," *Journal of the American Helicopter Society*, Vol. 40, (2), pp. 39-42, Apr 1995.

[13] Bielawa, R. L., "Blade Stress Calculation — Mode Deflection vs. Force Integration," *Journal of the American Helicopter Society*, Vol. 23, (2), pp. 10-16, Apr 1978.

[14] Ibrahim, S. R., "An Upper Hessenberg Sparse Matrix Algorithm for Modal Identification on Minicomputers," *Journal of Sound and Vibration*, Vol. 113, (1), pp. 47-57, Feb 1987.

Appendix

Dynamic Stall Parameters

NACA 23012 Airfoil Section(Ref. 6)

$$\lambda = 0.2 \tag{30a}$$

$$\delta = \frac{\partial C_{z_l}}{\partial \alpha} - \frac{a}{2} \tag{30b}$$

$$w = 0.10 + 0.023(|\alpha^0| - 13^0)u(|\alpha^0| - 13^0) \text{ if } |\alpha^0| \leq 21.7^0$$
$$= 0.3 \text{ if } |\alpha^0| > 21.7^0 \tag{30c}$$

$$d = \frac{0.105}{w} \tag{30d}$$

$$e = 2 - 5.1\tan^{-1}\left\{1.21(|\alpha^0| - 13^0)\right\} \times u(|\alpha^0| - 13^0)$$
$$\text{where } u \text{ is the unit step function} \tag{30e}$$

$$a_d = 0.32 \tag{31a}$$

$$r_d = 0.2 + 0.1\left(\Delta C_z\right)^2 \tag{31b}$$

$$E_d = -0.015\left(\Delta C_z\right)^2 \tag{31c}$$

$$a_m = 0.25 + 0.1\left(\Delta C_z\right)^2 \tag{32a}$$

$$r_m = 0.2 + 0.2\left(\Delta C_z\right)^2 \tag{32b}$$

$$E_m = 0.01\left(\Delta C_z\right)^2 \tag{32c}$$

NACA 0012 Airfoil Section (Ref. 8)

$$\lambda = 0.15 \tag{33a}$$

$$\delta = \frac{\partial C_{z_l}}{\partial \alpha} - \frac{a}{2} \tag{33b}$$

$$w^2(1 + d^2) = \left[0.2 + 0.1\left(\Delta C_z\right)^2\right]^2 \tag{33c}$$

$$2dw = 0.25 + 0.1\left(\Delta C_z\right)^2 \tag{33d}$$

$$e = -0.6\left(\Delta C_z\right)^2 \tag{33e}$$

$$a_d = 0.32 \tag{34a}$$

$$r_d = 0.2 + 0.1\left(\Delta C_z\right)^2 \tag{34b}$$

$$E_d = -0.015\left(\Delta C_z\right)^2 \tag{34c}$$

$$a_m = 0.25 + 0.1\left(\Delta C_z\right)^2 \tag{35a}$$

$$r_m = 0.2 + 0.1\left(\Delta C_z\right)^2 \tag{35b}$$

$$E_m = -0.6\left(\Delta C_z\right)^2 \tag{35c}$$